



UNIVERSITÀ
DEGLI STUDI
FIRENZE

DOTTORATO DI RICERCA

INTERNATIONAL DOCTORATE IN STRUCTURAL BIOLOGY

CICLO XXXI

COORDINATOR Prof. *Claudio Luchinat*

**Development and application of methods to investigate proteins
in mammalian cells by NMR**

Settore Scientifico Disciplinare CHIM/03

PhD student

Dott. *Panagis Polykretis*

Tutor

Prof. *Lucia Banci*

Coordinator

Prof. *Claudio Luchinat*

November 2015 – 2018

This thesis has been approved by the University of Florence,
the University of Frankfurt and the Utrecht University



TABLE OF CONTENTS

ABSTRACT

1. INTRODUCTION	1
1.1 Structural Biology	3
1.2 In-cell NMR	4
1.3 Aims of the research	6
2. RESEARCH PROJECTS	9
2.1. Development of inducible mammalian cell lines for in-cell NMR	11
2.1.1 Overview	11
2.1.2 Methodologies	12
2.1.3 Results & Discussion	14
2.1.4 Perspectives	16
2.2 Characterization of XIAP-BIR1 in mammalian cells by NMR	18
2.2.1 Overview	18
2.2.2 Attached article	21
2.3 Characterization of XIAP-BIR3 interaction with CCS and copper	41
2.1.1 Overview	41
2.1.2 Methodologies	42
2.1.3 Results & Discussion	43
2.1.4 Perspectives	45
2.4 Structural characterization of full length XIAP	46
2.2.1 Overview	46
2.2.2 Attached manuscript	48
2.5 Cadmium effects on Superoxide dismutase 1 in human cells	68
2.2.1 Overview	68
2.2.2 Attached manuscript	72
3. CONCLUSIONS	99
4. REFERENCES	103
5. ACKNOWLEDGEMENTS	113

ABSTRACT

In-cell NMR spectroscopy has proven to be an ideal technique for the characterization of the functional processes and maturation steps of biomolecules as it allows to study their structural and dynamic properties and networks of interactions directly in living cells, with atomic resolution. In fact, in-cell NMR allows to characterise a biomolecule within its physiological environment, where it is conditioned by different physicochemical parameters, such as pH, redox potential, viscosity, the presence of interaction partners and where it can undergo the eukaryotic post-translational modifications.

With the aim to extend the applicability of in-cell NMR, this thesis describes the development of a DNA vector, based on the piggyBac transposon system, that allows the stable integration and the expression of inducible genes of interest in the genome of mammalian cells.

Furthermore, in this thesis it is shown how the in-cell NMR methodology can be successfully applied in order to study the interaction between proteins and metal ions. In particular, the interaction of copper with the first domain of the X-chromosome linked inhibitor of apoptosis protein (XIAP) has been studied in living cells, as well as *in vitro*. In fact, this multidomain metalloprotein has been related to the regulation of the intracellular copper homeostasis, in addition to its very well-known role of inhibitor of apoptosis, which involves this protein in the onset of several diseases including cancer. Although XIAP has been intensively studied for more than twenty years, and the structures of all its single domains are known, there is no data on the conformation of the full-length protein, as it has never been purified in such form. In this thesis it is described a protocol for the expression and the purification of the full length XIAP, which allowed to characterize *in vitro* its quaternary structure and its overall conformation, by integrating different structural biology techniques, such as NMR, SAXS and EPR.

Finally, in-cell NMR spectroscopy has been applied to investigate the effect of cadmium treatment on the metal binding and redox state of the superoxide dismutase 1 (SOD1) in human cells. In this work we demonstrate that, unlike

what previously assumed, cadmium does not replace zinc bound to intracellular SOD1. Instead, it causes the premature oxidation of the cysteines involved in SOD1 intramolecular disulfide bond, compromising its correct maturation and explaining the reported decrease in superoxide dismutase activity in cadmium-exposed tissues. The mechanism proposed in this thesis establishes a novel link between cadmium toxicity, zinc homeostasis and reduced SOD1 activity, which does not involve direct cadmium binding to SOD1, and contributes to a better understanding of cadmium toxicology at the molecular level.

1. INTRODUCTION

1.1 Structural Biology

Structural biology is a scientific discipline which combines molecular biology, biochemical and biophysical techniques in order to study the structure and dynamics of macromolecules, such as proteins and nucleic acids and their interaction and complexes, trying to characterize their three-dimensional structure and its relation with their biological function. This is of fundamental importance for describing living matter at the atomic level and for understanding the functioning mechanism of cellular processes. In fact, the structure of a biomolecule is related to its functional features, and this concept is of fundamental importance in biology, pharmacology and medicine. The description of a biological macromolecule, as well as of its complexes, at atomic-level and the comprehension of the cellular processes in which it is involved are critical for the development of novel drugs and therapeutic treatments against human diseases. Macromolecules like proteins perform most of the cellular functions thanks to their specific conformation, generated by the spatial arrangement of the amino acid sequences that compose them, i.e. their tertiary and quaternary structure (apart from the intrinsically disordered proteins), which also defines their interactions with specific cellular partners. In this regard, structural biologists rely on various investigative techniques which allow them to perform structural characterizations of macromolecules, at atomic-level resolution. These techniques are: Nuclear Magnetic Resonance (NMR), X-ray crystallography and, recently, cryo-Electron Microscopy (cryo-EM). Additionally, low-resolution techniques that provide important complementary information for the structural characterization of macromolecules are: Electron Paramagnetic Resonance (EPR), Small Angle X-ray Scattering (SAXS), Fluorescence Resonance Energy Transfer (FRET) and others. Each of the aforementioned techniques have great potential, nevertheless they also have limitations, mainly linked to the intrinsic characteristics of the samples, such as the complexity and the size of the macromolecules, which do not allow to select a single technique of structural investigation as the “definitive approach”. Consequently, these methodologies

can currently be considered as complementary in providing information for the structural characterization of biological macromolecules with different characteristics and peculiarities. In fact, the winning strategy in structural biology has proven to be the integration these techniques, in order to take advantage of the potentialities of each one of them, in the effort to obtain the most complete and accurate result.

1.2 In-cell NMR

Among the techniques which represents one of the “analytical pillars” of structural biology, NMR spectroscopy allows to obtain atomic resolution information on the structure and dynamics of a molecule in solution. NMR spectroscopy is based on the absorption of radiofrequencies by nuclear spins when a molecule is placed in a magnetic field. The radiofrequencies induce nuclear spin transitions in NMR-active nuclei. In biomolecules ^1H , ^{15}N and ^{13}C nuclei are typically observed. Through NMR spectroscopy information on the molecular structure is obtained, as the nuclear spin resonating frequency and its relaxation properties are determined by the surrounding of the nucleus. With respect to the other main analytical techniques used in Structural Biology, i.e. X-ray crystallography and cryo-EM, NMR has the advantages to allow the non-destructive characterization of macromolecules in solution, at room temperature, and to observe time-dependent and dynamic processes, such as ligand binding and redox state variations. In fact, both X-ray crystallography and cryo-EM require static samples, in which the proteins are immobilized in crystals and/or frozen and thus, far away from their physiological environment.

The progress of the NMR technology in terms of higher resolution and sensitivity of the instruments, by means of higher magnetic fields and cryo-cooled probes, allowed us to perform multi-dimensional NMR experiments on complex systems such as living cells. As a result, a new frontier of NMR was born when an isotope-labelled protein was observed in living bacterial cells for the first time (Serber et al., 2001). Such pioneering approach was named in-cell

NMR, and in the following years has been further developed, by extending its applicability to eukaryotic cells (Selenko et al., 2006), and to human cells (Inomata et al., 2009). These achievements attracted the interest of the scientific community, as the ability to observe macromolecules directly in their physiological environment is of fundamental importance to study processes related to human diseases. Consequently, further methods have been developed for the delivery of exogenous proteins and DNA into human cells in order to perform in-cell NMR experiments, such as the permeabilization of the cellular membrane obtained by streptolysin O, or by electroporation (Ogino et al., 2009; Theillet et al., 2016; Dzatko et al., 2018). However, the methods based on the insertion of proteins previously purified from bacteria present some disadvantages concerning the internalization efficiency and the potential introduction of artefacts, due to the non-native proteosynthetic system. Consequently, some methods were developed in order to obtain the protein expression, at suitable levels for NMR experiments, directly in yeast (Bertrand et al., 2012), in insect cells (Hamatsu et al., 2013) and more importantly in human cells (Banci et al., 2013). In mammalian cells, this was achieved transfecting the cells with constitutively inducible expression vectors, containing the gene encoding the protein of interest (Fig. 1).

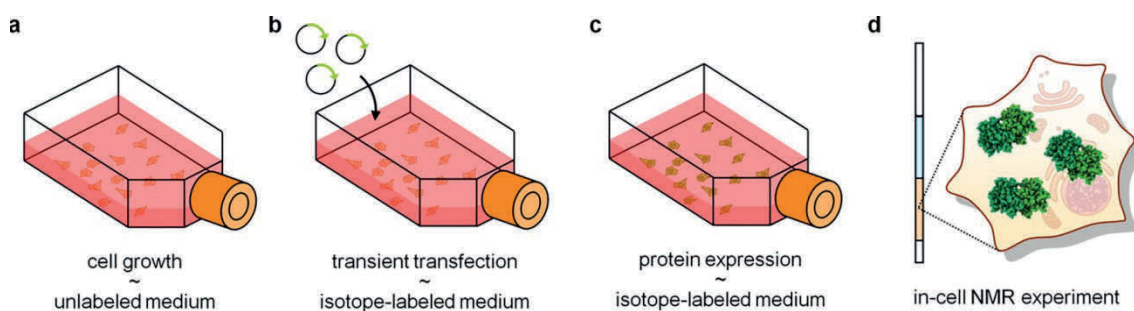


Fig. 1: Protein expression in mammalian cells for in-cell NMR experiments. (a) Mammalian cells are seeded in a culture flask and grown in unlabelled medium. (b) The plasmid containing a gene of interest (green arrow) is delivered by transient transfection in labelled medium. (c) Protein expression is carried out in labelled medium. (d) Cells expressing the protein of interest (green) are harvested and placed in a 3 mm Shigemi NMR tube for in-cell NMR analysis (image credit: Luchinat and Banci, 2018).

Thanks to this major improvement, in the following years, in-cell NMR proved to be an ideal technique for the characterization of functional processes and maturation steps of biomolecules with atomic resolution, thus allowing us to study their structural and dynamic properties and their networks of interactions directly in living human cells. In fact, in-cell NMR allows the characterization of a biomolecule within its physiological environment, where it is affected by different physicochemical parameters, such as pH, redox potential, viscosity, the presence of interaction partners and where it can undergo the typical eukaryotic post-translational modifications, which are fundamental for its function (Theillet et al., 2012; Barbieri et al., 2015; Smith et al., 2015; Mercatelli et al., 2016; Luchinat et al., 2017; Li et al., 2017; Capper et al., 2018; Barbieri et al., 2018; Luchinat and Banci, 2018).

1.3 Aims of the research

Considering the growing potential of in-cell NMR as a powerful Structural Biology analytical technique, the aim of my doctoral research was to further develop and apply in-cell NMR methods in order to investigate proteins in mammalian cells. In this regard, during my doctorate, I contributed to extend the applicability of in-cell NMR, developing a DNA vector that allows the stable integration and the expression of inducible genes, encoding specific proteins of interest, in mammalian cells. This method could be also extendable to other cell lines, such as embryonic stem cells, with the perspective to induce their differentiation towards specific cell types. A successful outcome of this method would add two important improvements to in-cell NMR, i.e. would make possible to induce the overexpression of a specific gene encoding a protein, without requiring the transfection with exogenous DNA, and would allow to perform structural investigations on proteins in their physiological tissues (e.g. neural cells, epithelial cells, etc.).

During my doctorate, I also applied the in-cell NMR methodology, combining it with *in vitro* measurements, to study the interaction between proteins and metal ions. In particular, I studied the interaction of copper with different domains of

the X-chromosome linked inhibitor of apoptosis protein (XIAP), a multifunction cytosolic metalloprotein that is involved in many important cellular processes, including copper homeostasis. Furthermore, I characterized *in vitro* the quaternary structure and the overall conformation of the full length XIAP, integrating different structural biology techniques. Finally, I studied the effects of cadmium on the maturation of the superoxide dismutase 1 (SOD1) in mammalian cells by NMR.

2. RESEARCH PROJECTS

2.1 Development of inducible mammalian cell lines for in-cell NMR

2.1.1 Overview

In-cell NMR spectroscopy has proven to be an ideal technique for the characterization of the functional processes and maturation steps of biomolecules, as it enables the study of their structural and dynamic properties and networks of interactions directly in living cells, with atomic resolution. The method currently employed relies on the protein over-expression in human embryonic kidney (HEK293T) cells by transient transfection with exogenous DNA mediated by polyethylenimine (PEI) (Aricescu et al., 2006). The genes encoding the proteins of interest are cloned in the pHLsec plasmid (modified from Aricescu et al., 2006) and their expression is controlled by the strong constitutive cytomegalovirus early enhancer/chicken β actin (CAG) promoter (Niwa et al., 1991; Fukuchi et al., 1994). In this way, the expression of such genes starts when the internalization of the DNA vector is completed. This method has proven to be very efficient to obtain the intracellular protein levels required to perform in-cell NMR, but does not allow to control or modulate the gene expression by an external triggering signal and it requires a new transfection for each sample. Therefore, the opportunity to perform experiments on cell lines stably transfected with inducible genes encoding the protein of interest would constitute a significant further improvement for the technique. This study aims to create mammalian cells lines stably transfected with inducible genes of interest, in order to obtain the overexpression of specific proteins at suitable levels for in-cell NMR experiments. The genes that have been chosen for this purpose are those encoding the copper transport protein human ATX homolog 1 (HAH1), superoxide dismutase 1 (SOD1) and the copper chaperone for superoxide dismutase (CCS). In order to maximize the gene expression and consequently the intracellular protein levels, an efficient method for the integration of multiple copies of each gene in the genome of the host cells was required. Indeed, spontaneous integration of exogenous DNA in the host genome of mammalian cells is an inefficient process that leads to very low number of integrated copies of the genes of interest, resulting in low

protein levels, therefore classical protocols are not suitable for in-cell NMR. On the basis of this consideration, we decided to use a different approach which could allow the integration of a larger number of copies of our target genes into the host genome. To this purpose, one of the most promising approaches to date relies on the piggyBac (PB) transposon (Wu et al., 2006). Transposons or “jumping genes” are mobile genetic elements that can change their position within a genome, often resulting in the duplication of the genetic sequence. The PB transposon relies on the action of the homonymous transposase, which is responsible for the excision and insertion of such mobile genetic material via a “cut and paste” mechanism. More precisely, during transposition, the PB transposase identifies specific sequences termed inverted terminal repeats (ITRs) located at the edges of the transposon, excises their content and efficiently inserts it into TTAA chromosomal sites, showing a “palindromic” preference for regions where T and A repetitive sequences are respectively located upstream and downstream from the central TTAA site (Wilson et al., 2007). Previous estimation of the number of insertions, performed through integration analysis, reported 575 potential PB integration sites within the genome of HEK293 and HeLa cells (Wilson et al., 2007), and 228 in the genome of human T cells (Galvan et al., 2009). The high transposition efficiency and the ability to transpose DNA fragments up to 14 kb, makes PB transposon suitable for a variety of gene therapy studies (Wilson et al., 2007). Therefore, considering the potentials of the PB transposon, we chose to use this technique in order to achieve the integration of multiple gene copies, controlled by an inducible promoter, within the genome of mammalian cells. This method could allow to extend the applicability of the inducible systems for in-cell NMR to other cell lines, such as murine Embryonic Stem Cells (mESCs).

2.1.2 Methodologies

The host vector pCyL-50:PB containing the ITRs (Wang et al., 2008) and the vector encoding the PB transposase pCMV-HyPBase (Yusa et al., 2011) were kindly provided by the Wellcome Trust Sanger Institute. The pCyL-50:PB host

vector was modified to allow cloning of the mammalian expression cassette, through the MXS-chaining protocol (Sladitschek and Neveu, 2015). The mammalian expression cassette used in this study contains a bidirectional Tet-On promoter, inducible by doxycycline, which controls the expression of the genes encoding HAH1, SOD1, or CCS (Fig. 2).



Fig. 2: Schematic representation of the mammalian expression cassette containing a bidirectional Tet-On promoter, controlling the expression of the genes encoding HAH1, SOD1 or CCS (TRE: Tetracycline responsive element; CMV: Cytomegalovirus minimal promoter; H2B: Histone H2B; bGHpA: Bovine growth hormone polyadenylation signal; PGK: Mouse phosphoglycerate kinase 1 promoter; NeoR: Neomycin resistance; rtTA: Reverse tetracycline-controlled transcriptional activator).

Such bidirectional Tet-On promoter contains a tetracycline responsive element (TRE), composed by seven copies of the tetracycline operator *tetO*, between two minimal cytomegalovirus (CMV) promoters with opposite orientation. The aforementioned mammalian expression cassettes were then cloned in the modified PB host vector, obtaining three distinct new vectors encoding HAH1 (pCyL-9071neo, 9304 bp), SOD1 (pCyL-9073neo, 9562 bp) and for CCS (pCyL-9075neo, 9922 bp). The correct ligation of the genes of interest was screened by analysing the restriction profiles of each plasmid (using EcoRI and KpnI). HEK293 cells were chosen first as, unlike HEK293T, they are sensitive to neomycin analogues (such as G418). HEK293 cells were co-transfected with the pCyL-9073neo host vector, along with the pCMV-HyPBase plasmid (at the ratio of 2:1). During co-transfection (lasted 48 hours), HEK293 cells were maintained in Dulbecco's modified Eagle's medium (DMEM; high glucose, D6546, Sigma) supplemented with L-glutamine, antibiotics (penicillin and streptomycin) and 2% FBS (Gibco) in uncoated 75 cm² plastic flasks and incubated at 310 K and 5% CO₂. The stable integration of the gene was then evaluated by maintaining the cells for three weeks under antibiotic selective pressure with G418 (0.75

mg/mL), without adding penicillin and streptomycin in the media, as they negatively compete with G418. Finally, colonies of monoclonal cell lines encoding SOD1 derived from single cells were obtained, which were manually selected under an inverted phase contrast optical microscope (OPTIKA XDS-2) and seeded separately. The expression test was performed by Western Blot, comparing the protein amounts (normalized on the total protein concentration of the cell lysates) obtained in stably transfected monoclonal HEK293 cells induced with 1 μ g/mL of doxycycline, with those obtained transiently transfecting HEK293T cells with 25 μ g of PB host vector encoding SOD1 and inducing the expression with 1 μ g/mL doxycycline under the same experimental conditions.

The PB host vectors were further modified by replacing the gene conferring geneticin resistance with that for puromycin resistance, to allow selection of stable HEK293T cells. The newly obtained vectors, conferring the puromycin resistance, i.e. pCyL-9071puro (9155 bp), pCyL-9073puro (9413 bp), pCyL-9075puro (9773 bp), were screened again by analysing their restriction profiles (using HindIII, Sall and XbaI) and were used to stably transfect HEK293T cells following the same procedure described above. The four polyclonal HEK293T cell lines stably transfected with the inducible genes encoding HAH1, SOD1, CCS and poly-A (negative control), were maintained under antibiotic selective pressure for two weeks with puromycin (2 μ g/mL).

2.1.3 Results & Discussion

We first tested the efficiency of the PB transposon on a cell line optimised for protein expression, such as HEK293. Thus, we cloned the mammalian expression cassette (Fig. 2) in the pCyL-50:PB vector, obtaining three different PB host plasmids carrying the inducible genes encoding HAH1, SOD1 and CCS (Fig. 3). Consequently, the pCyL-9073neo host vector has been used to transfect HEK293 cells, obtaining stably transfected cells with the inducible gene encoding SOD1. However, the expression test indicated that the protein levels were still not sufficient for in-cell NMR experiments and were notably lower in

comparison with the expression levels obtained in HEK293T cells transiently transfected with the same plasmid (Fig. 4).

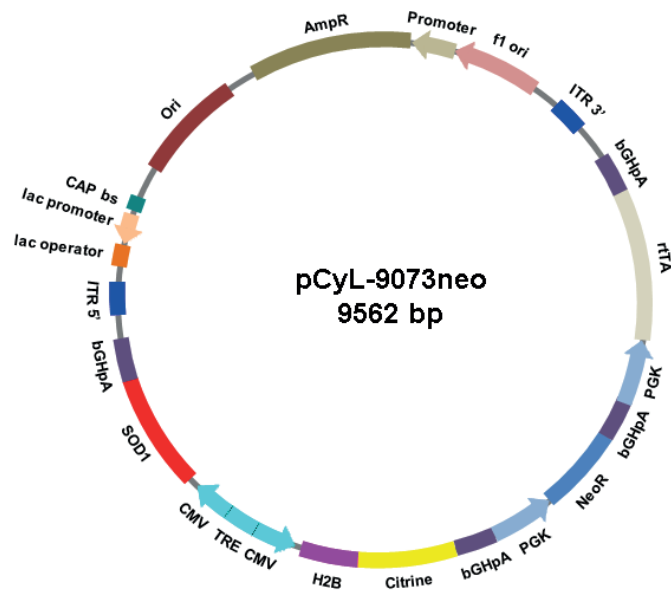


Fig. 3: Schematic representation of the pCyL-9073neo plasmid containing the mammalian expression cassette with the gene encoding SOD1 and the ITRs recognised by the PB trasposase. The pCyL-9071neo (9304 bp) and the pCyL-9075neo (9922 bp) plasmids, contain respectively the genes *HAH1* and *CCS* instead of *SOD1*. (F1 ori: Bacteriophage 1 origin of replication; AmpR: Ampicillin resistance; Ori: Origin of replication; CAP bs: Catabolite activator protein binding site; lac promoter: Lactose promoter; lac operator: Lactose operator).

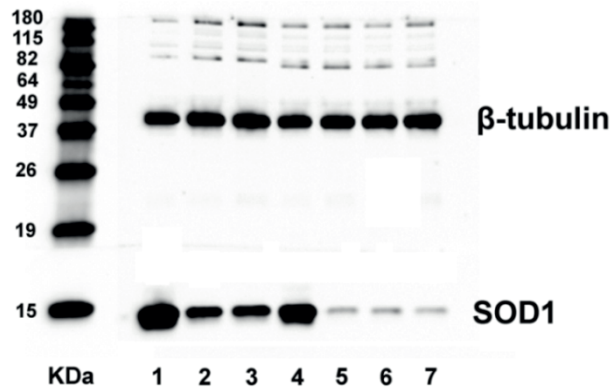


Fig. 4: Western Blot performed in order to compare the efficiency (in terms of amount of SOD1 normalized on the total protein concentration of the cell lysates) of the PB integration methodology, with that currently employed in our laboratory for in-cell NMR experiments. **Lane 1:** HEK293T transiently transfected with pHLsec-SOD1; **lane 2:** HEK293T transiently transfected with the plasmid containing the mammalian expression cassette shown in Fig. 2, induced with 1 $\mu\text{g}/\text{mL}$ of doxycycline; **lane 3:** HEK293T transiently transfected with pCyL-9073neo, induced with 1 $\mu\text{g}/\text{mL}$ of doxycycline; **lane 4:** HEK293 transiently transfected with pHLsec-SOD1; **lane 5:** HEK293 transiently transfected with the plasmid containing the mammalian expression cassette shown in Fig. 2, induced with 1 $\mu\text{g}/\text{mL}$ of doxycycline; **lane 6:** HEK293 transiently transfected with pCyL-9073neo, induced with 1 $\mu\text{g}/\text{mL}$ of doxycycline; **lane 7:** monoclonal HEK293 stably transfected with the inducible gene encoding SOD1, induced with 1 $\mu\text{g}/\text{mL}$ of doxycycline.

Overall, in the aforementioned expression test, HEK293T cells showed better results, in terms of protein levels, in all the analysed cases. This fact prompted us to modify again the PB host vectors shown in Fig. 3, replacing the gene conferring geneticin resistance with that for puromycin resistance, in order to adapt it for the neomycin-resistant HEK293T cells. The newly obtained PB host plasmids have been screened again, through restriction enzyme analysis of ligation (Fig. 5), and finally, were used to stably transfect HEK293T cells.

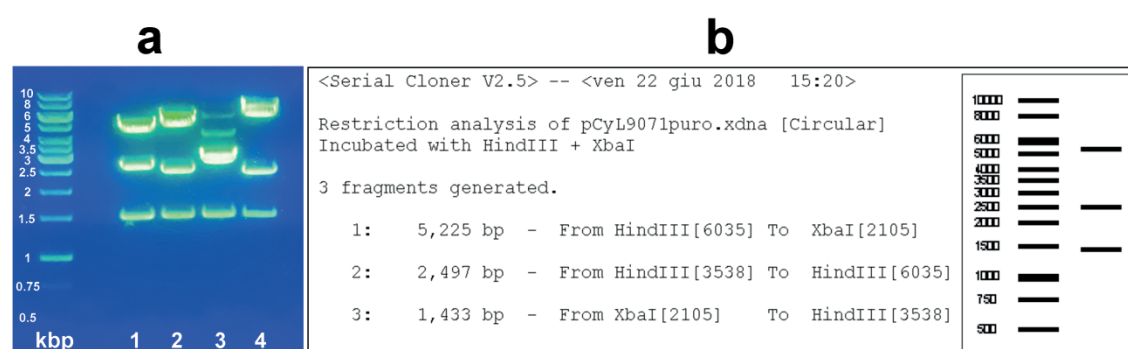


Fig. 5: Restriction analysis of the puromycin resistant PB host vectors. **a)** Agarose gel electrophoresis: **lane 1:** pCyl-9029puro incubated with HimdIII+Sall+XbaI; **lane 2:** pCyl-9071puro incubated with HimdIII+XbaI; **lane 3:** pCyl-9073puro incubated with HimdIII+Sall+XbaI; **lane 4:** pCyl-9075puro incubated with HimdIII+Sall+XbaI. **b)** Example of the restriction profile of the pCyl-9071puro vector obtained by the Serial Cloner 2.6 software.

At the moment, four polyclonal cell lines stably transfected with the inducible genes encoding HAH1, SOD1, CCS and poly-A (control) have been selected. As next step, from the aforesaid polyclonal cell lines, some monoclonal lines will be selected and their efficiency in terms of protein expression will be tested by Western Blot and by in-cell NMR.

2.1.4 Perspectives

Once the efficiency of this method will be optimised on HEK293T cells, obtaining samples suitable for in-cell NMR experiments, the PB vector will be used to stably transfect mESCs at multiple chromosomal sites. As further step, considering the characteristic of pluripotency of the mESCs, we are planning to develop a set of protocols for the selective and controlled differentiation of the stem cells towards specific cell lines. Such challenging project, would allow to

perform in-cell NMR experiments on cells adopting cellular phenotypes of specific tissues, depending on the physiological environment where the protein target of study exerts its function.

2.2 Characterization of XIAP-BIR1 in mammalian cells by NMR

2.2.1 Overview

The X-chromosome linked inhibitor of apoptosis protein (XIAP) is a 497-residue cytoplasmic zinc binding protein, ubiquitously expressed in all human cells except peripheral blood leukocytes (Liston et al., 1996). XIAP contains three zinc-binding baculovirus IAP repeat (BIR) domains at the N-terminal region, an ubiquitin associated (UBA) domain and a C-terminal, zinc-binding really interesting new gene (RING) domain (Fig. 6).



Fig. 6: Schematic representation of XIAP protein.

XIAP is a member of the IAP family, and was first recognised as a potent inhibitor of apoptosis, impeding directly the proteolytic activity of caspases (Deveraux et al., 1997). More precisely, through its BIR2 domain and a portion of the linker between BIR1 and BIR2, XIAP binds and inhibits the effector caspases 3 and 7 (Sun et al., 1999; Riedl et al., 2001; Chai et al., 2001), and through its BIR3 domain inhibits the initiating caspase 9 (Srinivasula et al., 2001). XIAP is frequently overexpressed in tumours, in which it potentiates cell survival and resistance to chemotherapeutics, and thus it has become an important target for the development of cancer treatments aimed to antagonize the interaction of XIAP with caspases (Schimmer et al., 2006; Nakagawa et al., 2006; Mizutani et al., 2007; Lopes et al., 2007; Mannhold et al., 2010; Fulda and Vucic, 2012; Baggio et al., 2018). Furthermore, its BIR1 domain, after dimerization, interacts with TAK binding protein 1 (TAB1), which in turn recruits transforming growth factor β activated kinase 1 (TAK1), with consequent activation of NF- κ B and cell survival pathways (Fig. 7) (Lu et al., 2007). Consequently, the impairment of the BIR1-TAB1 assembly would have a

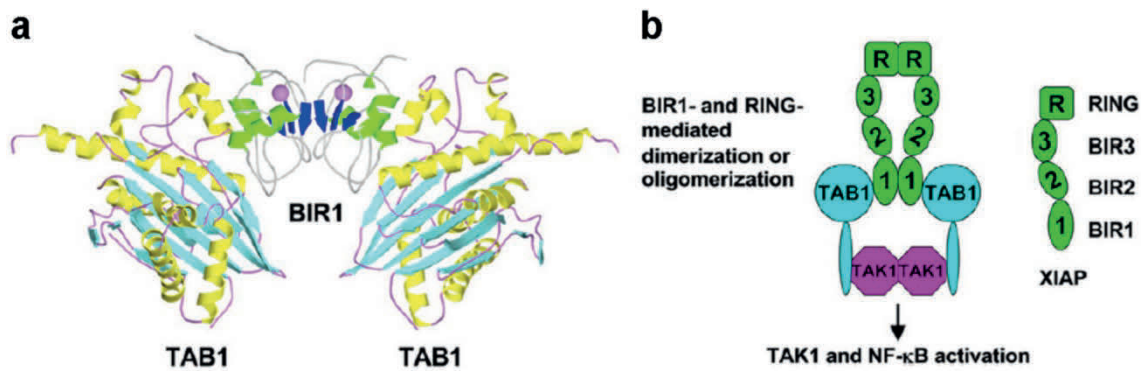


Fig. 7: Dimeric BIR1/TAB1 complex. TAB1 is shown with helices in yellow, β strands in cyan, and loops in pink, respectively. BIR1 is shown with helices in green, β strands in blue, and loops in gray. **b)** Schematic model for XIAP-mediated TAK1 and NF- κ B activation (image credit: taken and modified from Lu et al., 2007). In this model the UBA domain is missing.

synergistic action to the pro-apoptotic anticancer drugs. Moreover, XIAP has been reported to be involved the homeostasis of copper, and direct copper binding has been reported at multiple sites within the BIR domains (Burstein et al., 2004; Mufti et al., 2006, 2007; Galbán and Duckett, 2010; Liang et al., 2014). However, such interaction has not yet been characterized in cell. While the crystallographic structure of BIR1 is known (Lu et al., 2007), its structural properties in solution have not been characterized, including the function of the first 19 N-terminal residues of the domain, which were not resolved in the crystallographic structure. Consequently, in this study we sought to characterize through high-resolution NMR spectroscopy the BIR1 domain of XIAP *in vitro* and in the cytoplasm of *E. coli*, *X. laevis* oocytes and human cells, in order to provide a deeper description of the behaviour of this domain in its physiological environment. Furthermore, we evaluated the effects of copper addition in the oxidized and reduced states on BIR1. Our results, in accordance with the crystallographic structure, demonstrate that BIR1 forms a homodimer in solution, and that such dimerization can be impaired by two mutations (D71N and R72E) at the interface of the dimer, obtaining well-folded monomers. In-cell NMR experiments indicate that intracellular BIR1 interacts with intracellular partners or other cellular components, which decrease its tumbling rate causing the broadening of most signals beyond detection, while the N-terminal residues, which are absent in the crystal structure, are

unstructured and thus free to rotate. Concerning the interaction with copper, we showed that Cu(II) does not substitute the zinc ion in the zinc-finger motif, unlike what previously reported (Liang et al., 2014); that Cu(I) and (II) do not bind specifically to BIR1, both *in vitro* and in-cell, but rather Cu(II) serves as oxidant of cysteine 12 in causing the formation of a disulfide bond, most likely with glutathione or with the cysteine 12 of the other subunit of the homodimer.

SCIENTIFIC REPORTS

OPEN Solution structure and interaction with copper *in vitro* and in living cells of the first BIR domain of XIAP

Received: 6 April 2017

Accepted: 16 November 2017

Published online: 30 November 2017

Meng-Meng Hou¹, Panagis Polykretis², Enrico Luchinat^{2,3}, Xiao Wang¹, Shen-Na Chen¹, Hui-Hui Zuo¹, Yin Yang¹, Jia-Liang Chen¹, Yansheng Ye⁴, Conggang Li⁴, Lucia Banci^{2,5} & Xun-Cheng Su¹

The X-chromosome linked inhibitor of apoptosis (XIAP) is a multidomain metalloprotein involved in caspase inhibition and in copper homeostasis. It contains three zinc-binding baculoviral IAP repeats (BIR) domains, which are responsible for caspase interaction. Recently, it has been suggested that the BIR domains can bind copper, however high resolution data on such interaction is missing. Here we characterize by NMR the structural properties of BIR1 in solution, and the effects of its interaction with copper both *in vitro* and in physiological environments. BIR1 is dimeric in solution, consistent with the X-ray structure. Cysteine 12, located in the unfolded N-terminal region, has a remarkably low redox potential, and is prone to oxidation even in reducing physiological environments. Interaction of BIR1 with copper(II) results in the oxidation of cysteine 12, with the formation of either an intermolecular disulfide bond between two BIR1 molecules or a mixed disulfide bond with glutathione, whereas the zinc binding site is not affected by the interaction.

The X-chromosome linked inhibitor of apoptosis (XIAP) is a direct inhibitor of caspases and has been regarded as a potential target for therapy of cancer^{1,2}. XIAP is a 497-residue cytoplasmic zinc-binding protein containing three baculoviral IAP repeats (BIR) domains at the N-terminal region, followed by an ubiquitin-associated domain (UBA) and a Really Interesting New Gene (RING) domain at the C-terminus. Each BIR domain contains a CCHC zinc binding motif, while the RING domain contains a CCCHCCCC motif that binds two zinc ions. XIAP was first recognized as an inhibitor of apoptosis due to its specific interactions with caspases 3 and 7, mediated by BIR2 domain, and caspase 9, mediated by BIR3³⁻⁶. BIR1 was found to be involved in the interaction with TAB1 in the NF- κ B pathway⁷. Recently, additional roles of XIAP in receptor signaling, cell division, ubiquitin ligation and copper homeostasis have been reported⁸.

In human cells, the concentration of copper is tightly controlled by copper chaperones and imbalances of copper concentration results in diseases like Menkes or Wilson's disease⁹. Recent studies have shown that XIAP is involved in cellular copper homeostasis and the direct interaction of XIAP with copper ions was reported¹⁰⁻¹². It was also suggested that XIAP binds copper via the coordination of cysteines and it undergoes conformation changes upon copper binding¹¹, resulting in decreased stability of XIAP. A later study showed that several cysteine residues in the BIR2 and BIR3 domains can coordinate copper(I), both at the zinc binding site and at additional surface sites¹². Compared with BIR2 and BIR3, BIR1 was less studied, even though it has been reported by X-ray crystallography that BIR1 forms dimeric complex either in its free state or complexed with TAB1⁷. BIR1 forms a stable homodimer in the crystal structure, in which the BIR1 monomers are held together by electrostatic and hydrophobic interactions. However, the structural characterization of BIR1 in solution has not been reported and

¹State Key Laboratory and Research Institute of Elemento-organic Chemistry, College of Chemistry, Collaborative Innovation Center of Chemical Science and Engineering (Tianjin), Nankai University, Tianjin, 300071, China.

²Magnetic Resonance Center – CERM, University of Florence, 50019, Sesto Fiorentino, Florence, Italy. ³Department of Biomedical, Clinical and Experimental Sciences, University of Florence, 50134, Florence, Italy. ⁴Key Laboratory of Magnetic Resonance in Biological Systems, State Key Laboratory of Magnetic Resonance and Atomic and Molecular Physics, National Center for Magnetic Resonance in Wuhan, Wuhan Institute of Physics and Mathematics, Chinese Academy of Sciences, Wuhan, 430071, China. ⁵Department of Chemistry, University of Florence, 50019, Sesto Fiorentino, Florence, Italy. Meng-Meng Hou, Panagis Polykretis, Enrico Luchinat, Xiao Wang, Shen-Na Chen and Hui-Hui Zuo contributed equally to this work. Correspondence and requests for materials should be addressed to L.B. (email: banci@cerm.unifi.it) or X.-C.S. (email: xunchengsu@nankai.edu.cn)

the function of the N-terminal residues (1–19), which were not observed in the crystal structure, has not been elucidated.

In the present study, the structural properties of BIR1 were characterized using high-resolution NMR spectroscopy *in vitro* and in different physiological environments, namely in the cytoplasm of *E. coli*, *X. laevis* oocytes and cultured human cells. The effect of copper addition in both oxidation and reduced states on BIR1 was then characterized. Wild-type BIR1 exists as a stable homodimer in solution, in line with the existing X-ray data. The dimerization can be impaired by two point mutations at the dimer interface, D71N/R72E, resulting in a well-folded monomeric protein. In-cell NMR experiments show that BIR1 interacts with cellular constituents in the cytoplasm of different cells, causing the loss of NMR signals from the well-structured residues. The N-terminal residues 1–19, which are absent in the crystal structure, are unstructured. No interaction between BIR1 and copper(I) was observed both *in vitro* and in-cell. Remarkably cysteine 12, which resides in a well-conserved TCVP motif in the unstructured N-terminal tail among XIAP homologues, presents a very low redox potential (~–300 mV), and is found to react with copper(II) leading to the formation of either a disulfide-linked protein dimer or an adduct with glutathione *in vitro* and in-cell lysate.

Results and Discussion

Structural and dynamical characterization in solution of WT BIR1 and its D71N/R72E mutant.

The apo form of BIR1 (i.e. BIR1 lacking the zinc ion) is unfolded in solution as determined by ¹⁵N-HSQC spectra since all the cross-peaks show narrow dispersions and sharp linewidths, and hence in the present study all the protein samples were prepared by denature-refolding process in the presence of zinc ion (see experimental section). Wild-type BIR1 (WT BIR1) shows well dispersed resonances in the ¹⁵N-HSQC spectra, which are characteristic of a well-folded protein but characterized by quite large linewidths (Fig. 1A). ¹⁵N heteronuclear relaxation rates R_1 and R_2 of backbone amide nitrogen indicated different behaviors for various stretches of the protein, with the N- and C-termini characterized by high R_1 and low R_2 , indicative of fast motions on the ns-ps time scale and the central part with the opposite pattern (Figure S1). Overall, the linewidths of most cross-peaks are larger than those expected from a monomeric polypeptide chain, suggesting that the protein exists as an oligomer or experiences conformation exchange in solution. The averaged R_2/R_1 ratios in the well-structured segments indicated a rotational correlation time (τ_c) of 17.5 ns, consistent with a dimeric protein of 23 kDa. The large R_2 values hampered the spectral assignment procedure based on standard triple resonance experiments. Therefore, we sought to design a mutant that would be monomeric in solution, in order to facilitate the NMR assignment. We then transferred the assignment of the mutant to the ¹⁵N-HSQC spectra of WT BIR1.

In the crystal structures of homodimeric BIR1¹³, D71 and R72 of one subunit form salt bridges with R82 and D77, respectively, of the other subunit. Additional hydrogen bonds are also present between T60-K85 and D71-K85. As the salt bridges involving D71 and R72 likely play an essential role in stabilizing the dimeric complex, the double-point mutant D71N/R72E was investigated. Compared to WT BIR1, D71N/R72E BIR1 gave rise to significantly narrower NMR signals (Fig. 1B), which permitted the assignment of most backbone resonances with the triple resonance NMR spectra HNCA, CBCA(CO)NH and NOESY-¹⁵N-HSQC. The cross-peaks in ¹⁵N-HSQC spectrum corresponding to residues of T2, F3, E20, F23, V24 and G56 were not assigned due to line broadening effects (Fig. 1). The ¹⁵N heteronuclear relaxation values R_1 and R_2 of backbone amide nitrogens have a similar pattern to those of WT BIR1 over the various sequence segments. The R_2/R_1 ratio gives a τ_c of 7.3 ns, consistent with the monomeric state.

NOESY-¹⁵N-HSQC spectra recorded for WT BIR1 and D71N/R72E indicated that both two protein constructs share similar secondary structural elements to the dimeric structure as determined by X-ray crystallography.¹³ The backbone assignment of D71N/R72E BIR1 was therefore transferred to WT BIR1 and cross-checked with 3D HNCA, CBCA(CO)NH and ¹⁵N-NOESY-HSQC spectra of WT BIR1. Residues E22, E25, A69, E72, Y75, G76, D77, K85, V86, F92, I93 and N94 could not be identified in the ¹⁵N-HSQC spectrum of WT BIR1, most likely due to line broadening effects.

Chemical shift differences between the two forms were observed, as expected, for the residues vicinal to the homo-dimeric interface (Fig. 2A). Most unassigned residues in WT BIR1 are located at the dimer interface (Fig. 2B), suggesting that the dimeric BIR1 complex in solution experiences conformational exchange that broadens a number of residues in the ¹⁵N-HSQC spectra. The N-terminal residues 1–19, which are not observed in the X-ray structure^{7,13}, generally produce narrower cross-peaks in the ¹⁵N-HSQC spectrum. Interestingly, the N-terminal residue T11 and C-terminal residues F96 and Y97 also show significant chemical shift difference between the dimeric and monomeric forms, suggesting that a dynamic contact between these residues may occur in the dimeric form in solution. The secondary structure prediction based on the backbone chemical shifts, obtained using TALOS+¹⁴, suggested that the stretches containing residues 3–16 and 97–105 are unstructured.

With the assignment of backbone resonances of the D71N/R72E mutant, we performed structural calculations using CS-Rosetta protocol¹⁵. The unstructured segments at the flexible N- and C-termini containing residues 1–22 and 97–105 were excluded from the calculations. The backbone chemical shifts of C^α, C^β, CO, HN and N were used in the CS-Rosetta calculations, and nicely converged structures for monomeric D71N/R72E mutant were determined (Fig. 3). The structures produced are well defined, with a mean pair-wise backbone RMSD among the 10 lowest-energy structures of 1.46 ± 0.71 Å. The lowest-energy structure has a 1.3 Å backbone root mean square deviation (RMSD) to the crystal structure of the BIR1 (PDB code: 2QRA)¹³. Consistent with the dimeric X-ray structure of WT BIR1¹³, the regularly structured elements produced well conserved short and long-range NOEs between HN-HN and HN-HA, indicative of α-helix and β-strands, in the NOESY-¹⁵N-HSQC spectrum recorded for D71N/R72E mutant, indicating the highly reliable CS-Rosetta structure.

BIR1 is prone to oxidation in solution. Both WT BIR1 and the D71N/R72E mutant are prone to oxidation in solution as determined by NMR, mass spectrometry and gel filtration. When BIR1 is purified in absence

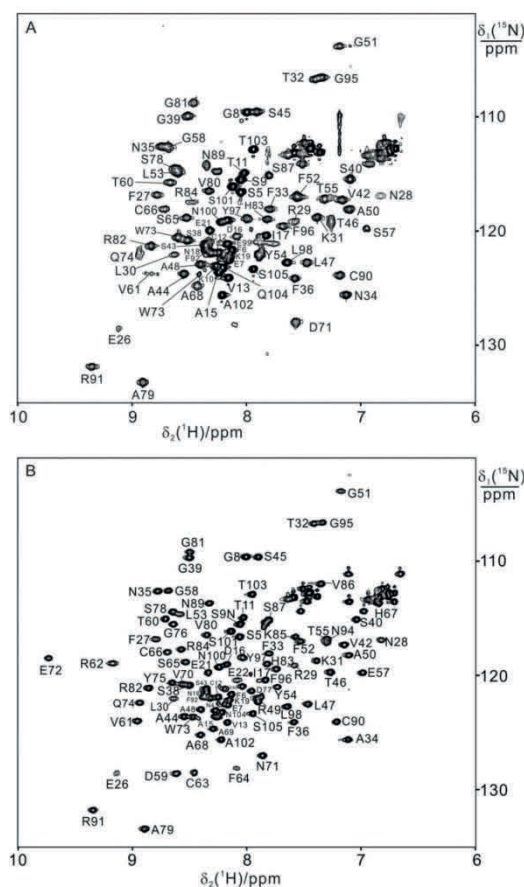


Figure 1. ^{15}N -HSQC spectra of BIR1 in solution. The NMR spectra were recorded for 0.3 mM WT BIR1 (1–105 aa) (A) and 0.3 mM D71N/R72E mutant of BIR1 (B) in 20 mM Bis-Tris buffer at pH 6.5 and 298 K with a proton frequency of 600 MHz. The cross-peaks with assignment were labeled.

of reducing agents, two species are observed in the ^{15}N -HSQC spectra, where both WT and D71N/R72E BIR1 displayed additional cross-peaks. These additional cross-peaks disappeared upon addition of 2 equivalents of DTT, suggesting that oxidation of C12, the only solvent-exposed free cysteine in BIR1, may have occurred. The oxidized protein could be obtained by dialyzing the reduced protein sample in 20 mM Tris at pH 9 at 4°C overnight. Comparison of the ^{15}N -HSQC spectra reveals that the residues close to C11, including V13, experienced significant chemical shift changes upon oxidation (Figure S2). The oxidized species of D71N/R72E BIR1 was also characterized by MALDI-TOF mass spectrometry. Two main species were observed, corresponding to monomeric and dimeric D71N/R72E BIR1 (Figure S3). The latter species is absent in the sample treated with DTT. As the ^{15}N NMR relaxation data show that D71N/R72E BIR1 is monomeric in solution, the dimeric species observed in the mass spectrum can be attributed to a covalent dimer formed by two D71N/R72E BIR1 monomers linked by an intermolecular disulfide bond.

Overall, our data indicate that the disulfide bond formed in the oxidized state involves C12, which resides in the flexible N-terminus. The ^{15}N -HSQC spectrum of oxidized D71N/R72E BIR1 is essentially identical to that of the reduced form, suggesting that the structure of D71N/R72E BIR1 is not perturbed upon oxidation. Indeed, only the chemical shifts of T11 to V13 vary significantly, while the other residues are not essentially affected (Figure S4). In contrast, the ^{15}N -HSQC spectrum of WT BIR1 is significantly affected, both in the dispersion and line-shape of the cross-peaks (Figures S2 and S4). In particular, residues 26–30 residing in the first α -helix are broader in the oxidized form, while the residues close to the dimer interface D59, R62 and C63 become narrower. Gel filtration chromatography showed that reduced and oxidized D71N/R72E mutant eluted at 31.5 and 28.8 min, respectively (Figure S5), consistent with the size increase between the monomeric protein and the covalent dimer. In contrast, the elution times of reduced and oxidized WT BIR1 were 30.2 and 31.5 min, respectively (Figure S5), suggesting that the formation of an intra-dimeric disulfide in the WT BIR1 dimer increases its compactness.

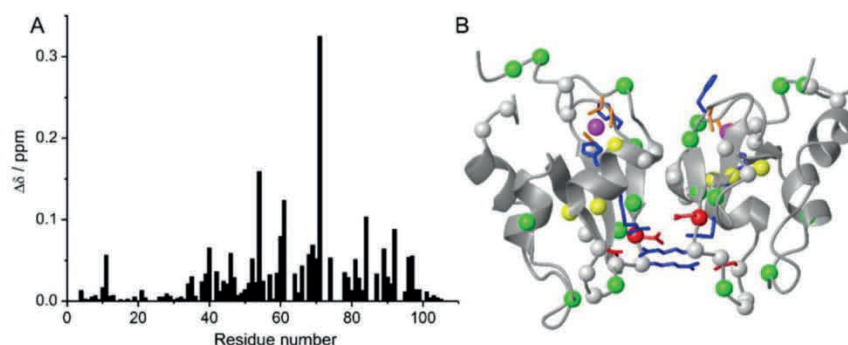


Figure 2. Chemical shift perturbations of D71N/R72E mutant on BIR1. (A) Plot of chemical shift perturbations caused by D71N/R72E mutation on BIR1 with the function of amino acid sequence. The chemical-shift differences between WT and D71N/R72E BIR1 were calculated as $\delta = ((\Delta\delta_H)^2 + (\Delta\delta_N/10)^2)^{1/2}$. (B) Chemical shift differences between WT BIR1 and D71N/R72E mutant plotted on the dimeric structure of BIR1 (PDB code: 2QRA)¹³, of which the C α atoms are shown in red spheres with $\delta > 0.2$ ppm, yellow spheres with $0.1 < \delta \leq 0.2$ ppm, green spheres with $0.05 < \delta \leq 0.1$ ppm, respectively. The unassigned C α resonances in WT BIR1 were shown in grey spheres.

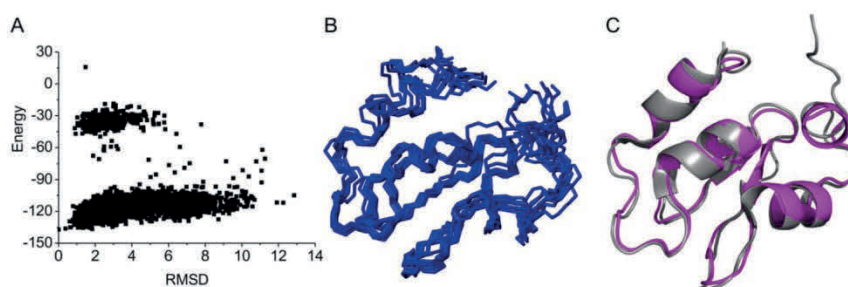


Figure 3. Solution structure of D71N/R72E BIR1 determined by CS-Rosetta. (A) Plot of Rosetta all atom energy versus C β RMSD relative to the lowest energy model. (B) Ensemble structural representation of 10-lowest energy conformations of D71N/R72E BIR1 calculated by CS-Rosetta. (C) Structural comparison of the lowest energy solution structure of D71N/R72E BIR1 from CS-Rosetta calculation (magenta) and X-ray crystal structure of WT BIR1 (grey) (PDB code: 2QRA)¹³.

To further characterize the quaternary structure of oxidized BIR1, backbone ^{15}N relaxation rates R_1 and R_2 were measured on oxidized WT BIR1 (Fig. 4). The latter presents a slightly smaller τ_c than the reduced state (16.4 ns vs 17.5 ns), confirming that the formation of an intramolecular disulfide bond between two C12 results in a more compact structure of the dimer. On the contrary, oxidation of the D71N/R72E mutant leads to an increase of τ_c from 7.3 ns to 11.8 ns. These relaxation results are in excellent agreement with the elution times from gel filtration experiments (Figure S5).

Redox potential measurement. To determine the redox properties of BIR1, we measured the redox potential of C12 for both WT and mutant BIR1 by NMR, using DTT as the reducing reagent. The cross-peaks of V13 in the two forms were used to quantify reduced and oxidized BIR1. The determined standard redox potential of WT BIR1 and D71N/R72E mutant were -304 ± 7 and -296 ± 8 mV, respectively (Tables S1 and S2). Notably, this redox potential is quite low, and is close to that of the cytosol of human cells (-315 mV), as determined by the pool of GSH¹⁶.

To better simulate the intracellular conditions, we tested the reaction of GSH and oxidized BIR1 in solution, and found that GSH could not reduce oxidized BIR1 to its reduced form. In contrast, this reaction formed a mixed disulfide bond between GSH and BIR1, which was characterized by MALDI-TOF spectrometry (Figure S6). The complex of BIR1-GSH in ^{15}N -HSQC spectra showed different spectral pattern from that of either oxidized or reduced of BIR1.

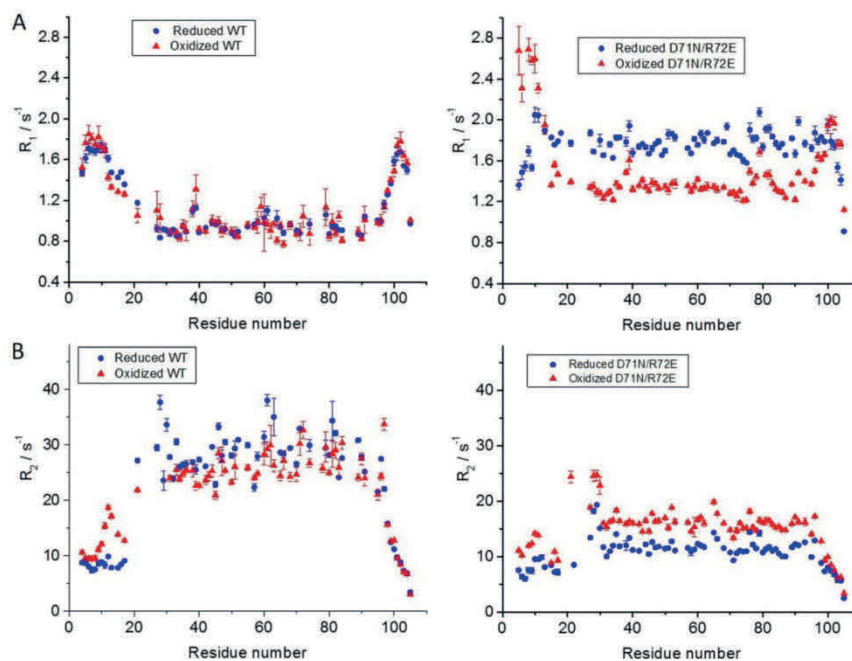


Figure 4. Relaxation rates of backbone ^{15}N measured for BIR1 at 298 K in different conditions. (A) R_1 of WT BIR1 and D71N/R72E mutant in the oxidized and reduced states. (B) R_2 of WT BIR1 and D71N/R72E mutant. The protein concentration was about 0.3 mM in 20 mM Bis-Tris buffer at pH 6.5.

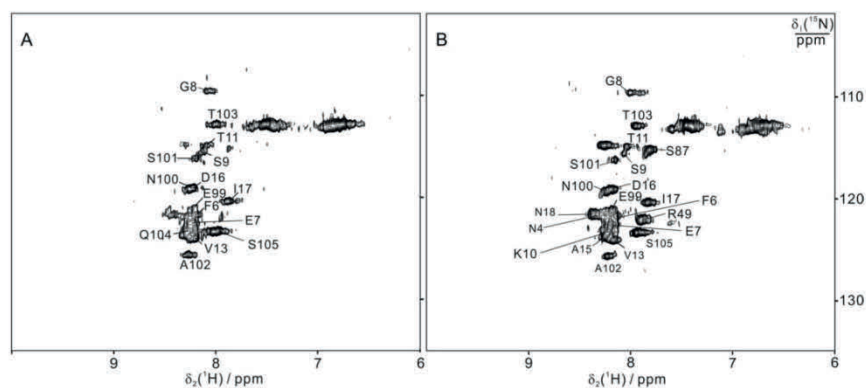


Figure 5. In cell ^{15}N -HSQC spectra recorded in oocytes via microinjection at 298 K. (A) WT BIR1; (B) D71N/R72E mutant.

BIR1 presents reduced form in living cells. In order to assess whether the low redox potential of BIR1 affects its intracellular redox state, we carried out in-cell NMR experiments in living *E. coli* cells, *Xenopus laevis* oocytes, and cultured HEK293T cells, to determine the oxidation state of BIR1 in different cellular environments. In the various types of cells, the residues in well-structured regions of BIR1 did not give rise to detectable cross-peaks in the ^{15}N -HSQC spectra, whereas a number of flexible residues in the N- and C-termini could be detected (Figs 5 and 6). In the cellular environment of *E. coli*, which has been reported to be more crowded than that of eukaryotic cells¹⁷, no signals from BIR1 are present, as all the observed cross-peaks arise from background intracellular species (Figure S7). These data indicate that, as is often the case for globular proteins^{18,19}, BIR1

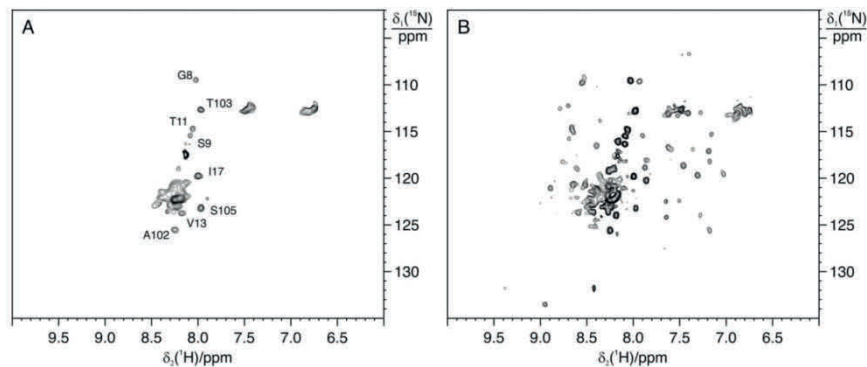


Figure 6. ^{15}N SOFAST-HMQC spectra of WT BIR1 in HEK293T cells and cell lysate. (A) On a sample of HEK293T cells expressing WT BIR1 and (B) on the corresponding cell lysate.

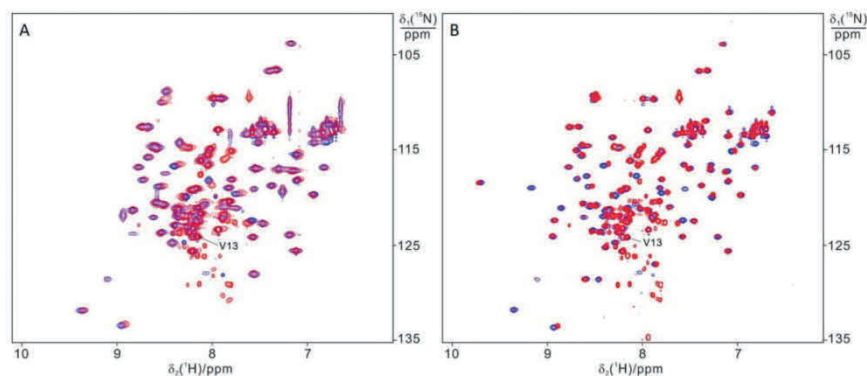


Figure 7. Comparison of ^{15}N -HSQC spectra of BIR1 recorded for protein samples prepared from *in vitro* (blue) and in *E. coli* lysate (red). (A) WT BIR1; (B) D71N/R72E mutant. NMR spectra were recorded at 298 K with a proton frequency of 600 MHz.

interacts with other cellular components, either with functional partners or non-specifically, causing broadening beyond detection of the NMR signals of the folded region.

To better assess the redox state of intracellular BIR1, we analyzed the NMR spectra of BIR1 in the cell lysates, which produced high quality NMR spectra for both WT BIR1 and D71N/R72E mutant, as the association of BIR1 with the cellular components was remarkably diminished upon cell lysis (Figs 6 and 7). Comparing ^{15}N -HSQC spectra recorded *in vitro* with those of the cell lysates, all the residues showed negligible chemical shift changes with respect to the spectra of reduced BIR1, both in WT and D71N/R72E mutant. The oxidized form, which has clear chemical shift differences for the residues close to C12 (Figure S2), was not detected. These results suggest that in the cytoplasm, under basal conditions, the majority of BIR1 is in the reduced form. Nevertheless, the low redox potential of C12 likely makes the XIAP BIR1 domain prone to oxidation as a consequence of cellular stress phenomena.

Effect of copper on BIR1 structure. XIAP has been shown to regulate cellular copper homeostasis, and recent data suggested a direct interaction between copper and XIAP^{11,12}. It has been hypothesized that copper binding occurs either by displacement of Zn(II) in the zinc finger, or at additional sites on the surface. With these premises, we investigated the effect of copper on BIR1 *in vitro* at atomic resolution by NMR spectroscopy. The effect of Cu(II) was first characterized on both WT and mutant BIR1. As shown in Fig. 8, the addition of copper to the solution of either WT BIR1 and D71N/R72E mutant resulted in significant chemical shift perturbations.

New cross-peaks appeared, while some others were broadened in the ^{15}N -HSQC spectra of both WT and D71N/R72E mutant (Fig. 8). As to WT BIR1, residues at the N-terminal segments containing T11, C12, V13 as well as E21, E22 and E26 experienced dramatic chemical shift changes upon addition of Cu(II) (Fig. 8A). In contrast to WT BIR1, D71N/R72E has less significant chemical shift perturbations as shown in Fig. 8B. It is noted that the residues in the zinc binding motif (C63, C66, H83 and C90) experienced no observable chemical shift changes or variations on cross-peak intensity upon titration with copper (Fig. 8B). Notably, the spectra of Cu(II)-treated BIR1 samples are almost identical to those of the oxidized state (shown in Figure S2). Chemical shift mapping

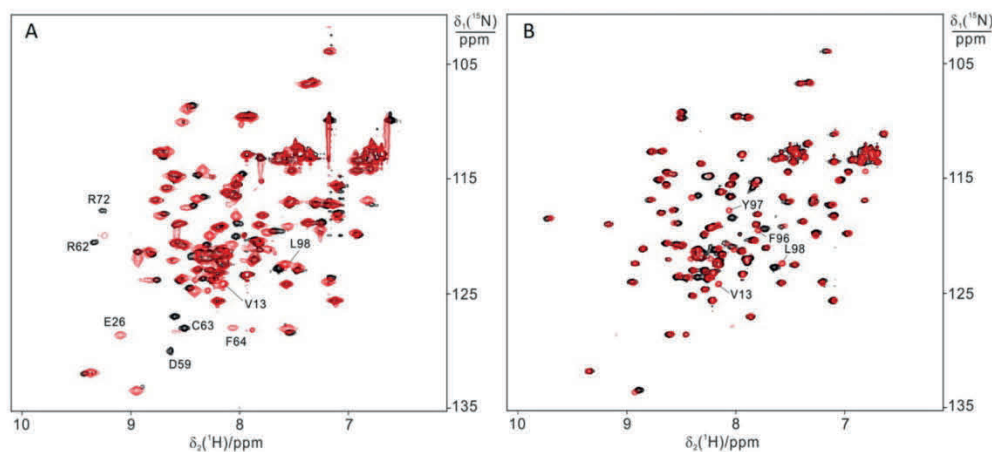


Figure 8. ^{15}N -HSQC spectra recorded for the solution of 0.2 mM protein in the absence (red) and presence (black) of 0.1 mM copper sulfate. (A) 0.2 mM WT BIR1; (B) 0.2 mM D71N/R72E. NMR spectra were recorded in 20 mM Bis-Tris, at pH 6.5 and at 298 K, with a proton frequency of 600 MHz.

analysis confirmed this observation (Figure S4). It is noted that some residues close to the zinc binding motif including R62, C63 and F64 also experienced minor chemical shift perturbations, which is probably an indirect consequence of the disulfide bond formation between C12 in the two subunits in WT BIR1. The oxidation of C12 was further confirmed by the fact that the addition of DTT to the mixture of Cu(II)-treated BIR1 samples reproduced the reduced state of BIR1 as determined by ^{15}N -HSQC spectra (data not shown). In order to determine whether direct copper binding had occurred, the samples were washed to remove external copper ion with 20 mM Bis-Tris buffer and then analyzed by atomic absorption spectroscopy. No copper was determined in the protein samples, confirming that direct copper binding did not occur.

To further confirm that Cu(II) oxidizes BIR1 at C12, a triple mutant (C12A/D71N/R72E) was analyzed (Figure S8). Incubation of the triple mutant with Cu(II) did not produce any of the expected perturbations for the NMR signals in the ^{15}N -HSQC spectrum (Figure S8), nor any difference in elution time as observed by gel filtration chromatography (Figure S8C). The interaction of BIR1 with Cu(II) resulting in oxidation of BIR1 rather than forming stable complex BIR1 is not buffer dependent, since both phosphate and Bis-Tris buffer produced almost identical chemical shift perturbations on protein signals as shown in the ^{15}N -HSQC spectra (Figure S9).

Prompted by these interesting results, we analyzed the effect of Cu(I) on the structure of BIR1. The addition of one equivalent of Cu(I) to BIR1 in oxygen-free conditions caused the formation of precipitates, even at low (50 μM) protein concentration. NMR analysis of the residual soluble protein showed that most signals of both WT BIR1 and D71N/R72E mutant were broadened, except those of the residues at the flexible N- and C-termini (Figure S10). No chemical shift perturbation was observed, suggesting the absence of binding sites with high affinity for Cu(I).

Taken together, our data indicate that Cu(II) does not either substitute the zinc ion in the zinc finger motif or bind specifically with BIR1, but it serves as oxidant of C12 in formation of a disulfide bond. These results are in contrast with the previous findings stating that copper is capable of replacing zinc ion in the zinc finger motif or to bind to thiol groups of XIAP^{11,12}.

The effect of Cu(II) on BIR1 was also investigated in the *E. coli* lysate and compared with the *in vitro* data. Addition of up to 0.5 mM Cu(II) into the cell lysate produced no detectable changes of NMR resonances as monitored by ^{15}N -HSQC spectra. At higher copper concentrations, line broadening effects were observed for some cross-peaks, including C12. A few new cross-peaks were generated (Figure S11), which correspond to those arising from the BIR1-GSH complex, as the spectra are almost identical to those of BIR1 oxidized *in vitro* with excess of GSH. The formation of BIR1-GSH was confirmed by MALDI-TOF mass spectrometry (Figure S6), and is consistent with the high abundance of GSH in the cytoplasm and in the cell lysates.

The ability of Cu(II) to oxidize C12, both *in vitro* and in the cell lysates, forming either an inter-subunit disulfide bond or a complex with GSH suggests an interesting, previously unreported, property of XIAP. The sequence alignment of the first domain of XIAP from human, rat, cow, mouse, dog and *Xenopus laevis* (Figure S12) reveals that, in addition to the well-conserved residues forming the zinc finger motif, there is a conserved TCVP motif in four out of six species, suggesting that this motif may exert a kind of function that has not been explored yet.

Summary

In this study, using high-resolution NMR spectroscopy, we show that the BIR1 domain of human XIAP forms a homodimer in solution, in accordance with the X-ray crystal structure. The dimer is destabilized by removing two salt bridges at the binding interface, resulting in the monomeric D71N/R72E mutant. In both WT and mutant

BIR1, the first 19 residues at the N-terminus are flexible in solution. These flexible residues are invisible in the X-ray structures both in its free state and in complex with TAB1. A TCVP motif was identified in the N-terminal unstructured segment, which is conserved among XIAP orthologues and likely plays an important role in the interaction with copper. Cysteine 12 in the TCVP motif is prone to oxidation, resulting in the formation of a disulfide bond between two BIR1 subunits, or in the formation of a mixed BIR1-GSH disulfide bond in a physiological environment. The redox potential of C12, ~ -300 mV, is lower than the generally known cysteine-related reductases, and comparable to that of the human cytosol. Considering the suggested role of XIAP in copper homeostasis, we further investigated the interaction of BIR1 with copper. In contrast to previous findings, the zinc ion bound to BIR1 is not replaced by Cu(II) or Cu(I), and the zinc finger domain has negligible changes upon interaction with copper. Cu(I) binding occurs non-specifically and with low affinity, therefore it is unlikely that BIR1 directly binds copper in a physiological environment. Instead, Cu(II) is able to oxidize C12 both in buffer and in the cell lysate.

These findings suggest a novel regulation mechanism of XIAP that deserves to be further investigated, in which C12 oxidation would modulate the biological roles of XIAP in response to intracellular stimuli or changes in the redox environment.

Materials and Methods

Protein expression and purification. The cDNA encoding the sequence (1–105) of the XIAP, following the previous report⁷, was amplified and cloned into the pET-3a expression vector. The D71N/R72E and D71N/R72E/C12A mutants were made by PCR-based quick-change mutagenesis method and all the plasmids were confirmed via DNA sequencing. The recombinant vector was transformed into *Escherichia coli* BL21(DE3) CodonPlus strain, and single colonies were selected for ampicillin and chloramphenicol resistance.

¹⁵N-labeled protein was prepared by growing cells in M9 medium following an optimized high cell-density protocol²⁰. The bacteria were first grown in LB medium and when the cell density reached 0.6 O.D. at 600 nm, the cells were gently collected and washed with MilliQ water. The cells were then transferred in the M9 medium containing 160 mM Na₂HPO₄, 40 mM KH₂PO₄, 2 mM MgSO₄, 0.1 mM CaCl₂, a trace metal mixture²¹, 1% ¹²C-glucose (or ¹³C-glucose for ¹³C labeling), ¹⁵NH₄Cl (1 g/mL) and 0.1 mM ZnCl₂. The cells were allowed to recover by incubation at 30 °C for 1 h. Protein expression was subsequently induced by addition of isopropyl β-D-1-thio-galactopyranoside (IPTG) to a concentration of 1 mM. After 10 h incubation, the cells were harvested. Large fractions of BIR1 protein were shown as being precipitated in the inclusion bodies during the over-expression. The cell lysate was centrifuged and the precipitates were solubilized in a solution of 8 M urea, 20 mM dithiothreitol (DTT) and 20 mM PBS (pH 8). The protein was refolded by using a multistep dialysis against solutions containing 6 M urea, 20 mM PBS, pH 8.0, 0.1 mM ZnCl₂, and 0.2 mM DTT; 4 M urea, 20 mM PBS, pH 8.0, 0.1 mM ZnCl₂, and 0.2 mM DTT; 2 M urea, 20 mM PBS, pH 8.0, 0.1 mM ZnCl₂, and 0.2 mM DTT; and finally 20 mM PBS, pH 8.0, 0.1 mM ZnCl₂, and 0.2 mM DTT. The protein was purified through DEAE column followed by Superdex-75 gel filtration. The buffer was then exchanged with 20 mM Bis-Tris at pH 6.5.

NMR experiments and protein assignment. All NMR spectra were recorded at 298 K on a Bruker AV600 NMR spectrometer equipped with a QCI-cryoprobe unless noted elsewhere. The triple-resonance NMR experiments were performed on protein samples at concentration of 1 mM ¹⁵N,¹³C-BIR1 (both for WT BIR1 and D71N/R72E mutant) in 20 mM Bis-Tris buffer at pH 6.5. All the NMR spectra were processed with the Bruker Topspin 2.1 and analyzed using NEASY program in CARRA package²² and Sparky²³.

The backbone resonance assignments were obtained from the analysis triple resonances of 3D HNCA, HNCACB and CBCA(CO)NH together with NOESY-¹⁵N-HSQC spectra and crystal structure of BIR1⁷. Wild type BIR1 has broad NMR signals and the backbone assignment was achieved with the 3D crystal structure of BIR1⁷ and the completed assignments of BIR1 D71N/R72E mutant, since both wild type BIR1 and D71N/R72E mutant present similar long- and intermediate-range NOEs according to the crystal structure.

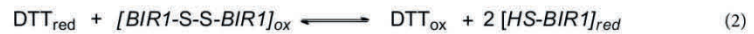
Backbone ¹⁵N-relaxation data of wild type BIR1 and D71N/R72E mutant were recorded at 298 K using standard experiments²⁴. The relaxation delays were 17, 34, 51, 68, 85, 102, 119 ms in the R₂ experiment and 3, 30, 150, 400, 550, 700, and 900 ms in the R₁ experiment. The complete set of R₁ and R₂ relaxation data was recorded in about 18 h per protein sample, using t_{1max} = 45 ms and t_{2max} = 110 ms for each spectrum.

Structure Calculations by CS-Rosetta. Software CS-Rosetta 3.2 protocol¹⁵ was applied to determine the 3D structure of D71N/R72E mutant using the backbone chemical shifts of ¹⁵N, ¹HN, ¹³CO, ¹³C_β, and ¹³CO (318 in total). Homology CS-RosettaCM calculations were performed based on the crystal structure of BIR1⁷; Zinc(II) was not added during the structural calculation. The convergence of the predicted models was established on the basis of plots of energy vs. backbone RMSD to the lowest energy ("best") structure following the established protocol¹⁵.

Oxidation of BIR1. The solution of 0.3 mM BIR1 (wild type or D71N/R72E) was dialyzed in 20 mM Tris buffer at room temperature, at pH 8.0, for 12 hours and the oxidation process was monitored by ¹⁵N-HSQC spectra. Analytical gel filtration measurements were performed on a Superdex 75 10/200 GL column (GE Healthcare Life Sciences) attached to an UPC-900 AKTA FPLC system in 20 mM Bis-Tris pH 6.5. Atomic absorption was analyzed on the Hitachi 180-80 Polarized Zeeman Atomic Absorption Spectrometer.

Redox potential measurement. The redox potential of BIR1 was measured by NMR-based titration of the protein with DTT in 100 mM PBS buffer at pH 7.0. ¹⁵N-labeled oxidized BIR1 samples (0.32 mM for BIR1 D71N/R72E and 0.28 mM for WT BIR1) were incubated with increasing concentrations of reduced DTT. At each titration point, one ¹⁵N-HSQC spectrum of BIR1 was recorded to measure peak heights for the oxidized and reduced populations of the BIR1. To make sure that the reactions have reached equilibrium, the mixtures in NMR

tubes were incubated at pH 7.0, at room temperature for 2 h prior to data acquisition. To reduce air oxidation, all solutions were degassed and the NMR tubes were purged with nitrogen. The BIR1 redox reactions for WT BIR1 and D71N/R72E can be described as the following:



when BIR1_{ox} was incubated with varying concentration of reduced DTT, the fractions of reduced BIR1_{red} , oxidized BIR1_{ox} , reduced DTT_{red} and oxidized DTT_{ox} in equations (1) and (2) were determined as following. The concentration of reduced and oxidized BIR1 under equilibrium condition in equations (1) and (2) was determined by measuring the cross-peak intensity of residues in the ^{15}N -HSQC spectra following a linear relationship of cross-peak intensity versus the concentrations of protein, respectively. For WT BIR1, in equation (1), the concentration of oxidized DTT, DTT_{ox} , equals the concentration of reduced BIR1, BIR1_{red} , under equilibrium condition. As to D71N/R72E mutant, the concentration of DTT_{ox} , is half of that of BIR1_{red} , under equilibrium condition in equation (2). In the following expressions, $[\text{DTT}_{\text{red, total}}]$ represents the initial concentration of reduced DTT, and $[\text{BIR1}_{\text{ox, total}}]$ the initial concentration of oxidized BIR1, respectively. The standard potential E in equation (1) can be written as Nernst equation:

$$E^0 = E_{\text{DTT}}^0 - E_{\text{BIR1}}^0 = -\frac{RT}{nF} \ln Q,$$

where Q is the equilibrium constant in equations (1) and (2), R the gas constant ($8.315 \text{ J} \cdot \text{K}^{-1} \cdot \text{mol}^{-1}$), T the absolute temperature (298.15 K), n the number of transferred electrons (2) and F the Faraday constant ($9.649 \times 10^4 \text{ C} \cdot \text{mol}^{-1}$). Q can be rewritten as:

$$Q = \frac{[\text{BIR1}_{\text{red}}][\text{DTT}_{\text{ox}}]}{[\text{BIR1}_{\text{ox}}][\text{DTT}_{\text{red}}]}, \text{ for equation (1) and}$$

$$Q = \frac{[\text{BIR1}_{\text{red}}]^2 [\text{DTT}_{\text{ox}}]}{[\text{BIR1}_{\text{ox}}][\text{DTT}_{\text{red}}]} \text{ for equation (2),}$$

respectively, under equilibrium condition. The concentration of reduced and oxidized BIR1, and reduced and oxidized DTT can be determined following the linear relationship of cross-peak intensity of NMR signals to the concentration of protein, which is determined independently. Knowing the standard potential of DTT, $E_{\text{DTT}}^0 - 323 \text{ mV}^{25}$, the standard potential of BIR1 can therefore be determined.

In-cell *E. coli* NMR experiment. The expression system was the same as described above. The cells containing BIR1 vector were first grown in 200 mL LB until absorbance at 600 nm (OD_{600}) reached about 0.8 and the cells were gently collected by centrifuge (3000 rpm for 10 minutes). The cells were washed with MilliQ water and then resuspended in 50 mL M9 medium with ^{15}N - NH_4Cl as sole nitrogen source. After 20 minutes, the culture was induced with isopropyl β -D-thiogalactopyranoside (IPTG) to a final concentration of 1 mM. After 3 h, a 10 mL aliquot was pelleted at 3000 rpm for 10 min at 4 °C. The pellet was then resuspended in 0.5 mL of 20 mM Bis-Tris, pH 6.4 and 10% D_2O . The remaining 40 mL culture was incubated with shaking for 5 h before processing as described above.

After obtaining in-cell NMR spectra, the cells were pelleted immediately by centrifuge at 5000 rpm for 5 min at 4 °C. The supernatant was checked for protein leakage by NMR. The resulting cell pellets were resuspended in 1 mL 20 mM Bis-Tris buffer at pH 6.5 and lysed with sonication. The cell lysate was harvested by centrifugation at 14000 g for 10 min at 4 °C and the supernatant was applied for NMR measurement.

Preparation of bacterial cell lysate. *E. coli* cells were first grew in 600 mL LB media and then in 100 mL M9 medium. The cells were collected and washed with lysate buffer (20 mM Bis-Tris, pH 6.5 free from reducing reagent like DTT or TCEP). Then the cells were mixed with 2 mL lysate buffer and the mixture was sonicated in an ice bath with cooling intervals between sonication bursts. The sonication cycle was repeated until the suspension became partially clear. Then the solution was centrifuged at 12000 rpm for 15 min at 4 °C. The supernatant was carefully transferred to an NMR tube for measurement.

In *Xenopus laevis* oocytes NMR measurement of BIR1. The in-cell NMR sample preparation was based on the previously established protocol^{26–28}. The solution of 0.2 mM ^{15}N -labeled BIR1 samples (about 550 μL) was lyophilized and then dissolved in 30 μL MilliQ water without further adjusting the pH. The protein concentration for micro-injection was typically about 3.6 mM. Each oocyte was injected with $\sim 30 \text{ nL}$ of $\sim 3.6 \text{ mM}$ ^{15}N -enriched proteins via an IM-300 microinjector (Narishige Co. Ltd., Tokyo, Japan). Injected oocytes (about 200) were put into a 5 mm Shigemi NMR tube containing ND96 buffer (96 mM NaCl, 2 mM KCl, 1.8 mM CaCl_2 , 1 mM MgCl_2 , 5 mM HEPES, pH 7.4) plus 10% D_2O . After the in-cell NMR experiments, about 200 μL of buffer above the oocytes was suctioned for a protein leakage test. No leakage was observed after NMR measurement.

In-cell NMR in HEK293T cells. The gene of WT BIR1 (encoding the a.a. 1–105) was cloned into the pHLsec vector²⁹ between EcoRI and XhoI restriction sites, and was verified by DNA sequencing. Samples for in-cell NMR were prepared following a reported protocol^{30–32}. Briefly, adherent HEK293T cells were grown on uncoated 75 cm² plastic flasks at 37 °C in 5% CO₂ atmosphere, and were maintained in Dulbecco's Modified Eagle's medium (DMEM; high glucose, D6546, Sigma) supplemented with L-glutamine, antibiotics (penicillin and streptomycin) and 10% FBS (Gibco). Cells were transiently transfected with the pHLsec plasmid containing BIR1, using polyethylenimine (PEI) in the ratio 1:1, in ¹⁵N labelled media (BioExpress6000), supplemented 2% FBS and Zn(II) as ZnSO₄, to a final concentration of 10 μM. After 48 h, the cells were collected and placed in a 3 mm Shigemitsu NMR tube. After the NMR experiments, the cell lysates were obtained by freeze-thaw lysis in PBS buffer, followed by centrifugation at 15000 g. NMR experiments on intact cells and lysates were recorded at 298 K at a 950 MHz Bruker Avance spectrometer equipped with a TCI CryoProbe.

Interaction of BIR1 with copper. The interaction of BIR1 with copper(II) was analyzed by recording the ¹⁵N-HSQC spectra. ¹⁵N-HSQC spectra were recorded with addition of copper sulfate from a 10 mM stock solution into the solution of 0.2 mM BIR1 (either wild type or D71N/R72E). A number of ¹⁵N-HSQC spectra were recorded at the molar ratio of [Cu²⁺]/[protein] 0, 0.2, 0.6, 0.8, 1.0 and 1.2, respectively, in 20 mM Bis-Tris at pH 6.5. For comparison, mixture of ascorbic acid and copper sulfate (molar ratio 10:1) was added into the same concentration of BIR1, and ¹⁵N-HSQC spectra were recorded accordingly. The precipitates formed during the addition of copper were characterized by Atomic Absorption Spectroscopy (AAS).

To investigate the interaction of BIR1 with copper(I), BIR1 proteins were treated with tetrakis(acetonitrile)copper(I) hexafluorophosphate, [Cu(I)(CH₃CN)₄]PF₆, which was made of 50 mM stock solution in acetonitrile. The samples of 0.15 mM ¹⁵N-labeled BIR1 proteins in the absence and presence of one equivalent of Cu(I) were made in a glove box without oxygen, and were analyzed by ¹⁵N-HSQC spectra.

Interaction of BIR1 with copper(II) in cell lysates. To investigate the interaction of BIR1 and copper (II) in a cell lysate, *E. coli* cells expressing ¹⁵N labeled BIR1 (wild type or D71N/R72E) were lysed in 20 mM Bis-Tris buffer at pH 6.5 without DTT. The obtained lysate was centrifuged and the supernatant was analyzed by NMR. A solution of copper sulfate was then added to the lysate and ¹⁵N-HSQC spectra were recorded subsequently.

References

- Schimmer, A. D. *et al.* Targeting XIAP for the treatment of malignancy. *Cell Death and Differentiation* **13**, 179–188 (2001).
- Fulda, S. & Vucic, D. Targeting IAP proteins for therapeutic intervention in cancer. *Nat. Rev. Drug Disc.* **11**, 109–124 (2012).
- Riedl, S. J. *et al.* Structural basis for the inhibition of caspase-3 by XIAP. *Cell* **104**, 791–800 (2001).
- Huang, Y. *et al.* Structural basis of caspase inhibition by XIAP: differential roles of the linker versus the BIR domain. *Cell* **104**, 781–790 (2001).
- Chai, J. *et al.* A conserved XIAP-interaction motif in caspase-9 and Smac/DIABLO regulates caspase activity and apoptosis. *Cell* **104**, 769–780 (2001).
- Srinivasula, S. M. *et al.* A conserved XIAP-interaction motif in caspase-9 and Smac/DIABLO regulates caspase activity and apoptosis. *Nature* **410**, 112–116 (2001).
- Lu, M. *et al.* XIAP induces NF-κB activation via the BIR1/TAB1 interaction and BIR1 dimerization. *Molecular cell* **26**, 689–702 (2007).
- Galbán, S. & Duckett, C. S. XIAP as a ubiquitin ligase in cellular signaling. *Cell Death Differentiation* **17**, 54–60 (2010).
- Robinson, N. J. & Winge, D. R. Copper metallochaperones. *Ann. Rev. Biochem.* **79**, 537–562 (2010).
- Burstein, E. *et al.* A novel role for XIAP in copper homeostasis through regulation of MURR1. *EMBO J.* **23**, 244–254 (2004).
- Mufli, A. R. *et al.* XIAP Is a copper binding protein deregulated in Wilson's disease and other copper toxicosis disorders. *Molecular Cell* **21**, 775–785 (2006).
- Liang, Y. *et al.* Copper-binding properties of the BIR2 and BIR3 domains of the X-linked inhibitor of apoptosis protein. *J. Inorg. Biochem.* **140**, 104–110 (2014).
- Lin, S. C. *et al.* Crystal structure of the BIR1 domain of XIAP in two crystal forms. *J. Mol. Biol.* **372**, 847–854 (2007).
- Shen, Y., Delaglio, F. & Cornilescu, G. *et al.* TALOS plus: A hybrid method for predicting protein torsion angles from NMR chemical shifts. *J. Biomol. NMR* **44**, 213–223 (2009).
- Shen, Y. *et al.* Consistent blind protein structure generation from NMR chemical shift data. *Proc. Natl. Acad. Sci. USA* **105**, 4685–4690 (2008).
- Dooley, C. T. *et al.* Imaging dynamic redox changes in mammalian cells with green fluorescent protein indicators. *J. Biol. Chem.* **279**, 2284–22293 (2004).
- Theillet, F.-X. *et al.* Physicochemical properties of cells and their effects on intrinsically disordered proteins (IDPs). *Chem. Rev.* **114**, 6661–6714 (2014).
- Barbieri, L., Luchinat, E. & Banci, L. Protein interaction patterns in different cellular environments are revealed by in-cell NMR. *Scientific Reports* **5**, 14456–14456 (2014).
- Smith, A. E., Zhang, Z., Pielak, G. J. & Li, C. NMR studies of protein folding and binding in cells and cell-like environments. *Curr. Opin. Struct. Biol.* **30**, 7–16 (2015).
- Cao, C. *et al.* Selective ¹⁵N-labeling of the side-chain amide groups of asparagine and glutamine for applications in paramagnetic NMR spectroscopy. *J. Biomol. NMR* **59**, 251–261 (2014).
- Studier, F. W. Protein production by auto-induction in high-density shaking cultures. *Protein Expr. Purif.* **41**, 207–234 (2005).
- Rochus, K. PhD thesis, Diss. ETH Nr. 15947 (2004).
- Goddard, T. D. & Kneller, D. G. Sparky 3, University of California, San Francisco (2008).
- Farrow, N. A. *et al.* Backbone dynamics of a free and a phosphopeptide-complexed Src homology 2 domain studied by ¹⁵N NMR relaxation. *Biochemistry* **33**, 5984–6003 (1994).
- Szajewski, R. P. & Whitesides, G. M. Rate constants and equilibrium constants for thiol-disulfide interchange reactions involving oxidized glutathione. *J. Am. Chem. Soc.* **102**, 2011–2015 (1980).
- Selenko, P. *et al.* Quantitative NMR analysis of the protein G B1 domain in *Xenopus laevis* egg extracts and intact oocytes. *Proc. Natl. Acad. Sci. USA* **103**, 11904–11909 (2006).
- Ye, Y. *et al.* Direct observation of Ca²⁺ induced calmodulin conformational transitions in intact *Xenopus laevis* oocytes by ¹⁹F NMR spectroscopy. *Angew. Chem. Int. Ed. Engl.* **54**, 5328–5330 (2015).

28. Pan, B. *et al.* 3D structure determination of a protein in living cells using paramagnetic NMR spectroscopy. *Chem. Commun.* **52**, 10237–10240 (2016).
29. Aricescu, A. R., Lu, W. & Jones, E. Y. A time- and cost-efficient system for high-level protein production in mammalian cells. *Acta Crystallogr. D Biol. Crystallogr.* **62**, 1243–1250 (2006).
30. Banci, L. *et al.* Atomic-resolution monitoring of protein maturation in live human cells by NMR. *Nature Chem. Biol.* **9**, 297–299 (2013).
31. Luchinat, E. *et al.* In-cell NMR reveals potential precursor of toxic species from SOD1 fALS mutants. *Nature Commun.* **5**, 5502 (2014).
32. Barbieri, L., Luchinat, E. & Banci, L. Characterization of proteins by in-cell NMR spectroscopy in cultured mammalian cells. *Nature Protoc.* **11**, 1101–1111 (2016).

Acknowledgements

This work was supported by National Key R&D Program of China (2016YFA0501202) and the National Natural Science Foundation of China (21673122 and 21473095) to X.-C.S.

Author Contributions


X.C.S. and L.B. conceived the work; H.H.Z., Y.Y., M.M.H., X.W., S.N.C., J.L.C. and X.C.S. cloned the genes and performed the mutagenesis, overexpressed the protein and made the assignments; H.H.Z., M.M.H., X.W. and S.N.C. studied the interaction of BIR1 with copper *in vitro* and in *E. coli* lysate; H.M.M. and X.W. performed in-cell N.M.R. in *E. coli* cells; P.P. and E.L. performed the N.M.R. work in H.E.K. cells and analyzed the data; M.M.H., Ye.Y. and C.L. performed in-cell N.M.R. in oocytes; X.C.S., M.M.H. and H.H.Z. analyzed the N.M.R. data; X.C.S., E.L. and L.B. wrote the paper.

Additional Information

Supplementary information accompanies this paper at <https://doi.org/10.1038/s41598-017-16723-5>.

Competing Interests: The authors declare that they have no competing interests.

Publisher's note: Springer Nature remains neutral with regard to jurisdictional claims in published maps and institutional affiliations.

 **Open Access** This article is licensed under a Creative Commons Attribution 4.0 International License, which permits use, sharing, adaptation, distribution and reproduction in any medium or format, as long as you give appropriate credit to the original author(s) and the source, provide a link to the Creative Commons license, and indicate if changes were made. The images or other third party material in this article are included in the article's Creative Commons license, unless indicated otherwise in a credit line to the material. If material is not included in the article's Creative Commons license and your intended use is not permitted by statutory regulation or exceeds the permitted use, you will need to obtain permission directly from the copyright holder. To view a copy of this license, visit <http://creativecommons.org/licenses/by/4.0/>.

© The Author(s) 2017

Supplementary information

Solution structure and interaction with copper *in vitro* and in living cells of the first BIR domain of XIAP

Meng-Meng Hou^{a,*}, Panagis Polykretis^{b,*}, Enrico Luchinat^{b,c,*}, Xiao Wang^{a*}, Shen-Na Chen^{a*}, Hui-Hui Zuo^{a*}, Yin Yang^a, Jia-Liang Chen^a, Yansheng Ye^d, Conggang Li^d, Lucia Banci^e, Xun-Cheng Su^a

^aState Key Laboratory and Research Institute of Elemento-organic Chemistry, College of Chemistry, Collaborative Innovation Center of Chemical Science and Engineering (Tianjin), Nankai University, Tianjin 300071, China.

^bMagnetic Resonance Center – CERM, University of Florence, 50019 Sesto Fiorentino, Florence, Italy.

^cDepartment of Biomedical, Clinical and Experimental Sciences, University of Florence, 50134 Florence, Italy.

^dKey Laboratory of Magnetic Resonance in Biological Systems, State Key Laboratory of Magnetic Resonance and Atomic and Molecular Physics, National Center for Magnetic Resonance in Wuhan, Wuhan Institute of Physics and Mathematics, Chinese Academy of Sciences, Wuhan 430071, China.

^eDepartment of Chemistry, University of Florence, 50019 Sesto Fiorentino, Florence, Italy.

* These authors have contributed equally to this work.

Correspondance to: Lucia Banci, banci@cerm.unifi.it and Xun-Cheng Su, xunchengsu@nankai.edu.cn

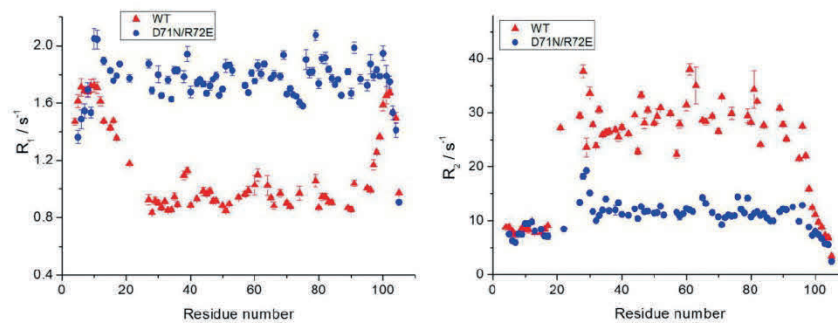


Figure S1. Relaxation measurements of BIR1. ^{15}N -relaxation rates measured for wild type BIR1 and D71N/R72E mutant at 298 K in 20 mM Bis-Tris buffer at pH 6.5, with a proton frequency of 600 MHz.

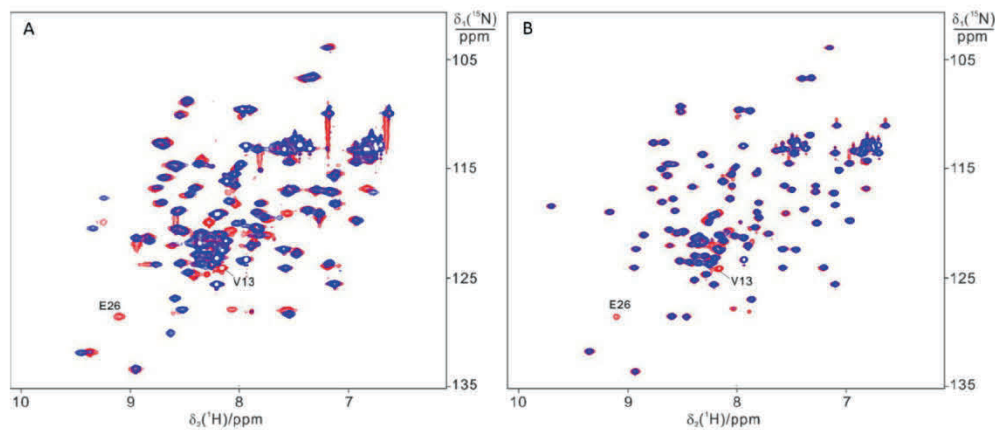


Figure S2. Comparison of oxidized and reduced BIR1. Superimposition of ^{15}N -HSQC spectra recorded for 0.2 mM ^{15}N -BIR1 in the reduced (red) and oxidized (blue) form. (A) WT BIR1; (B) D71N/R72E mutant. NMR spectra were recorded in 20 mM Bis-Tris at pH 6.5 and 298 K, with a proton frequency of 600 MHz. It is noted that in the oxidized state, the residues close to C11 including V13 experienced significant chemical shift changes and the chemical shift perturbations with the function of amino acid sequence are shown in Figure S4.

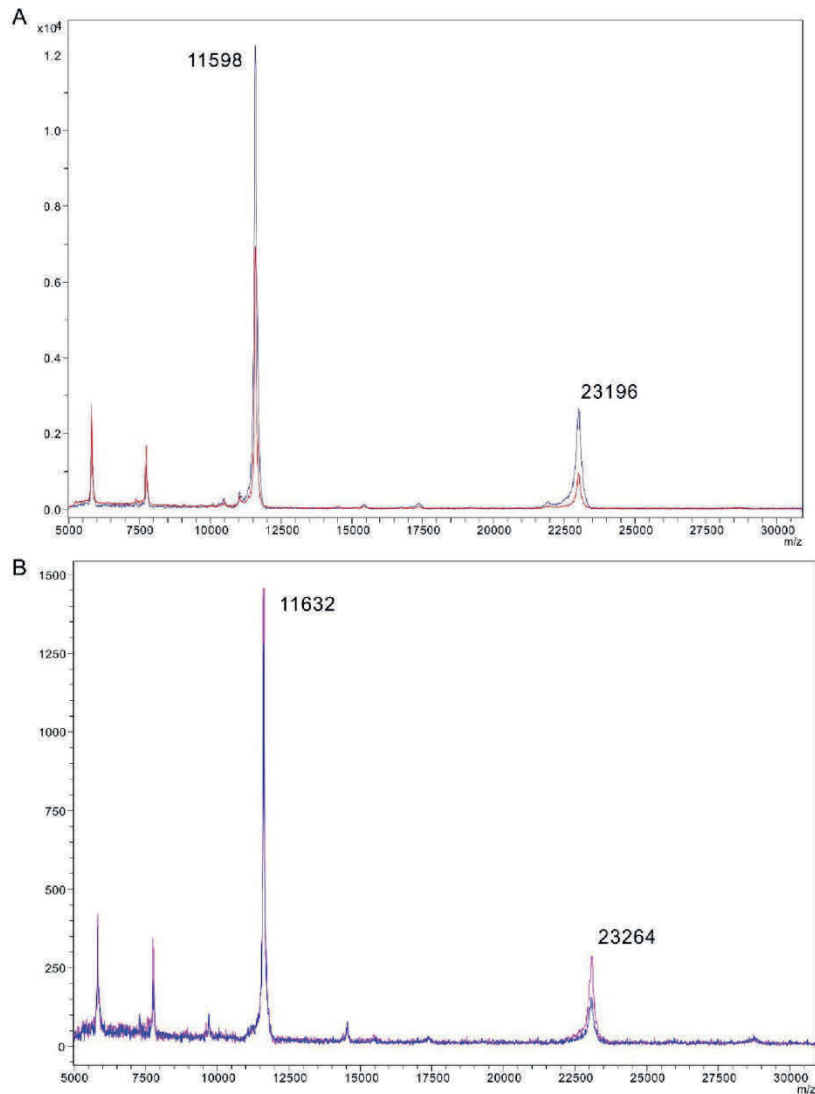


Figure S3. MALDI-TOF mass spectra recorded for the mixture of reduced and oxidized BIR1 and oxidized BIR1. (A) D71N/R72E: mixture of reduced and oxidized states (red) and oxidized state (blue). (B) WT BIR1: mixture of reduced and oxidized states (blue) and oxidized state (magenta). The spectra were recorded using matrix of α -cyano-4-hydroxycinnamic acid in water:CH₃CN (1:1) and 00.1% CF₃COOH, in which condition the zinc ion was released from protein due to low pH (about 3.5) and only free polypeptide was determined.

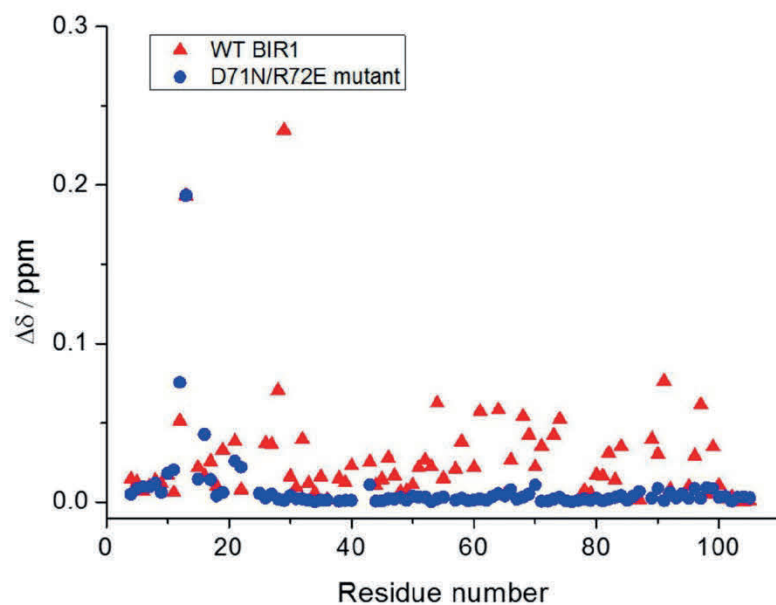


Figure S4. Chemical shift changes of BIR1 between the oxidized and reduced states with the function of amino acids. Chemical shift differences were calculated as $\Delta\delta = \text{Sqrt}[(\Delta\delta_{\text{H}})^2 + (\Delta\delta_{\text{N}}/10)^2]$, where $\Delta\delta_{\text{H}}$ and $\Delta\delta_{\text{N}}$ are the backbone amide chemical shift differences in the hydrogen and nitrogen dimension, respectively.

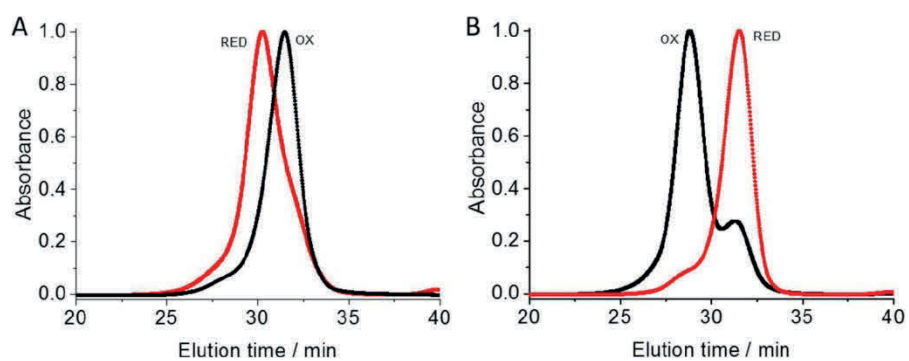


Figure S5. Gel filtration analysis of reduced and oxidized BIR1. Gel filtration profiles of reduced (red) and oxidized (black) WT BIR1 (A) and D71N/R72E (B), of which the absorption was monitored by UV lamp at 280 nm.

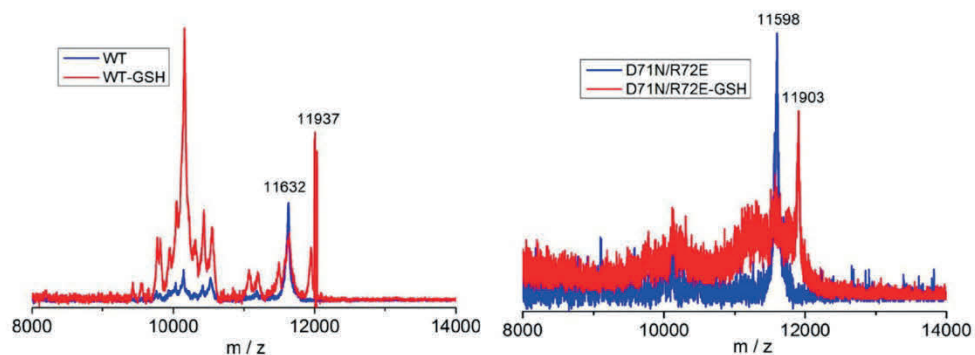


Figure S6. MALDI-TOF mass spectra analysis of oxidized BIR1 after treatment with GSH. Spectra were recorded for the reduced 0.1 mM WT BIR1 (left) and D71N/R72E mutant (right) and mixture of 0.1 mM oxidized WT BIR1 and D71N/R72E mutant and 0.2 mM GSH. The calculated molecular mass difference of 305 mass units between BIR1 and BIR1-GSH is identical to the difference of masses observed.

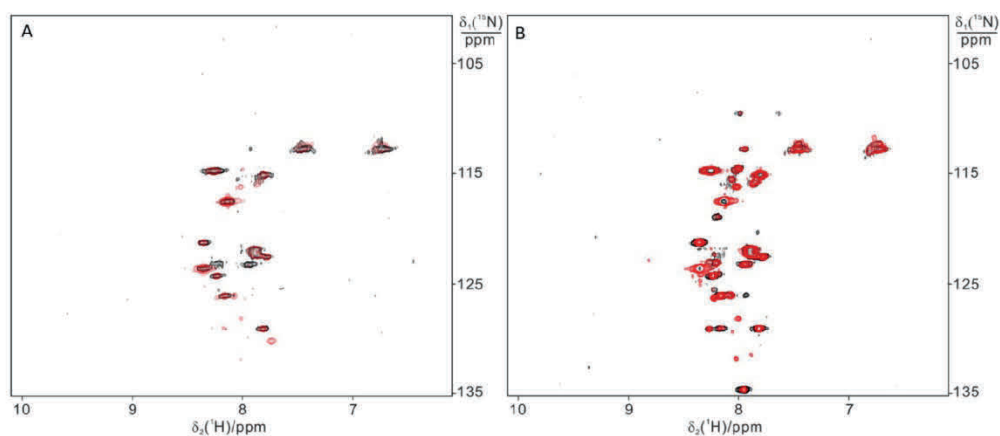


Figure S7. ^{15}N -HSQC spectra recorded in-cell living *E. coli* cells. The cells were collected before (red) and after (black) IPTG induction for NMR measurements. A) WT BIR1; B) D71N/R72E mutant. The NMR spectra were recorded at 298 K and in 20 mM Bis-Tris buffer at pH 6.5. In *E. coli* cells, even the NMR signals of the flexible regions of BIR1 were not determined.

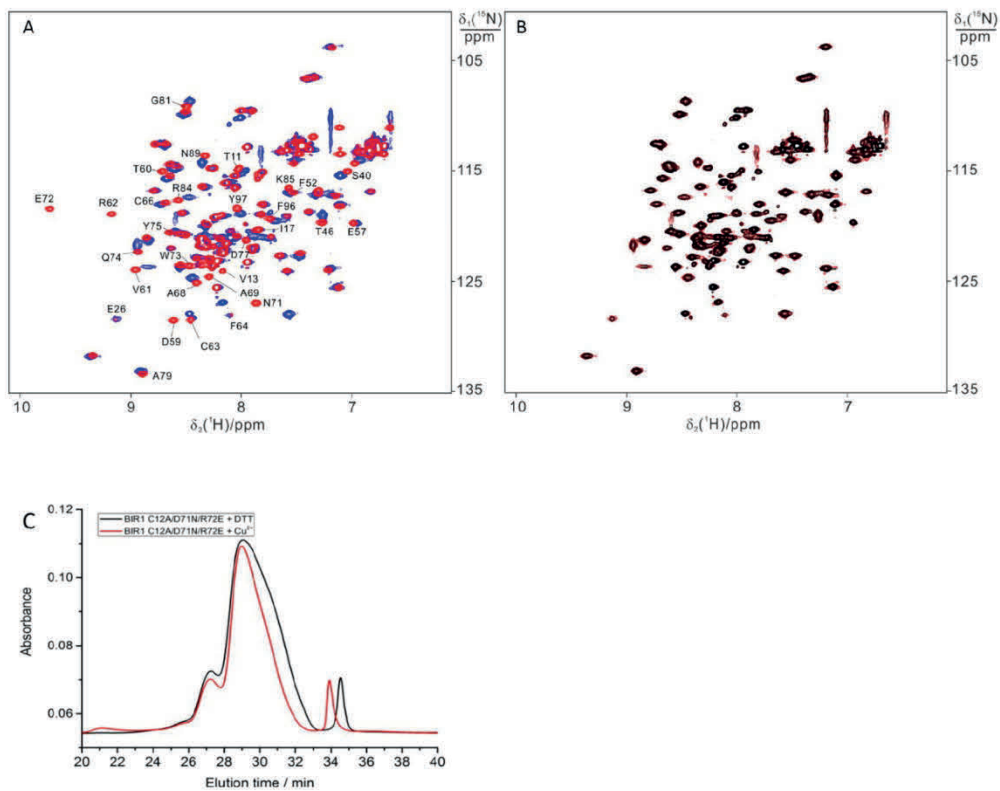


Figure S8. Comparison of BIR1 mutants in interaction with copper sulfate. (A) 0.2 mM D71N/R72E mutant (red) and 0.2 mM C12A/D71N/R72E mutant (blue), of which residues with large chemical shifts changes are labeled for D71N/R72E mutant. (B) 0.2 mM C12A/D71N/R72E mutant in the absence (red) and presence (black) of 0.5 mM copper sulfate. NMR spectra were recorded in 20 mM Bis-Tris at pH 6.5 and 298 K with a proton frequency of 600 MHz. (C) Gel filtration analysis of C12A/D71N/R72E mutant in interaction with copper (II). Gel filtration profiles of C12A/D71N/R72E mutant in the presence of 5 equivalents of DTT (black) and 0.6 equivalent of copper sulfate (red), respectively, of which the absorption was monitored by UV lamp at 280 nm. The protein samples treated with DTT or copper sulfate were incubated for 5 hours at room temperature prior to gel filtration experiment.

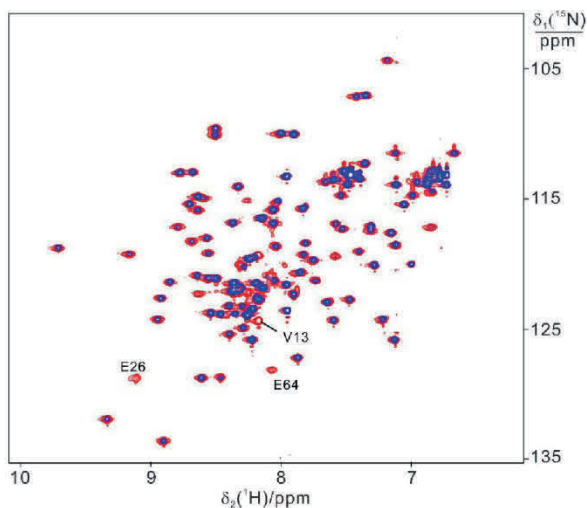


Figure S9. Interaction of BIR1 with copper sulfate is not buffer dependent. Superimposition of ^{15}N -HSQC spectra recorded for 0.1 mM D71N/R72E mutant (red) and after addition of 0.06 M CuSO_4 (blue) in 20 mM phosphate buffer at pH 7.0. NMR spectra were recorded in 20 mM phosphate buffer at pH 7.0 and 298 K with a proton frequency of 600 MHz.

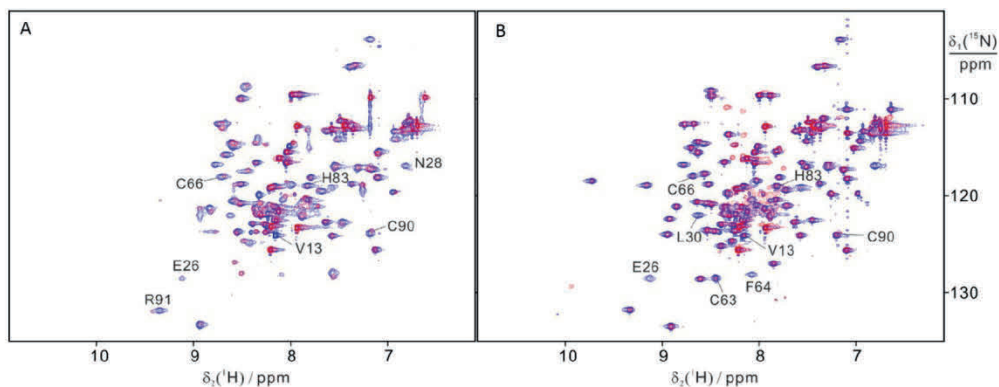


Figure S10. Superimposition of ^{15}N -HSQC spectra recorded for 0.15 mM BIR1 in the absence (blue) and presence of one equivalent of Cu(I) (red). (A) WT BIR1, (B) D71N/R72E mutant. NMR spectra were recorded in 20 mM Bis-Tris at pH 6.5 and 298 K with a proton frequency of 600 MHz and protein samples were made in glove box without O_2 , and Cu(I) stock solution was used as 50 mM $[\text{Cu}(\text{I})(\text{CH}_3\text{CN})_4][\text{PF}_6]$ in CH_3CN .

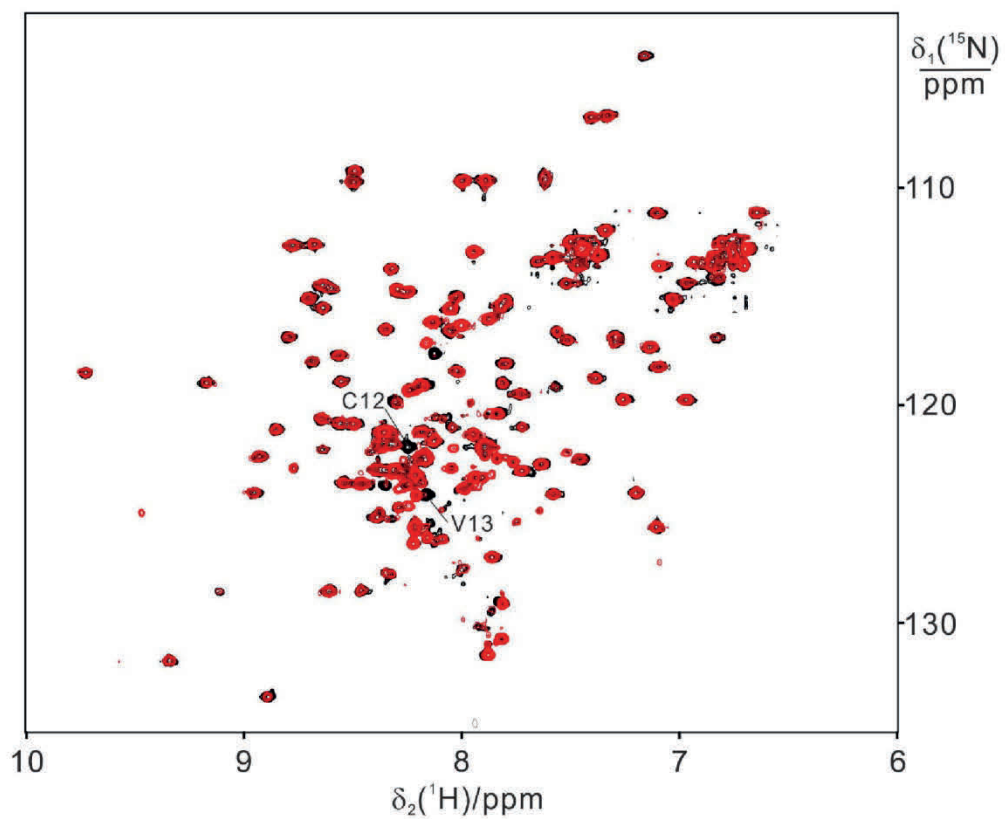


Figure S11. Interaction of D71N/R72E mutant with copper sulfate in *E. coli* cell lysate. Superimposition of ^{15}N -HSQC spectra recorded for cell lysate of D71N/R72E mutant (black) and after treatment with 1.0 mM CuSO_4 (red).



Figure S12. Structure based sequence alignment of XIAP BIR1 domain. The amino acid sequence of BIR1 (from the top to bottom) was from human, Rat, cow, mouse, dog and *Xenopus laevis*, respectively.

Table S1. Determined redox potential of Cys12 in wild type mutant by measuring the cross-peak intensity of Val13 in the reduced and oxidized BIR1 with respective concentration of DTT in 100 mM PBS at pH 7.0 and 298K.

[DTT _{red}] _o	[WT _{ox}]	[DTT _{red}]	[WT _{red}]	[DTT _{ox}]	E ⁰ (V)
mM	mM	mM	mM	mM	
0.12	0.11	0.04	0.16	0.08	-0.3126
0.1	0.12	0.02	0.16	0.08	-0.3015
0.08	0.16	0.03	0.10	0.05	-0.2990

Table S2. Determined redox potential of Cys12 in BIR1 D71N/R72E by measuring the cross-peak intensity of Val13 in the reduced and oxidized BIR1 with respective concentration of DTT in 100 mM PBS at pH 7.9 and 298K.

[DTT _{red}] _o	[DR _{ox}]	[DTT _{red}]	[DR _{red}]	[DTT _{ox}]	E ⁰ (V)
mM	mM	mM	mM	mM	
0.12	0.13	0.03	0.19	0.09	-0.3045
0.1	0.15	0.02	0.17	0.08	-0.2941
0.08	0.18	0.02	0.13	0.06	-0.2890

2.3 Characterization of XIAP-BIR3 interaction with CCS and copper

2.3.1 Overview

As mentioned above, XIAP has been reported to be involved in the intracellular homeostasis of copper (Burstein et al., 2004; Mufti et al., 2006, 2007; Galbán and Duckett, 2010; Liang et al., 2014). It has been proposed that at basal intracellular copper levels, XIAP binds and ubiquitinates the copper-free form of CCS through its BIR3 domain (Brady et al., 2010). Notably, this ubiquitination enhances its ability to deliver copper to SOD1, rather than triggering the degradation of CCS. On the contrary, at elevated copper levels, when the cellular pool of apo-SOD1 is depleted and the copper-bound CCS accumulates in the cytosol, XIAP ubiquitinates CCS at a different position, targeting it for degradation. In addition, XIAP ubiquitinates itself when bound to copper, also leading to its degradation (Fig. 8).

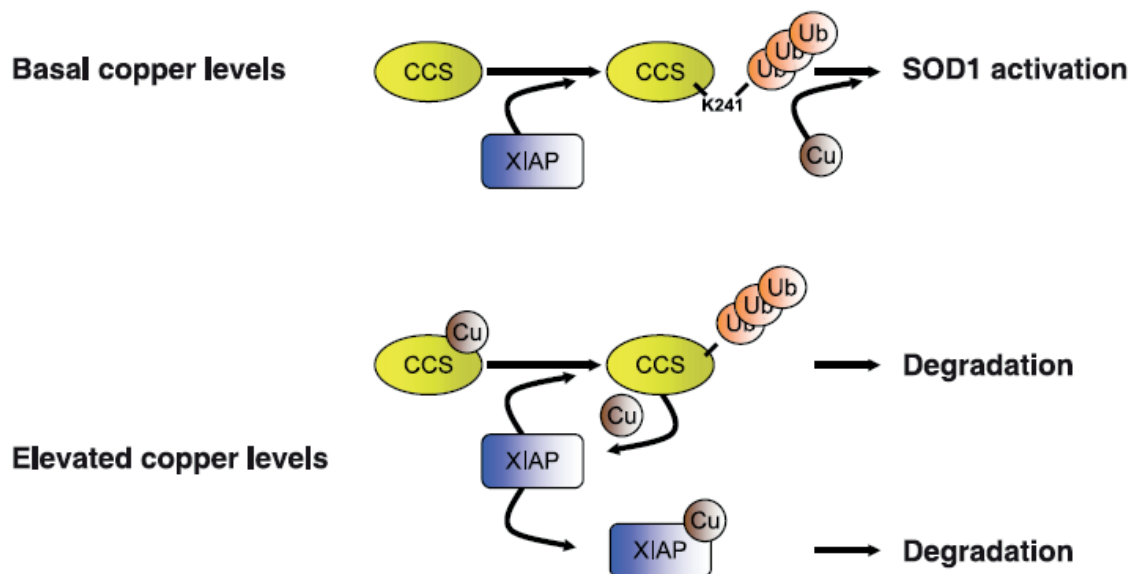


Fig. 8: Proposed model of CCS regulation by distinct ubiquitination pathways (image credit: Brady et al., 2010).

Furthermore, it has been hypothesized that, when the intracellular copper concentration is high, CCS interacts with BIR3 and transfers copper to XIAP (Fig. 8). Reportedly, copper-bound XIAP has a reduced activity and is thought that, under these conditions, it ubiquitinates itself promoting its own degradation, and triggering in this way the caspase-induced apoptosis (Brady et al., 2010). In summary, in the hypothesized mechanism two kinds of

ubiquitination occur: an enhancing one, at basal copper levels, and an inhibiting one at high intracellular copper levels. Such intriguing mechanism has not been proven at the molecular level, therefore the aim this study is to better investigate, through NMR spectroscopy, how the interaction between BIR3 and CCS occurs, and if this domain is able to bind copper.

2.3.2 Methodologies

In vitro experiments:

The gene of the BIR3 domain (encoding the a.a. 241-356 of human XIAP) was cloned in the pET-15 vector (for the expression in *E. coli* cells), between NdeI and XhoI restriction enzyme sites. The pET15-BIR3 plasmid was transformed in BL21 Rosetta (DE3) pLysS *E. coli* cells. The transformed bacteria were grown to mid-log phase at 37 °C and 180 rpm in M9 minimal medium, containing $(^{15}\text{NH}_4)_2\text{SO}_4$ as only nitrogen source, in the presence of 100 μM ZnSO_4 , and were induced with 0.5 mM isopropyl β -D-1-thiogalactopyranoside (IPTG). After induction the cells were grown for other 4 hours. Harvested cells were re-suspended in binding buffer (Tris 50 mM, NaCl 500 mM, Imidazole 20 mM, pH 7.5), supplemented with protease inhibitor tablets (Roche) and lysed via sonication (10'' ON, 50'' OFF, at 60% of amplitude for 40'). The lysate was loaded on a 5mL HisTrap FF affinity column, previously equilibrated with the binding buffer, and the protein was recovered with the elution buffer (Tris 50 mM, NaCl 500 mM, Imidazole 500 mM, pH 7.5). The His-tag was cleaved by incubating overnight with thrombin. Finally, BIR3 was transferred in NMR buffer (KPi 50 mM, NaCl 500 mM, DTT 5 mM, pH 6) using a desalting column. CCS, previously cloned in a pTH-27 plasmid, was expressed in BL21 (DE3) Codon Plus RIPL *E. coli* cells grown in unlabelled medium and then purified in the same NMR buffer of BIR3 (Banci et al., 2012).

2D ^1H - ^{15}N SOFAST-HSQC NMR spectra of BIR3 alone (145 μM , ^{15}N -labelled) were acquired on a 700 MHz Bruker Avance III spectrometer equipped with a TXO CryoProbe at 298 K. For monitoring the interactions with CCS and/or copper, ^1H - ^{15}N HSQC spectra of BIR3 titrated under anaerobic conditions with

1 eq. of CCS and/or 1 eq. of Cu(I) were acquired at the same spectrometer at 298 K.

In-cell NMR experiments:

For the in-cell NMR experiments, the sequence encoding the BIR3 domain (i.e. the a.a. 241-356 of human XIAP) was cloned into the pHLsec vector, between EcoRI and XhoI restriction enzyme sites. HEK293T cells were maintained in Dulbecco's modified Eagle's medium (DMEM; high glucose, D6546, Sigma) supplemented with L-glutamine, antibiotics (penicillin and streptomycin) and 10% FBS (Gibco) in uncoated 75 cm² plastic flasks and incubated at 310 K and 5% CO₂. Cells were transiently transfected with the pHLsec-BIR3 plasmid, using polyethylenimine (PEI) in the ratio 1:1, in ¹⁵N labelled medium (BioExpress6000), supplemented with 2% FBS (Banci et al., 2013). ¹H-¹⁵N SOFAST-HMQC spectra were acquired directly on living HEK293T cells (and lysates) on a 950 MHz Bruker Avance III spectrometer equipped with a TCI CryoProbe, at 298 K.

2.3.3 Results & Discussion

In vitro experiments:

The 2D NMR spectrum of BIR3 indicates that in solution the domain is well structured (Fig. 9a). In order to evaluate the interaction of BIR3 with copper, BIR3 was titrated with 1 eq. of Cu(I). The results of such experiment did not provided any evidence of an interaction between BIR3 and the metal (Fig. 9b). Next, in order to evaluate the interaction of BIR3 with CCS, BIR3 was titrated with one eq. of CCS, but even in this case no significant chemical shift perturbation was observed (Fig. 9c). Finally, to test whether a metal-mediated protein-protein interaction occurred, we added 1 eq. of Cu(I) in the aforementioned sample; again, no spectral changes were observed (Fig. 9d). Summarising, the results of this study did not provided any evidence of an interaction between BIR3 and CCS, and demonstrated that BIR3 is not able to bind Cu(I).

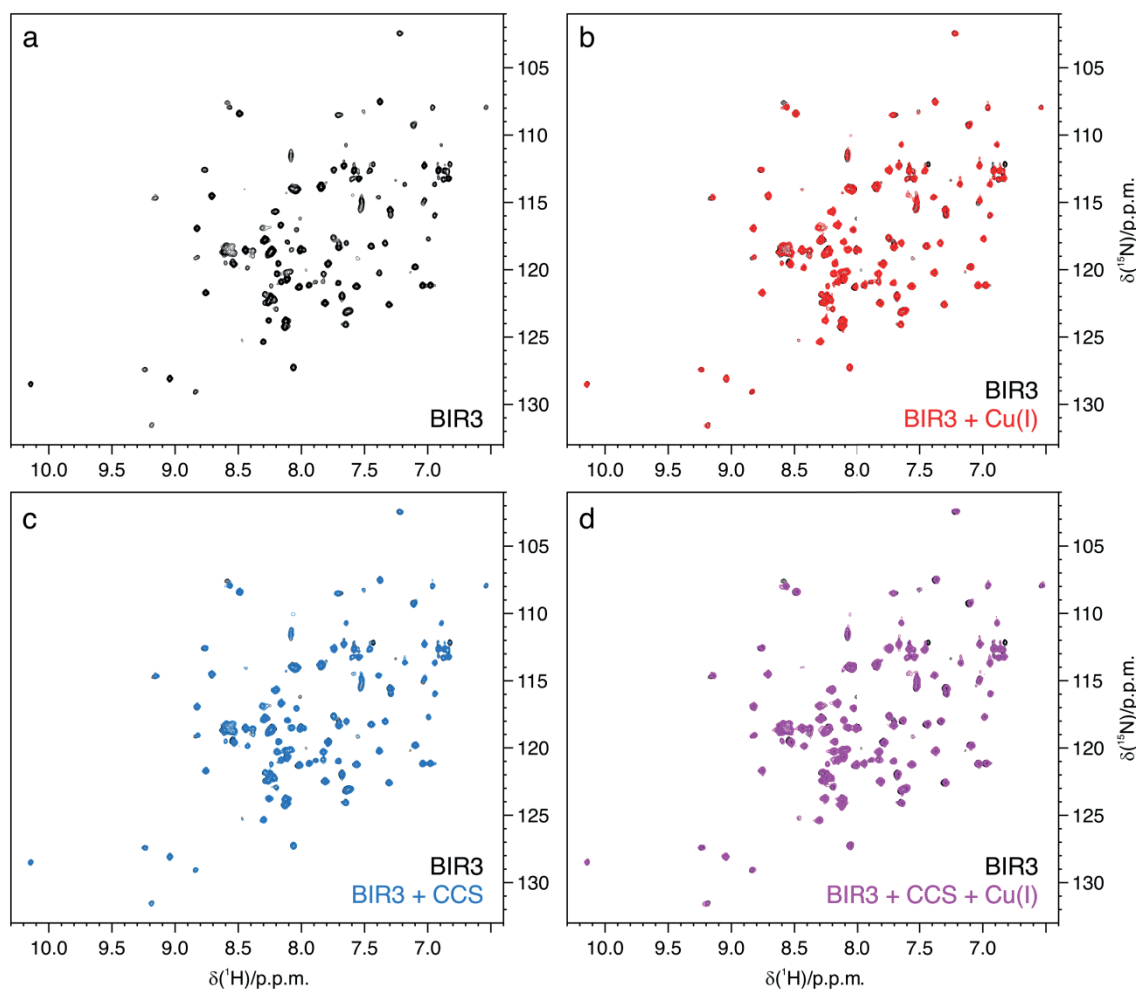


Fig. 9: **a**) ^1H - ^{15}N HSQC (700 MHz, 298 K) spectrum of solution BIR3 (145 μM); **b**) overlay of the ^1H - ^{15}N HSQC (700 MHz, 298 K) spectrum obtained from the titration of BIR3 (145 μM) with 1 eq. of Cu(I) (**red**), on the spectrum “a” (**black**); **c**) overlay of the ^1H - ^{15}N HSQC (700 MHz, 298 K) spectrum obtained from the titration of BIR3 (145 μM) with 1 eq. of unlabelled CCS (**blue**), on the spectrum “a” (**black**); **d**) overlay of the ^1H - ^{15}N HSQC (700 MHz, 298 K) spectrum obtained from the titration of BIR3 (145 μM) with 1 eq. of CCS and 1 eq. of Cu(I) (**magenta**), on the spectrum “a” (**black**).

In-cell NMR experiments:

The results obtained acquiring ^1H - ^{15}N SOFAST-HMQC spectra directly on living HEK293T cells suggest that the BIR3 domain, after its translation, interacts with a partner or a cellular structure which decreases its tumbling rate. This can be deduced from the fact that we identify fewer signals attributable to BIR3 in the spectra acquired on living cells, than in those acquired on the cell lysate and *in vitro* (Fig. 10).

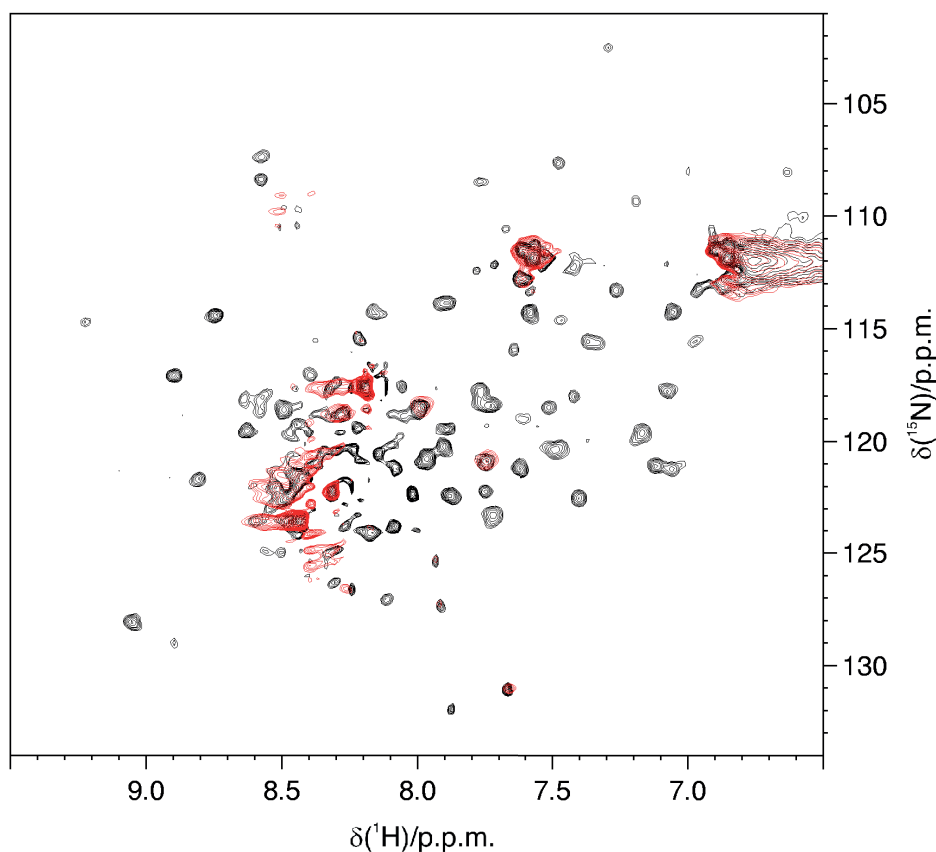


Fig. 10: Overlay of the 2D ^1H - ^{15}N SOFAST-HMQC (950 MHz, 298 K) spectra of BIR3 acquired on living HEK293T cells (**red**) and on the lysate (**black**).

2.3.4 Perspectives

In contrast with what previously reported, the results of the experiments performed on BIR3 did not provide any evidence of a specific interaction of such domain with Cu(I) and with CCS. This finding, combined with the fact that also BIR1 did not bind copper, prompted us to study the structural conformation of the full length XIAP, in order to address many questions that remain unexplained concerning: the structure of the full length protein; the ability of XIAP to bind copper and its binding sites; the conformational changes resulting from the hypothesised metal binding; and to determine if the interaction with Cu(I) and with CCS requires the entire protein to occur.

2.4 Structural characterization of full length XIAP integrating NMR, SAXS and EPR data.

2.4.1 Overview

A multitude of studies has been published on XIAP in the last two decades, and the structures of all the single domains of XIAP have been determined (Sun et al., 1999; Lu et al., 2007; Hui et al., 2010; Lukacs et al., 2013; Nakatani et al., 2013). Despite this, there is still no information about their spatial arrangement in the full length protein. XIAP is involved in many cellular processes in which exerts different functions: i) inhibition of the apoptotic cascade (Liston et al., 1996; Deveraux et al., 1997); ii) activation of NF- κ B pathway (Lu et al., 2007); iii) E3 ligase activity, through which XIAP regulates several important pathways, such as the inflammatory and cell death signalling (Witt and Vucic, 2017; Vucic, 2018); iiiii) involvement in copper homeostasis (Mufti et al., 2007). Taken together, all these processes require that in the cell XIAP constantly interacts with one or more different partners. Consequently, the conformation of the full length protein and the spatial arrangement of its domains could modulate differently the various interactions of XIAP. Therefore, it becomes of fundamental importance to determine the structural conformation of the full length XIAP, to better understand whether/how its many interactions are mutually influenced and how the arrangement of the various domains plays a role in its different functions. To this aim, we used an integrative approach combining structural techniques: NMR, SAXS and EPR with biophysical techniques: Size Exclusion Chromatography with Multi-Angle Light Scattering (SEC-MALS) and Inductively Coupled Plasma Atomic Emission Spectrometry (ICP-AES). Such integrated approach provided several types of information that allowed the structural characterization of full length XIAP. Specifically, SEC-MALS experiments demonstrated that in solution XIAP forms a 115 kDa homodimer, and ICP-AES confirmed that XIAP homodimer contains 10 zinc atoms. The NMR data suggested that only the inter-domain linkers of XIAP have a certain degree of flexibility, while the folded regions assume a rigid conformation of high molecular weight, not allowing the detection of signals

belonging to the structured domains. This is in accordance with the data obtained by EPR, since the broad components of the continuous wave spectra are the most abundant, suggesting that XIAP assumes a poorly flexible conformation in the regions where the paramagnetic tags are located (i.e. on BIR2 and BIR3). Finally, combined fitting of the SAXS data with DEER-EPR distance restraints provided a low resolution structure of the full length XIAP dimer, compatible with a discoidal and flat conformation. This study provides the first structural characterization of the XIAP homodimer, adding useful information that will help to elucidate the role of this multifunctional protein involved in many cellular processes.

2.4.2 Attached manuscript (in preparation - advanced version)

Structural characterization of full length XIAP by integrating NMR, SAXS and EPR data

Polykretis, P.^a, Luchinat, E.^{a,b}, Graewert, M. A.^c, Bonucci, A.^a, Giachetti, A. ^a, Svergun, D. I.^c, & Banci, L.^{a,d,1}

^aMagnetic Resonance Center - CERM, University of Florence, Via Luigi Sacconi 6, 50019 Sesto Fiorentino, Florence, Italy.

^bDepartment of Experimental and Clinical Biomedical Sciences "Mario Serio", University of Florence, Viale Morgagni 50, 50134 Florence, Italy.

^cEuropean Molecular Biology Laboratory (EMBL), Hamburg Outstation, Notkestrasse 85, 22607 Hamburg, Germany.

^dDepartment of Chemistry, University of Florence, Via della Lastruccia 3, 50019 Sesto Fiorentino, Florence, Italy.

¹To whom correspondence should be addressed. Telephone: +39 055 457 4273. Email: banci@cerm.unifi.it

Introduction

The X-chromosome linked Inhibitor of Apoptosis Protein (XIAP) is 497-residue cytoplasmic, zinc binding protein, ubiquitously expressed in human cells except peripheral blood leukocytes (Liston et al., 1996). XIAP contains three zinc-binding BIR (Baculovirus IAP Repeat) domains at the N-terminal region, an UBA (Ubiquitin Associated) domain and a C-terminal, zinc-binding RING (Really Interesting New Gene) domain.

XIAP is a member of the IAP family, and was first recognised as a potent inhibitor of apoptosis, impeding directly the proteolytic activity of caspases (Deveraux et al., 1997). More precisely, through its BIR2 domain and a portion of the linker between BIR1 and BIR2, XIAP binds and inhibits the effector caspases 3 and 7 (Sun et al., 1999; Riedl et al., 2001; Chai et al., 2001), while through its BIR3 domain inhibits the initiating caspase 9 (Srinivasula et al., 2001). XIAP is frequently overexpressed in tumors, in which it potentiates cell survival and resistance to chemotherapeutics, and thus it has become an important target for the development of cancer treatments aimed to antagonize the interaction of XIAP with caspases (Schimmer et al., 2006; Nakagawa et al., 2006; Mizutani et al., 2007; Lopes et al., 2007; Mannhold et al., 2010; Fulda and Vucic, 2012; Baggio et al., 2018).

Moreover, literature reports the involvement of XIAP in several fundamental cellular processes. Through its BIR1 domain, XIAP is involved in the NF- κ B pathway (Lu et al., 2007). Furthermore, it has been demonstrated that the RING

domain has an E3 ubiquitin ligase activity (Nakatani et al., 2013); this activity is responsible for the ubiquitination of important substrates such as RIP1 and RIP2, involved respectively in the pro-inflammatory TNF and NOD2 signalling pathways (Witt and Vucic, 2017; Goncharov et al., 2018). As a result, mutations in the XIAP gene have been related to inflammatory diseases such the X-linked lymphoproliferative syndrome type-2 (XLP2) (Damgaard et al., 2013) and the inflammatory bowel disease (IBD) (Pedersen et al., 2014). Finally, literature reports that XIAP also takes part in the maintenance of the intracellular copper homeostasis and that its downregulation may contribute to the onset of copper toxicosis such as Wilson's disease (Mufti et al., 2006; Galbán and Duckett, 2010). This multi-functional role of XIAP raised several questions about how this protein is able to perform so many activities, and which are the structural features that allows to XIAP to engage so many different interactions. From the structural point of view, all the single domains of XIAP have been characterized (Sun et al., 1999; Liu et al., 2000; Lu et al., 2007; Hui et al., 2010; Lukacs et al., 2013; Nakatani et al., 2013), and it is known that the BIR1 and the RING domains forms homodimers (Lu et al., 2007; Nakatani et al., 2013; Hou et al., 2017), but there is no information about their spatial arrangement, as the conformation of the full length XIAP has never been determined. Consequently, a structural characterization of the full length protein is essential in order to elucidate the relation between its structural features and the numerous cellular processes and interactions in which this protein is involved. In this study we used an integrative approach, combining Nuclear Magnetic Resonance (NMR), with Small-Angle X-ray Scattering (SAXS) and Electron Paramagnetic Resonance (EPR), in order to provide the first low-resolution structural characterization of the full length XIAP.

Materials & Methods

Protein expression and purification:

The gene encoding XIAP was cloned in the pENTR vector for the Gateway cloning technology and subcloned in the pDEST-HisMBP vector (which adds a His tag followed by the Maltose Binding Protein at the N-terminus of the protein), utilizing the pENTR/TEV/D-TOPO cloning kit (Invitrogen). *E. coli* BL21 (DE3) Codon Plus RIPL cells were transformed with the plasmid pDEST-HisMBP-XIAP, grown in LB medium (or in ¹⁵N M9 medium) supplemented with 100 µM ZnSO₄ at 37 °C and 170 rpm. At mid-log phase the cells were induced with 0.75 mM IPTG, and then grown overnight at 18 °C and 170 rpm. The cells were harvested and re-suspended in 100 mL of binding buffer (Tris 20 mM, TCEP 1 mM, Imidazole 5 mM, pH 8) supplemented with protease inhibitor tablets (Roche) and lysed by sonication (10'' ON, 50'' OFF, at 60% of amplitude for 40'). The lysate was passed through a 5 mL HisTrap FF affinity

column (GE healthcare Life Sciences) and washed with the elution buffer (Tris 20 mM, TCEP 1 mM, Imidazole 500 mM, pH 8). The His-MBP tag was cleaved incubating overnight with TEV in dialysis (5 L). As final purification step, a gel filtration using a HiLoad 16/600 Superdex 200 pg column (GE Healthcare Life Sciences) was performed in order to separate XIAP from the His-MBP tag and to transfer the protein in the final buffer (Tris 20 mM, TCEP 0.5 mM, pH 7.4). The eluted fractions were checked by SDS-PAGE, and those containing pure XIAP were collected and concentrated with an Amicon Ultra centrifugal filter device (MWCO = 50 kDa).

NMR:

NMR spectra were acquired at 310 K on a 700 MHz Bruker Avance Neo spectrometer equipped with a TCI CryoProbe. 2D ^1H - ^{15}N HSQC on a sample of ^{15}N -XIAP (160 μM monomer concentration) in Tris 20 mM buffer, 0.5 mM TCEP, pH 7.4. The spectra were processed with Bruker TopSpin.

SEC-MALS:

Size Exclusion Chromatography with Multi-Angle Light Scattering (SEC-MALS) was performed on full length XIAP (30 μM), utilizing a Superdex 200 10/300 GL column (GE healthcare Life Sciences) at a flowrate of 0.3 mL/min, by an instrumentation including a multi-angle light scattering, with a quasi-elastic light scattering detector, and a refractometer with extended range (Wyatt Technology), connected to a high-performance liquid chromatographer (HPLC).

CD:

Circular Dichroism experiments were performed on 2.2 μM samples of the full length XIAP by a JASCO J-810 spectrometer and the spectra were analysed with the DichroWeb software.

ICP-AES:

The Zinc/protein ratio of the full length XIAP (5 μM) was determined by Inductively Coupled Plasma Atomic Emission Spectrometry (ICP-AES) measurements, carried out by a Varian 720 ES simultaneous ICP-AES equipped with a CETAC U5000 AT+ ultrasonic nebulizer.

SAXS:

Synchrotron radiation X-ray scattering from full length XIAP in solution was collected at the EMBL P12 beamline of the storage ring PETRA III (DESY, Hamburg, Germany, (Blanchet et al., 2015)). Images were recorded using a photon counting Pilatus-2M detector at a sample to detector distance of 3.1 m and a wavelength (λ) of 1.2 \AA covering the range of momentum transfer (s) $0.01 < s < 0.5 \text{\AA}^{-1}$; with $s=4\pi\sin\theta/\lambda$. To obtain data from a monodisperse sample, SEC-SAXS mode was employed (size exclusion chromatography directly coupled to

the scattering experiment). Here, the eluent from a Superdex 200 10/300 GL (GE healthcare Life Sciences) column is passed through an UV-cell (280 nm, Agilent) and then to the SAXS capillary where 1^s sample exposures are recorded. As mobile phase SEC buffer (Tris 20 mM, TCEP 0.5 mM, pH 7.4.) was used. 100 μ L of purified sample (7.5 mg/mL) were injected and the flow rate was 0.5 mL/min. SAXS data were recorded from macromolecular free fractions corresponding to the matched solvent blank (frames 1,389–1,804 s) which eluted directly after the peak corresponding to the separated XIAP dimers (elution time maximum = 20.7 min, 10.4 mL; frames 1,244–1,281 s). Data reduction to produce the final scattering profile of dimeric full length XIAP was performed using standard methods. Briefly, 2D-to-1D radial averaging was performed using the *SASFLOW* pipeline (Franke et al., 2017). CHROMIXS was used for the visualization and reduction of the SEC-SAXS datasets (REF). Aided by the integrated prediction algorithms in Chormix the optimal frames within the elution peak and the buffer regions were selected. Then, single buffer frames were subtracted from sample frames one by one, scaled and averaged to produce the final subtracted curve.

The indirect inverse Fourier transform of the SAXS data and the corresponding probable real space-scattering pair distance distribution ($p(r)$ versus r profile) of full length XIAP was calculated using GNOM (Svergun, 1992), from which the R_g and D_{max} were determined. The $p(r)$ versus r profile was also used for volume and subsequent molecular weight estimates of the XIAP dimers, as evaluated by the *datporod* (Porod volume) (Petoukhov et al., 2012), *datmow* (Fischer et al., 2010), and *datvc* (Rambo and Tainer, 2013) modules of the ATSAS 2.8 package. The *ab initio* bead modeling of XIAP was performed using DAMMIF (Franke and Svergun, 2009). Because SAXS data can be ambiguous with respect to shape restoration DAMMIF was run 10 times, and the consistency of the individual models was evaluated using the normalized spatial discrepancy (NSD) metric (where NSD <0.9 represents spatially similar) (Volkov and Svergun, 2003). From this the most probable model was selected for further analysis. *Ab initio* modelling was performed with and without adding symmetry constraints (p2 symmetry to reflect the dimeric state of the protein). The resolution estimate of the model ensemble was estimated with SASRES (Tuukkanen et al., 2016). The *a priori* shape classification of the SAXS data was determined with DATCLASS (Franke et al., 2018).

The molecule masses (MM) was evaluated based on concentration independent methods as described in (Hajizadeh et al., 2018). Further analysis of the flexibility of the samples was addressed with Ensemble Optimization Method (EOM). For this, ensembles of models with variable conformations are selected from a pool of randomly generated models such that the scattering from the ensemble fits the experimental data, and the distributions of the overall

parameters (e.g. D_{\max}) in the selected pool are compared to the original pool (Tria et al., 2015).

The SAXS data (as summarized in Table X) and *ab initio* bead models as well as rigid body reconstruction of full length XIAP have been deposited into the Small-Angle Scattering Biological Data Bank (SASBDB) (Valentini et al., 2015) under the accession code (to be determined).

EPR:

In order to perform EPR and EPR-DEER experiments the MTSL (S-(1-oxyl-2,2,5,5-tetramethyl-2,5-dihydro-1H-pyrrol-3-yl)methyl methanesulfonothioate) nitroxide spin label was selected for Site-Directed Spin Labeling (SDSL) (Hubbell et al., 2013; Klare, 2013). WT XIAP possesses four cysteine residues (C12, C202, C213 and C351) that are not involved in zinc coordination. Given the homodimeric nature of XIAP, labeling the same cysteine residue on each monomer would provide a symmetrical distance restraint. Mutations were sequentially introduced on the WT XIAP gene using the Quick Change II mutagenesis kit (Invitrogen), and the resulting genes were checked by DNA sequencing. Two triple mutants of XIAP were chosen for the SDSL reaction, termed XIAP C202 (i.e. XIAP C12A, C213G, C351S) and XIAP C351 (i.e. C12A, C202S, C213G).

SDSL reaction was performed by incubating XIAP mutants with a 10-fold excess of MTSL. The reaction was kept for 2 hours at room temperature under continuous agitation, after which an identical amount of MTSL was added to the solution to improve the labelling yield. After 4 hours, the unreacted spin label was eliminated by washing several times the reaction solution with Tris 20 mM, pH 7.4 buffer using an Amicon Ultra centrifugal filter device (MCWO = 50 kDa). The resulting samples were checked by X-band EPR to ensure the complete MTSL removal and to calculate the relative spin concentrations from double integration of the signals. Using a calibration curve, the total spin concentrations resulted equal to 30 μ M and 60 μ M for the two XIAP mutants labeled with MTSL nitroxide on C202 (XIAP C202R1) and C351 (XIAP C351R1), respectively. X-band (9.8 GHz) continuous wave EPR experiments were performed at room temperature on a Bruker ELEXSYS E580 spectrometer. The parameters used were the following: microwaves power = 10 mW, magnetic field modulation amplitude = 0.1 mT, field sweep = 10 mT, receiver gain = 60 dB. The spectra were accumulated 9 times to increase the S/N ratio. Simulations were performed with SimLabel program (GUI of EasySpin software) (Etienne et al., 2017), to obtain the components of the experimental spectra and the relative parameters (g-tensor, A splitting constants and τ C correlational times).

Q-band experiments were performed using the standard EN5107D2 resonator and an Oxford helium system to keep temperature at 50K. 4-pulse DEER

experiments (34 GHz) were recorded with a Hahn-echo pulse sequence $\pi/2 - \tau - \pi - \tau - \text{echo}$ with 20 ns ($\pi/2$) and 40 ns (π), $\tau_1 = 200$ ns and τ_2 was set accordingly to relative spin-spin relaxation time. The pump ELDOR pulse was centred at the central resonance and the observed frequency was set with an offset of 56 MHz. The total acquisition time was 20-24 hours to increase the S/N ratio. All DEER measurements were performed with 8-steps nuclear modulation average.

DEERANALYSIS2013 software was used to correct background echo decay involving a second order polynomial baseline correction, and successively to obtain the relative distance distribution (Jeschke, 2002, 2012).

Results

The integrated approach used in this study allowed the collection of several information for the structural characterization of the full length XIAP. SEC-MALS experiments indicated that the protein in solution is monodisperse and forms a homodimer of approximately 115 kDa (Fig. 1). Each monomer of full length XIAP contains five zinc fingers: one in each BIR domain, and two in the C-terminal RING domain (Sun et al., 1999; Liu et al., 2000; Nakatani et al., 2013; Hou et al., 2017). The metallation state of the samples used in this study as determined by ICP-AES resulted in 10 zinc ions per XIAP homodimer, indicating that all zinc binding sites are occupied. In principle, the multidomain nature of XIAP could allow a certain degree of relative flexibility of the single domains. Therefore, heteronuclear NMR spectroscopy was employed to qualitatively assess the dynamic nature of the XIAP homodimer. Only a small number of amide crosspeaks (~70) were visible in the central region of the ^1H - ^{15}N HSQC spectrum of XIAP (Fig. 2). These signals likely arise from the unstructured regions of the protein, i.e. the N-terminus and the linkers between the domains. No signals typical of a folded protein were detected, indicating that the conformation of XIAP is sufficiently rigid to cause broadening beyond detection of the signals arising from the structured regions, due to the slow rotation of the dimer in solution. NMR experiments optimized for high molecular weight systems did not provide additional information due to the low sample concentration imposed by the aggregation propensity of XIAP (data not shown). Further evidence of a rigid conformation assumed by the structured domains of XIAP was derived from the EPR experiments. For this purpose, full length XIAP was labelled with MTSL either at cysteine 202 on the BIR2 domain (XIAP C202R1) or at cysteine 351 on the BIR3 domain (XIAP C351R1). The X-band CW-EPR spectrum of XIAP C202R1 at room temperature exhibits a line-shape typical of the presence of a multi motional components (Fig. 3A, black line). In fact, the simulation revealed the presence of a sharp component ($\tau_c = 0.1$ ns) (Fig. 3A, blue line), relative to a very flexible

conformation, and a broader signal ($\tau_c = 2.5$ ns) (Fig. 3A, pink line), specific of a more rigid structure. The broad component is the most abundant (92%), indicating that XIAP has a rigid structure surrounding cysteine 202. Similar results were obtained for XIAP C351R1: The CW-EPR spectrum (Fig. 3B, black line) shows the presence of two minor sharp components characteristic of very flexible conformations, with spin label tumbling times of 0.1 ns and 0.5 ns (Fig. 3B, pink and green lines respectively), while most of the EPR signal (84%) arises from a broader component ($\tau_c = 3.3$ ns) (Fig. 3B, pink line), revealing that also in proximity of cysteine 351 the protein assumes a rigid structure. Overall, these findings suggest that the XIAP homodimer in solution adopts a relatively compact conformation.

To confirm this, SAXS was performed to obtain the primary structural parameters and overall shape characteristics of dimeric XIAP in solution. In-line SEC-SAXS was employed, based on the results from SEC-MALS, indicating the presence of trace amounts of higher molecular weight species. The latter are removed during the chromatography step so that the scattering intensity data is measured solely from the separated dimeric form. The radius of gyration (R_g) through the dimer elution peak is consistent (36–38 Å), suggesting that indeed the solute is monodisperse. The final averaged SAXS profile of dimeric full length XIAP is shown in Figure 4A, and the Guinier plot of the SAXS data is linear (Fig. 4B), as expected for aggregate-free, monodisperse systems, yielding an R_g of 37 ± 0.6 Å. Compared to expected molecule mass of 115 kDa, this suggests that XIAP has a relatively globular isotropic mass distribution. The corresponding $p(r)$ versus r profile (Fig. 4C) supports this observation as the distribution of vector lengths is almost Gaussian with a maximum particle dimension (D_{max}) of ~ 122 Å. The *a priori* shape classification of the SAXS data places XIAP in the “flat/compact” regime. The final structural parameters extracted from the data, including volume and molecular mass estimates, are consistent with dimeric XIAP and the SEC-MALS results (Table 1). In addition, the *ab initio* low resolution structure indicated that the quaternary structure of the XIAP homodimer is compatible with a discoidal and flat conformation (Fig. 4D). Here, the most probable model determined with a P2 symmetry is shown. The overall projected ensemble resolution was determined to be 40 ± 3 Å.

Quantitative flexibility analysis was performed using the EOM which fits the experimental data using scattering computed from conformational ensembles (Fig. 4A). Over 14000 models with randomized linkers were generated based on the atomic structures from the individual domains: BIR1 (2POI.pdb), BIR2 (4J3Y.pdb), BIR3 (4KMP.pdb), UBA (2KNA.pdb) and RING (4IC2.pdb). The missing linker residues (117 in total) as well as 21 N-terminal residues make up for $\sim 23\%$ of the overall sequence. To account for the dimerization, P2 symmetry was partially applied by constraining the BIR1 as well as the RING dimer

interface as seen in the crystal structure (2POI.pdb and 4IC2.pdb). The narrow distributions of the overall parameters in the selected structures compared with those the original pool (Fig. 5A&B) suggest that XIAP is compact and that the orientation of the individual domains is rather rigid and not as flexible as one would expect. Figure 5C, shows representative models from the selected pools. In general, these comprise a similar volume as the generated *ab initio* models (overlaid as grey surface representation).

The reduce degree in flexibility suggests that rigid body modelling will result in realistic structures. We, therefore, sought to obtain a low-resolution structural model of the XIAP homodimer by combining EPR-derived distance restraints with SAXS data. For this, Q-band DEER measurements on XIAP C202R1 and XIAP C351R1 were performed. Since the protein is a homodimer, the values calculated from the DEER experiments correspond to the distances between two spin-labeled cysteines 202 (or 351) located one on each monomer. For XIAP C202R1 the distance distribution calculated has a single maximum at $38 \pm 6 \text{ \AA}$ (Fig. 6), while for XIAP C351R1 oscillation of the echo-detected signal was not observed (Fig. 7), indicating that the two cysteines 351 of each monomer are located farther than the estimated upper limit of the DEER experiment in our experimental conditions ($> 80 \text{ \AA}$). These volume fractions are indeed reflected in a large volume fraction of the EOM determined models (model 5 and 6 comprising roughly 50% volume fraction, table 2). Further we performed modelling approaches with CORAL. In this rigid body modelling approach possible models are generated by adding dummy residues to mimic the missing N-terminal and linker residues (Fig. 8). Attempts with and without adding the restrain of 40 \AA between cysteine 202 of the BIR1 domain resulted in a number of different structural rearrangements of the folded domains. Here we conclude, that even though the flexibility of full length XIAP is restricted, the data cannot be described with one unique model.

Conclusions

Given the number of different pathways in which XIAP is involved, it becomes necessary to know whether its three-dimensional structure can affect or modulate them in any way. This is especially critical when considering that several of XIAP domains are being heavily studied as potential anticancer drug targets (Fulda and Vucic, 2012). As is normally the case with many multidomain proteins, only the structures of the single domains have been relied upon for drug screening and for investigating protein-protein interactions, and the overall protein conformation has never been properly accounted for. Here, by integrating complementary data from different structural and biophysical techniques, we provided a first low-resolution model of full length XIAP, and we assessed the degree of flexibility of the protein.

XIAP behaved homogeneously in solution, and was mainly present as a heterodimer, with negligible amounts of higher molecular weight species. Most strikingly, despite the fact that unstructured N-terminus and the inter-domain linkers comprise more than 20% of the overall sequence, our data indicate that the XIAP homodimer is a rigid entity. This is clearly observed by both *ab initio* modeling and ensemble fitting based on the SAXS data, and is corroborated by the fact that the folded domains cannot be detected by solution NMR on non-deuterated samples. Furthermore, only ~70 NMR signals from unfolded regions were detected, i.e. about one half of the total expected unfolded residues, suggesting that some of the inter-domain linkers could actually fold as part of the overall 3D structure. Rigid body modeling combining SAXS and EPR-DEER distance restraints revealed a challenging task, due to the data being too sparse compared to the number of degrees of freedom of the XIAP dimer. Despite this, our findings highlight the fact that XIAP assumes quite a compact and rigid conformation, and should not be treated with simplistic “beads on a string” models when studying the interactions with its many partners. Based on this evidence, further refinement of the XIAP dimer structure should be made possible by including in the calculations electron density maps obtained by single-particle cryo-electron microscopy, which – in the case of a more rigid structure – could even allow single-particle reconstruction at a higher resolution.

References

Baggio, C., Gambini, L., Udompholkul, P., Salem, A.F., Aronson, A., Dona, A., Troadec, E., Pichiorri, F., and Pellicchia, M. (2018). Design of Potent pan-IAP and Lys-Covalent XIAP Selective Inhibitors Using a Thermodynamics Driven Approach. *J. Med. Chem.*

Blanchet, C.E., Spilotros, A., Schwemmer, F., Graewert, M.A., Kikhney, A., Jeffries, C.M., Franke, D., Mark, D., Zengerle, R., Cipriani, F., et al. (2015). Versatile sample environments and automation for biological solution X-ray scattering experiments at the P12 beamline (PETRA III, DESY). *J. Appl. Crystallogr.* *48*, 431–443.

Chai, J., Shiozaki, E., Srinivasula, S.M., Wu, Q., Datta, P., Alnemri, E.S., Shi, Y., and Dataa, P. (2001). Structural basis of caspase-7 inhibition by XIAP. *Cell* *104*, 769–780.

Damgaard, R.B., Fiil, B.K., Speckmann, C., Yabal, M., Stadt, U. zur Bekker-Jensen, S., Jost, P.J., Ehl, S., Mailand, N., and Gyrd-Hansen, M. (2013). Disease-causing mutations in the XIAP BIR2 domain impair NOD2-dependent immune signalling. *EMBO Mol. Med.* *5*, 1278–1295.

Deveraux, Q.L., Takahashi, R., Salvesen, G.S., and Reed, J.C. (1997). X-linked IAP is a direct inhibitor of cell-death proteases. *Nature* *388*, 300–304.

Etienne, E., Le Breton, N., Martinho, M., Mileo, E., and Belle, V. (2017). SimLabel: a graphical user interface to simulate continuous wave EPR spectra from site-directed spin labeling experiments. *Magn. Reson. Chem. MRC* *55*, 714–719.

Fischer, H., Neto, O., De, M., Napolitano, H.B., Polikarpov, I., and Craievich, A.F. (2010). Determination of the molecular weight of proteins in solution from a single small-angle X-ray scattering measurement on a relative scale. *J. Appl. Crystallogr.* *43*, 101–109.

Franke, D., and Svergun, D.I. (2009). DAMMIF, a program for rapid ab-initio shape determination in small-angle scattering. *J. Appl. Crystallogr.* *42*, 342–346.

Franke, D., Petoukhov, M.V., Konarev, P.V., Panjkovich, A., Tuukkanen, A., Mertens, H.D.T., Kikhney, A.G., Hajizadeh, N.R., Franklin, J.M., Jeffries, C.M., et al. (2017). ATSAS 2.8: a comprehensive data analysis suite for small-angle scattering from macromolecular solutions. *J. Appl. Crystallogr.* *50*, 1212–1225.

Franke, D., Jeffries, C.M., and Svergun, D.I. (2018). Machine Learning Methods for X-Ray Scattering Data Analysis from Biomacromolecular Solutions. *Biophys. J.* *114*, 2485–2492.

Fulda, S., and Vucic, D. (2012). Targeting IAP proteins for therapeutic intervention in cancer. *Nat. Rev. Drug Discov.* *11*, 109–124.

Galbán, S., and Duckett, C.S. (2010). XIAP as a ubiquitin ligase in cellular signaling. *Cell Death Differ.* 17, 54–60.

Goncharov, T., Hedayati, S., Mulvihill, M.M., Izrael-Tomasevic, A., Zobel, K., Jeet, S., Fedorova, A.V., Eidenschenk, C., deVoss, J., Yu, K., et al. (2018). Disruption of XIAP-RIP2 Association Blocks NOD2-Mediated Inflammatory Signaling. *Mol. Cell* 69, 551-565.e7.

Hajizadeh, N.R., Franke, D., Jeffries, C.M., and Svergun, D.I. (2018). Consensus Bayesian assessment of protein molecular mass from solution X-ray scattering data. *Sci. Rep.* 8, 7204.

Hou, M.-M., Polykretis, P., Luchinat, E., Wang, X., Chen, S.-N., Zuo, H.-H., Yang, Y., Chen, J.-L., Ye, Y., Li, C., et al. (2017). Solution structure and interaction with copper in vitro and in living cells of the first BIR domain of XIAP. *Sci. Rep.* 7, 16630.

Hubbell, W.L., López, C.J., Altenbach, C., and Yang, Z. (2013). Technological advances in site-directed spin labeling of proteins. *Curr. Opin. Struct. Biol.* 23, 725–733.

Hui, S.-K., Tse, M.-K., Yang, Y., Wong, B.C.-Y., and Sze, K.-H. (2010). Backbone and side-chain ¹H, ¹³C and ¹⁵N assignments of the ubiquitin-associated domain of human X-linked inhibitor of apoptosis protein. *Biomol. NMR Assign.* 4, 13–15.

Jeschke, G. (2002). Distance Measurements in the Nanometer Range by Pulse EPR. *ChemPhysChem* 3, 927–932.

Jeschke, G. (2012). DEER Distance Measurements on Proteins. *Annu. Rev. Phys. Chem.* 63, 419–446.

Klare, J.P. (2013). Site-directed spin labeling EPR spectroscopy in protein research. *Biol. Chem.* 394, 1281–1300.

Liston, P., Roy, N., Tamai, K., Lefebvre, C., Baird, S., Cherton-Horvat, G., Farahani, R., McLean, M., Ikeda, J.E., MacKenzie, A., et al. (1996). Suppression of apoptosis in mammalian cells by NAIP and a related family of IAP genes. *Nature* 379, 349–353.

Liu, Z., Sun, C., Olejniczak, E.T., Meadows, R.P., Betz, S.F., Oost, T., Herrmann, J., Wu, J.C., and Fesik, S.W. (2000). Structural basis for binding of Smac/DIABLO to the XIAP BIR3 domain. *Nature* 408, 1004–1008.

Lopes, R.B., Gangeswaran, R., McNeish, I.A., Wang, Y., and Lemoine, N.R. (2007). Expression of the IAP protein family is dysregulated in pancreatic cancer cells and is important for resistance to chemotherapy. *Int. J. Cancer* 120, 2344–2352.

- Lu, M., Lin, S.-C., Huang, Y., Kang, Y.J., Rich, R., Lo, Y.-C., Myszka, D., Han, J., and Wu, H. (2007). XIAP induces NF-kappaB activation via the BIR1/TAB1 interaction and BIR1 dimerization. *Mol. Cell* 26, 689–702.
- Lukacs, C., Belunis, C., Crowther, R., Danho, W., Gao, L., Goggin, B., Janson, C.A., Li, S., Remiszewski, S., Schutt, A., et al. (2013). The structure of XIAP BIR2: understanding the selectivity of the BIR domains. *Acta Crystallogr. D Biol. Crystallogr.* 69, 1717–1725.
- Mannhold, R., Fulda, S., and Carosati, E. (2010). IAP antagonists: promising candidates for cancer therapy. *Drug Discov. Today* 15, 210–219.
- Mizutani, Y., Nakanishi, H., Li, Y.N., Matsubara, H., Yamamoto, K., Sato, N., Shiraishi, T., Nakamura, T., Mikami, K., Okihara, K., et al. (2007). Overexpression of XIAP expression in renal cell carcinoma predicts a worse prognosis. *Int. J. Oncol.* 30, 919–925.
- Mufti, A.R., Burstein, E., Csomos, R.A., Graf, P.C.F., Wilkinson, J.C., Dick, R.D., Challa, M., Son, J.-K., Bratton, S.B., Su, G.L., et al. (2006). XIAP Is a Copper Binding Protein Deregulated in Wilson's Disease and Other Copper Toxicosis Disorders. *Mol. Cell* 21, 775–785.
- Nakagawa, Y., Abe, S., Kurata, M., Hasegawa, M., Yamamoto, K., Inoue, M., Takemura, T., Suzuki, K., and Kitagawa, M. (2006). IAP family protein expression correlates with poor outcome of multiple myeloma patients in association with chemotherapy-induced overexpression of multidrug resistance genes. *Am. J. Hematol.* 81, 824–831.
- Nakatani, Y., Kleffmann, T., Linke, K., Condon, S.M., Hinds, M.G., and Day, C.L. (2013). Regulation of ubiquitin transfer by XIAP, a dimeric RING E3 ligase. *Biochem. J.* 450, 629–638.
- Pedersen, J., LaCasse, E.C., Seidelin, J.B., Coskun, M., and Nielsen, O.H. (2014). Inhibitors of apoptosis (IAPs) regulate intestinal immunity and inflammatory bowel disease (IBD) inflammation. *Trends Mol. Med.* 20, 652–665.
- Petoukhov, M.V., Franke, D., Shkumatov, A.V., Tria, G., Kikhney, A.G., Gajda, M., Gorba, C., Mertens, H.D.T., Konarev, P.V., and Svergun, D.I. (2012). New developments in the ATSAS program package for small-angle scattering data analysis. *J. Appl. Crystallogr.* 45, 342–350.
- Rambo, R.P., and Tainer, J.A. (2013). Accurate assessment of mass, models and resolution by small-angle scattering. *Nature* 496, 477–481.
- Riedl, S.J., Renatus, M., Schwarzenbacher, R., Zhou, Q., Sun, C., Fesik, S.W., Liddington, R.C., and Salvesen, G.S. (2001). Structural basis for the inhibition of caspase-3 by XIAP. *Cell* 104, 791–800.
- Schimmer, A.D., Dalili, S., Batey, R.A., and Riedl, S.J. (2006). Targeting XIAP for the treatment of malignancy. *Cell Death Differ.* 13, 179–188.

Srinivasula, S.M., Hegde, R., Saleh, A., Datta, P., Shiozaki, E., Chai, J., Lee, R.A., Robbins, P.D., Fernandes-Alnemri, T., Shi, Y., et al. (2001). A conserved XIAP-interaction motif in caspase-9 and Smac/DIABLO regulates caspase activity and apoptosis. *Nature* 410, 112–116.

Sun, C., Cai, M., Gunasekera, A.H., Meadows, R.P., Wang, H., Chen, J., Zhang, H., Wu, W., Xu, N., Ng, S.-C., et al. (1999). NMR structure and mutagenesis of the inhibitor-of-apoptosis protein XIAP. *Nature* 401, 818–822.

Svergun, D.I. (1992). Determination of the regularization parameter in indirect-transform methods using perceptual criteria. *J. Appl. Crystallogr.* 25, 495–503.

Tria, G., Mertens, H.D.T., Kachala, M., and Svergun, D.I. (2015). Advanced ensemble modelling of flexible macromolecules using X-ray solution scattering. *IUCrJ* 2, 207–217.

Tuukkanen, A.T., Kleywegt, G.J., and Svergun, D.I. (2016). Resolution of *ab initio* shapes determined from small-angle scattering. *IUCrJ* 3, 440–447.

Valentini, E., Kikhney, A.G., Previtali, G., Jeffries, C.M., and Svergun, D.I. (2015). SASBDB, a repository for biological small-angle scattering data. *Nucleic Acids Res.* 43, D357–363.

Volkov, V.V., and Svergun, D.I. (2003). Uniqueness of *ab initio* shape determination in small-angle scattering. *J. Appl. Crystallogr.* 36, 860–864.

Witt, A., and Vucic, D. (2017). Diverse ubiquitin linkages regulate RIP kinases-mediated inflammatory and cell death signaling. *Cell Death Differ.* 24, 1160–1171.

Figures:

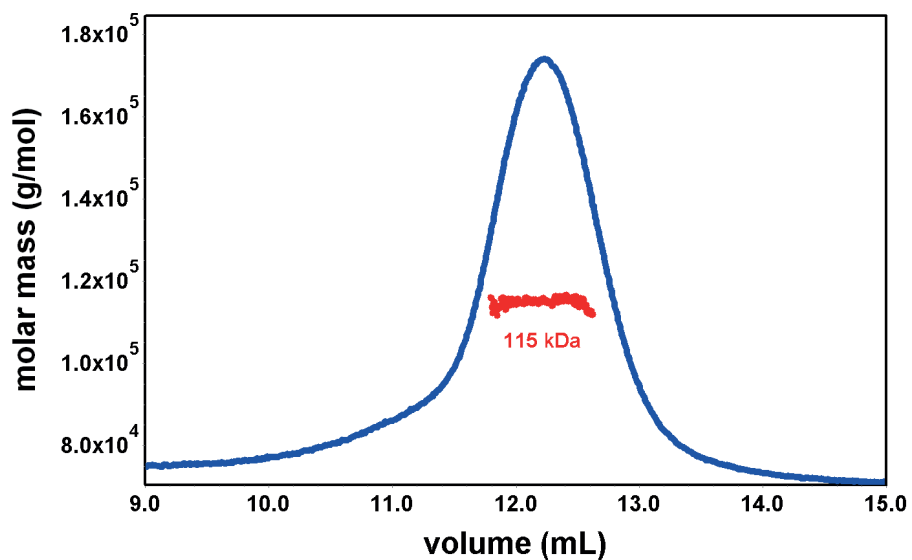


Fig. 1: SEC-MALS performed on full length XIAP (30 μ M).

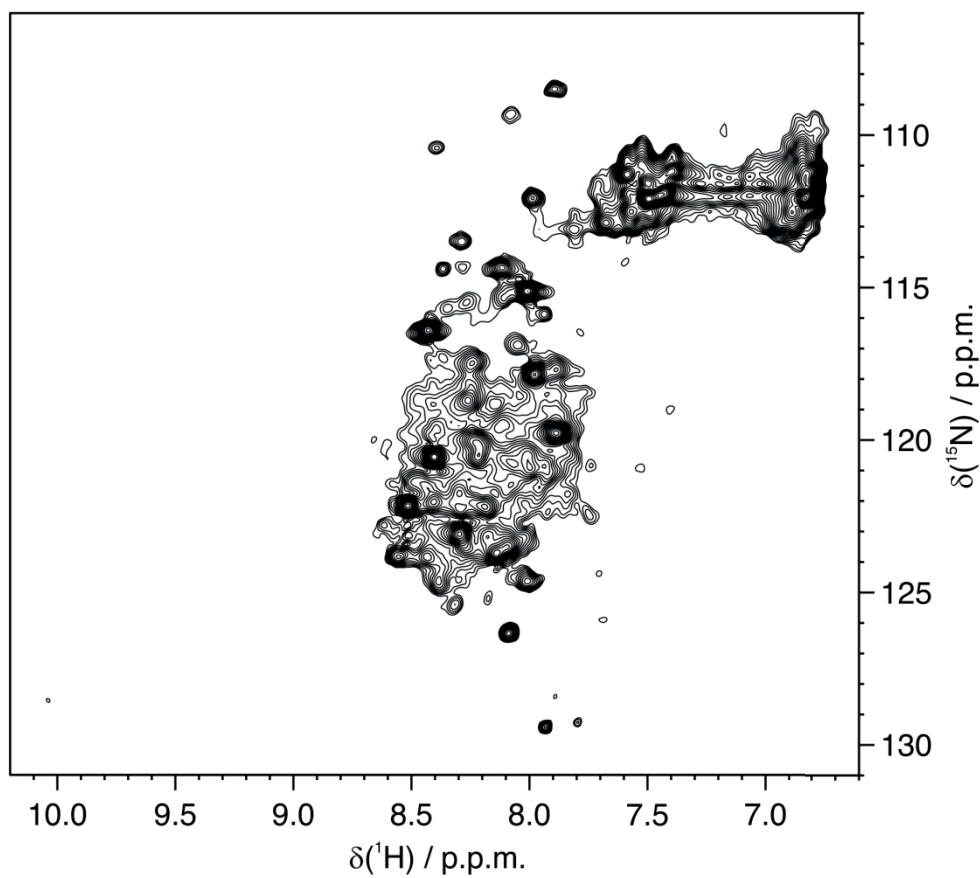


Fig. 2: ^1H - ^{15}N HSQC (700 MHz, 310 K) spectrum acquired on full length of XIAP (160 μ M monomer concentration).

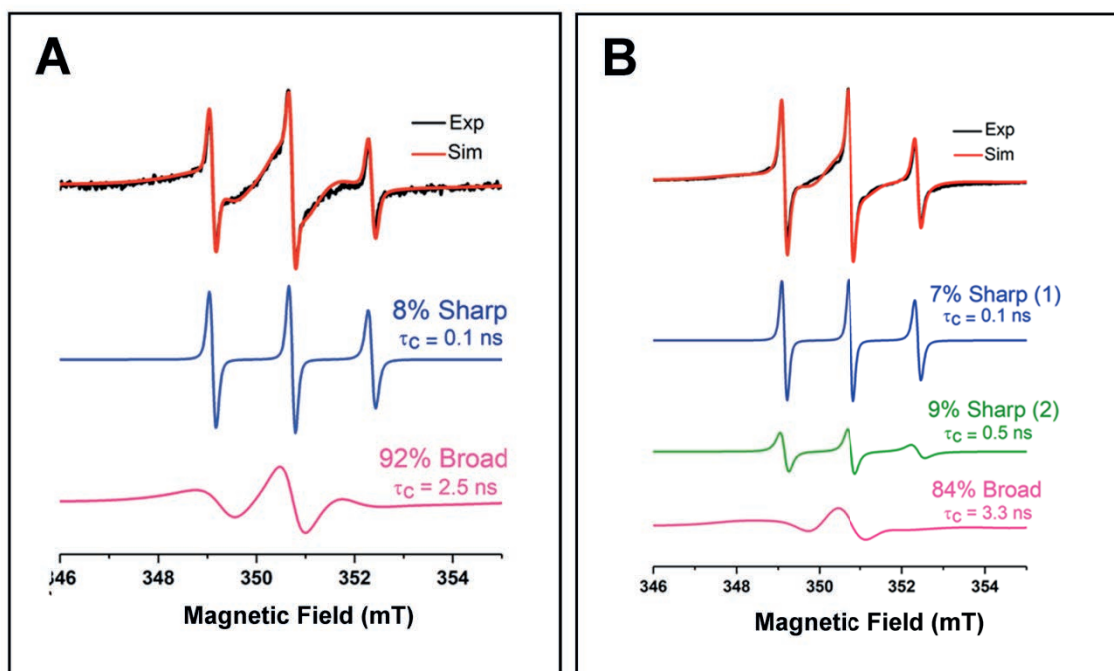


Fig. 3: X-band CW-EPR spectra at room temperature and relative simulations respectively of XIAP C202R1 (A) and XIAP C351 (B).

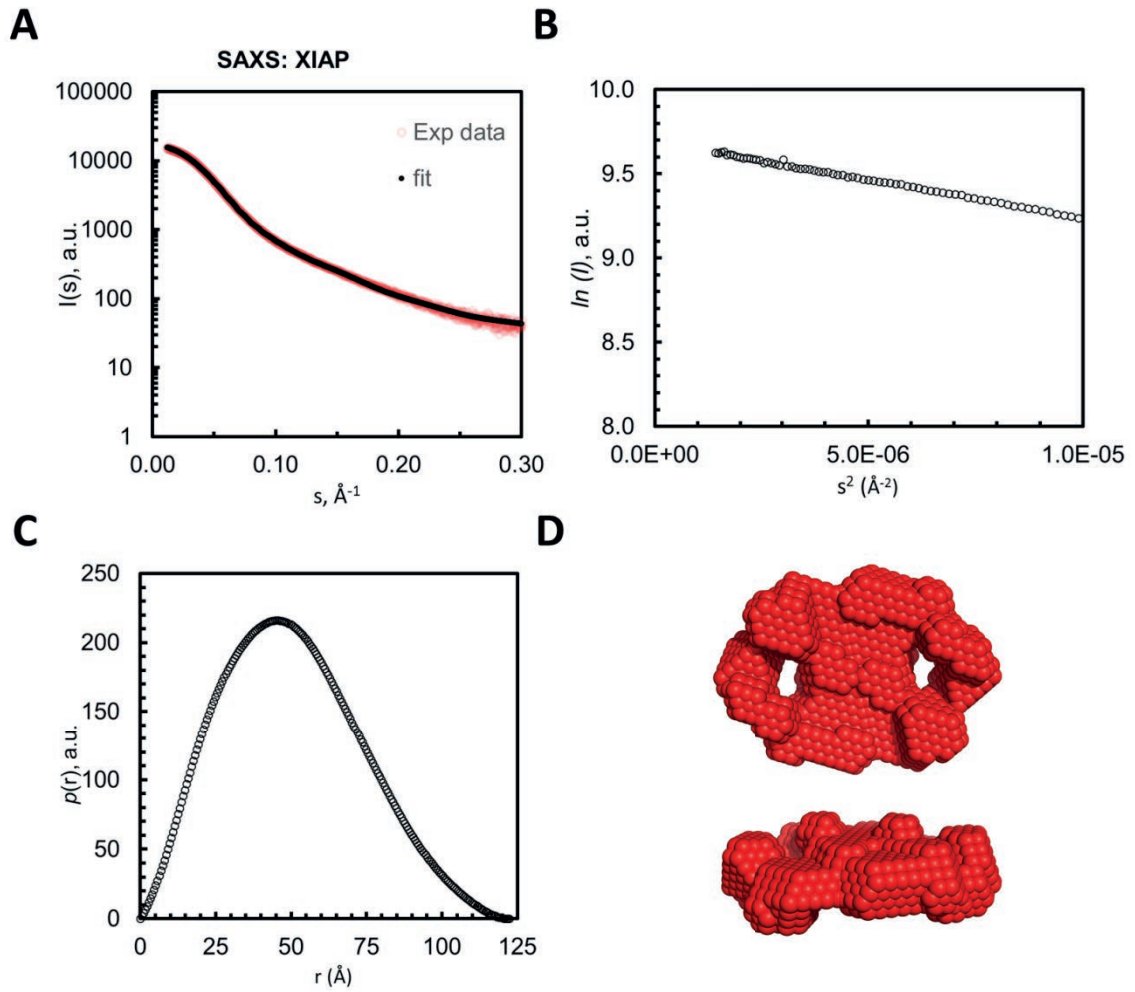


Fig. 4: SAXS data, primary structural parameters and overall shape characteristics. **A)** Averaged SEC-SAXS profile of XIAP through the dimeric elution peak (black) and corresponding fit against the data from the EOM approach (see Fig. 5, $\lambda^2=3.9$ with no systematic deviation). **B)** Guinier plot of $\ln I(s)$ versus s^2 . **C)** $p(r)$ versus r profile of XIAP. **D)** *ab initio* bead model reconstruction, *top and side view*; *a.u.*, arbitrary units.

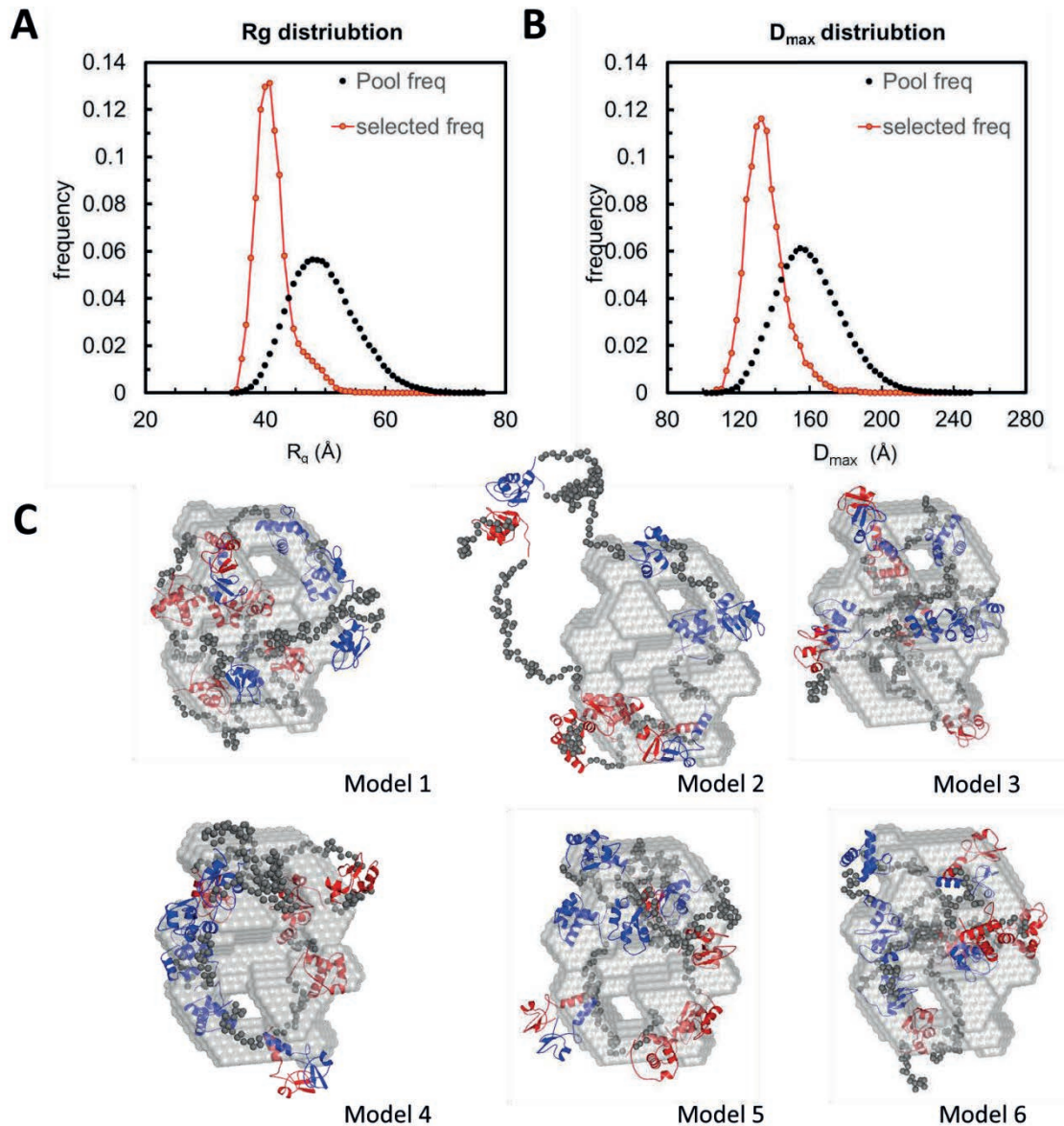


Fig. 5: Flexibility assessment. **A&B)** Distribution for structural parameters (**A**, R_g; **B**, D_{max}) of selected models (red) compared to those of initial random pool (black). **C)** representative conformations are shown as cartoons (folded domains) and spheres represent linkers and N-terminal residues. For orientation, the models are overlaid with the *ab initio* model (shown as grey surface). The monomeric subunits are in red and blue.

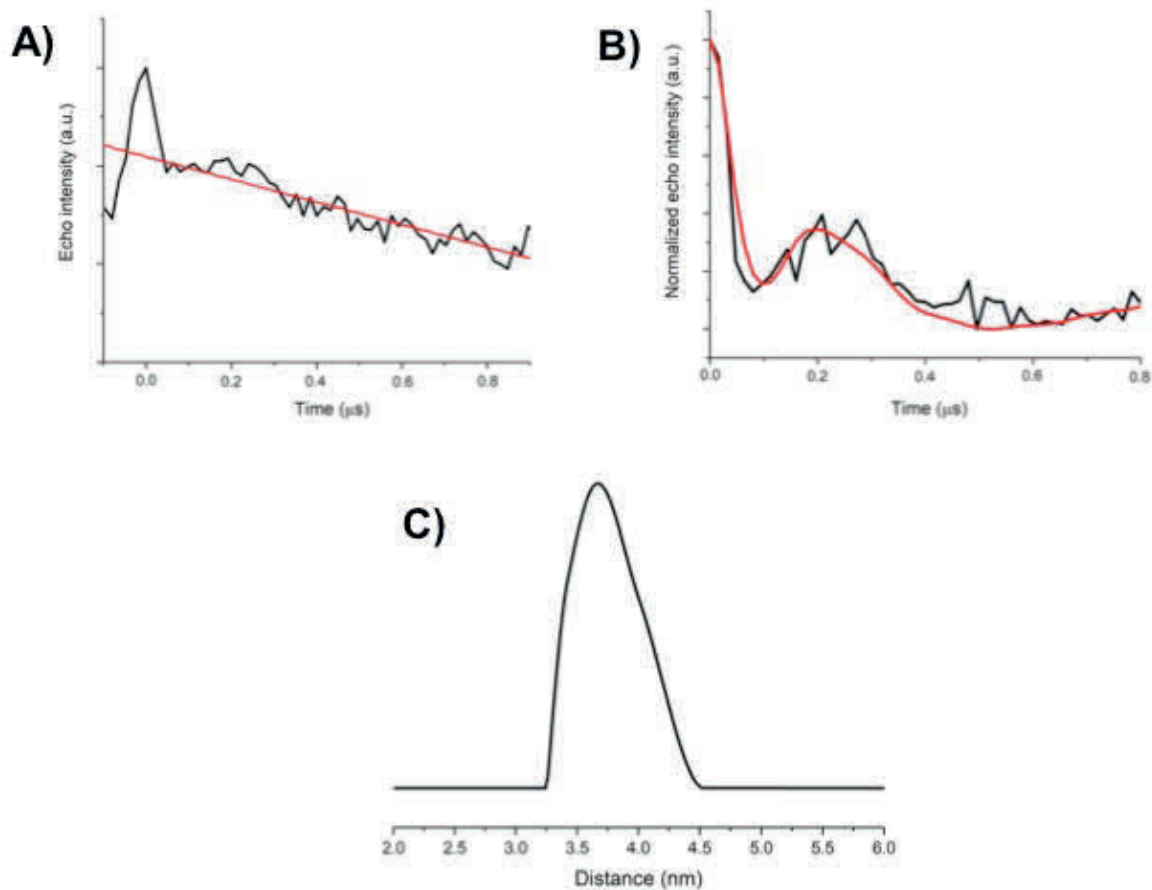


Fig. 6: Q-band DEER trace (A), relative background correction (B) and calculated distance distribution (C) for XIAP C202R1.

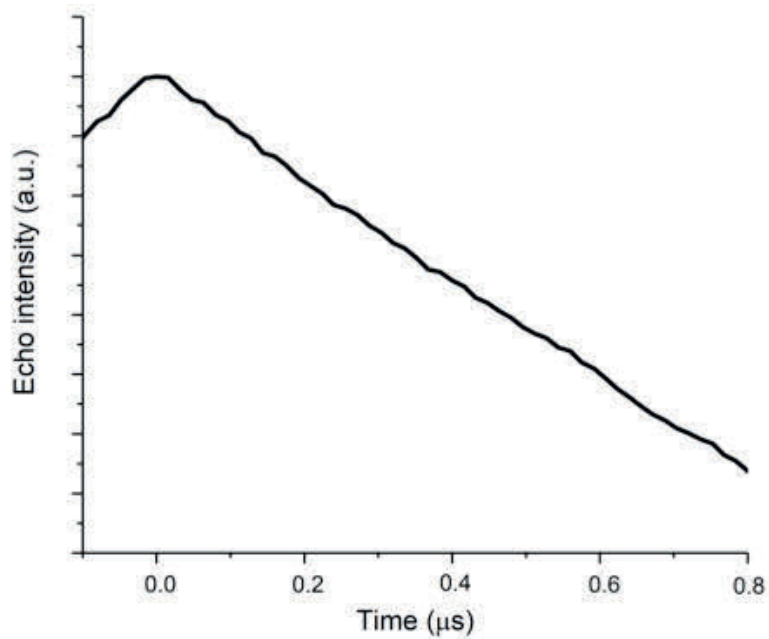


Fig. 7: Q-band DEER trace without echo oscillation obtained for XIAP C351R1.

R_g (Guinier)	R_g (p(r) versus r)	D_{max}	$V_{P'}$ Porod volume	$V_{P'}$ DAM volume	MM^a (Porod volume)	MM (datmow)	MM (Vc)	MM (DAM) ^b
nm	Å	Å	nm ³	nm ³	kDa	kDa	kDa	kDa
3.64 ± 0.02	37 ± 0.6	122.2	194	178	121	116	115	89 kD

Table 1: Structural parameters for XIAP.

Models	R_g	D_{max}	Fraction	Distance 202	Distance 351
Model 1	38.53	131.47	27.2	54	53
Model 2	41.86	137.05	9.1	84	91
Model 3	42.44	141.33	9.1	63	72
Model 4	41.65	127.24	9.1	72	55
Model 5	41.07	132.47	36.4	42	82
Model 6	44.58	140.84	9.1	43	83
	40.95	133.7			

Table 2: Structural parameters of selected EOM models.

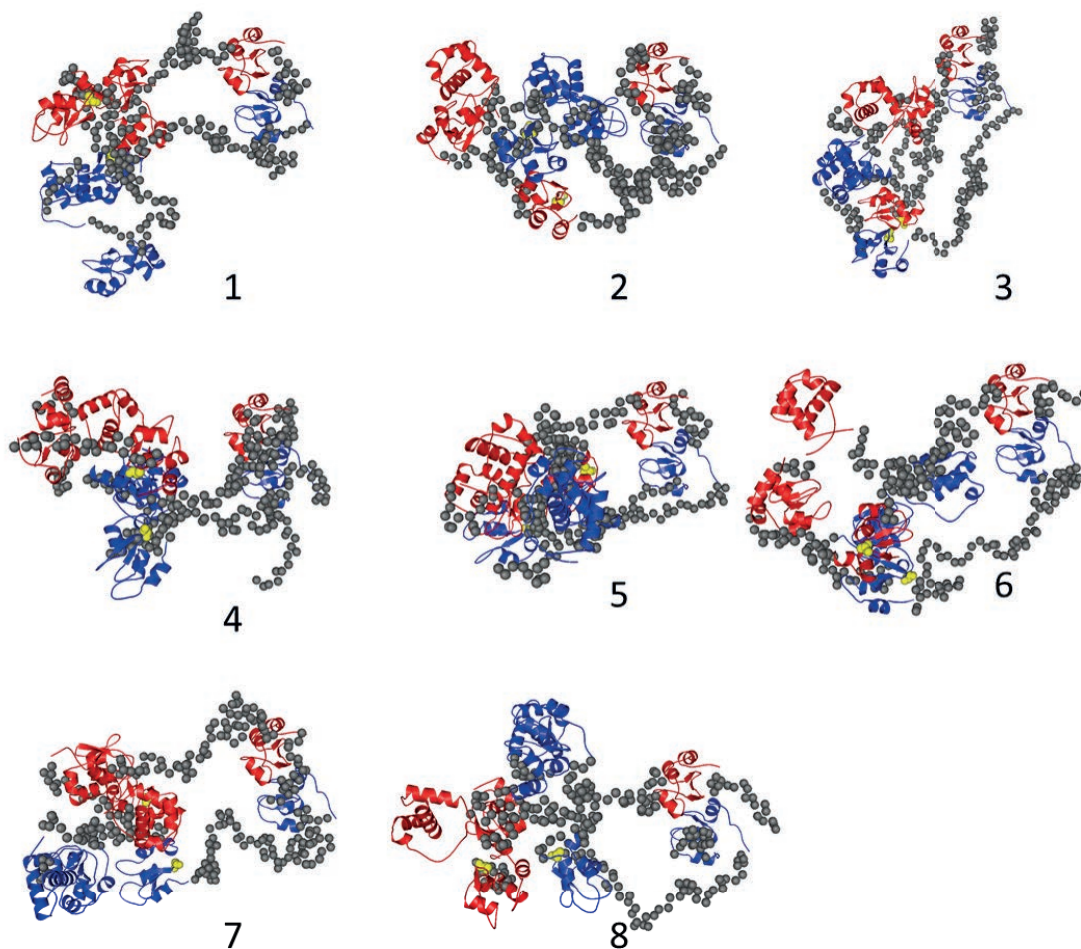


Fig. 8: Rigid body modelling. Representative conformations from rigid body modelling are shown as cartoons (folded domains), and spheres represent linkers and N-terminal residues. The monomeric subunits are in red and blue. Cys202 from the BIR2 domains are shown as yellow spheres.

2.5 Cadmium effects on Superoxide dismutase 1 in human cells

2.5.1 Overview

Cadmium is a toxic environmental and food contaminant whose effects are proving to be increasingly lethal for human health. Cadmium can spread in the environment due to natural processes, like volcanic eruptions, weathering and erosion, but during the last decades its dispersal has been considerably increased due to anthropogenic activities i.e.: i) Mining, smelting and refining of non-ferrous metals; ii) production of cadmium-pigmented plastics, paints and enamels, and cadmium-stabilized polyvinyl chloride (PVC) materials; iii) production and use of agricultural phosphate fertilizers; iiiii) combustion of fossil fuel, burning of municipal waste, in particular cadmium-containing plastics, batteries and electronic refuse (UNEP, 2008). Due to the high solubility of its compounds in water, cadmium gets easily absorbed by plants and thus it enters in the human food chain as a nutritional and tobacco contaminant (Satarug and Moore, 2004; Sarwar et al., 2010). Unlike many other metals that are fundamental for the cellular physiology, cadmium is a xenobiotic substance role for all living organisms. It is a potent cumulative toxin with a very low excretion rate and a half-life that in humans has been estimated around 15-25 years (Suwazono et al., 2009). In mammals, after its absorption through the respiratory and digestive system, cadmium mainly accumulates several tissues including kidneys, liver, lungs, bones, testicles and in the brain, where it exerts its detrimental effects by causing severe oxidative stress (Bertin and Averbeck, 2006; Nair et al., 2013). For these reasons, cadmium holds the seventh position in the ranking of the most hazardous substances for human health, when considering both toxicity and exposure frequency (ATSDR, 2017), and it has been classified as a category 1 carcinogen by the International Agency for Research on Cancer (IARC, 2009). Cadmium is not a Fenton-like metal, and consequently is not responsible for the direct formation of reactive oxygen species (ROS), but rather it increases their intracellular concentration and their damaging effects by altering the balance of the cellular anti-oxidative defence system (Nair et al., 2013). In fact, cadmium is thought to replace metals from

their catalytic sites (Bonomi et al., 1994; Moulis, 2010; Malgieri et al., 2011, 2014), to deplete anti-oxidant metabolites like glutathione, ascorbic acid and vitamin E, to cause mitochondrial damage by inhibiting the electron transport chain and to alter the enzymatic activity of anti-oxidant proteins (Fig. 11) (Thévenod, 2009; Gobe and Crane, 2010; Cuypers et al., 2010; Nair et al., 2013).

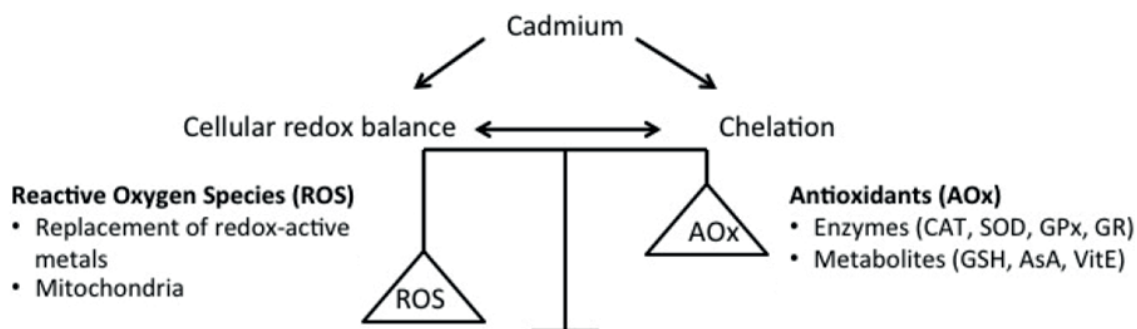


Fig. 11: Schematic overview of the components involved in cellular Cd-induced oxidative stress: Reactive Oxygen Species (ROS); antioxidants (AOx); catalase (CAT); superoxide dismutase (SOD); glutathione peroxidase (GPx); glutathione reductase (GR); glutathione (GSH); ascorbic acid (AsA); vitamin E (VitE); (image credit: taken and modified from Nair et al., 2013).

One of the main players in the cellular defence against cadmium toxicity are metallothioneins (MTs), a family of highly conserved proteins, composed by ~60 amino acids, one third of which are conserved cysteines. The cysteines form two metal-thiolate clusters (α and β), which are capable of binding a series of metal ions, such as Zn^{2+} , Cd^{2+} and Cu^{+} , inducing the folding of the protein (Sutherland and Stillman, 2011). Humans have 11 functional isoforms of MTs, divided in 4 subfamilies (MT1-4), that share a high grade of homology and that are differentially expressed according to the tissue (Coyle et al., 2002). Despite their small size and their simple structure, MTs play a fundamental role in scavenging xenobiotic toxic metals such as Cd^{2+} , Hg^{2+} and Pb^{2+} , radical scavenging, maintaining the intracellular redox balance, protecting against DNA damage, and maintaining the intracellular zinc homeostasis (Cai et al., 2000; Chiaverini and De Ley, 2010; Kimura and Kambe, 2016). The expression of MTs is triggered and enhanced by the intracellular free Zn^{2+} concentration. Specifically, it has been reported that under physiological conditions MTs bind seven Zn^{2+} ions, but when a toxic metal enters in a cell, it binds to MTs,

replacing the Zn^{2+} ions which are released in the cell. The surplus of intracellular free Zn^{2+} then binds to the metal regulatory transcription factor 1 (MTF-1), activating it and triggering the transcription of MTs (Fig. 12).

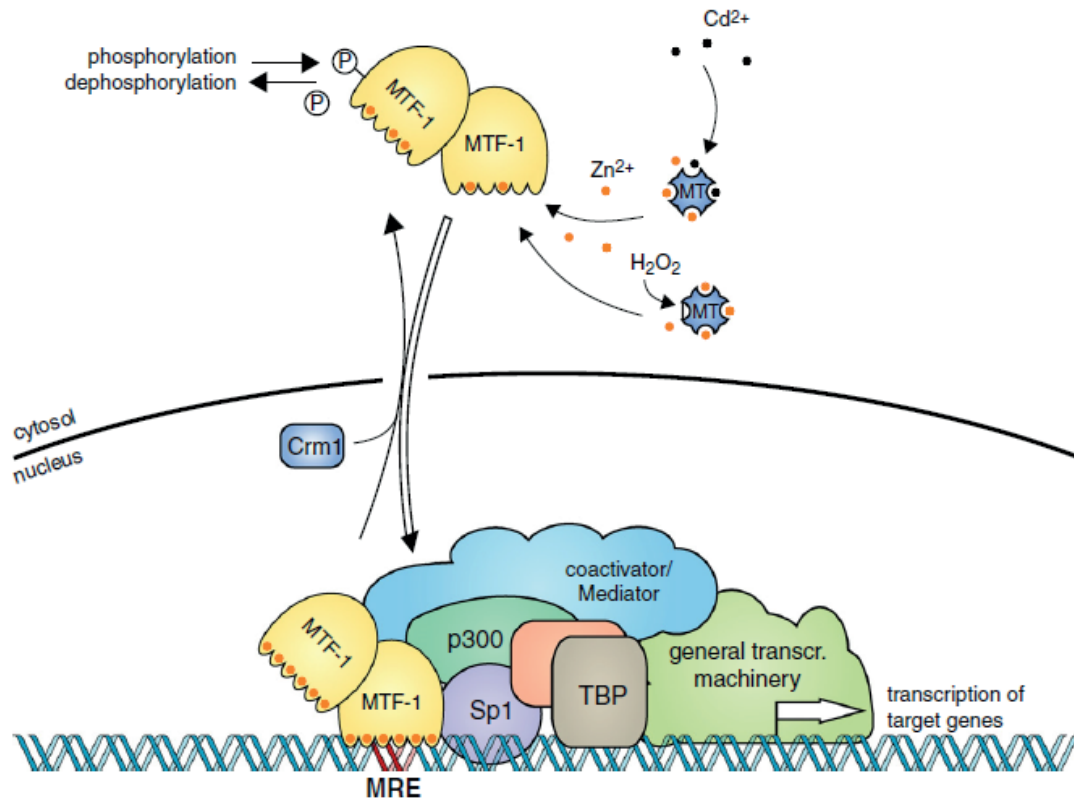


Fig. 12: Overview of mammalian MTF-1 regulation and the transcription mechanism of the genes encoding MTs (image credit: Günther et al., 2012).

Among the anti-oxidant proteins affected by cadmium exposure, literature reports the involvement of cadmium in the alteration of the enzymatic activity of SOD1 (Jurczuk et al., 2004; Thévenod, 2009). SOD1 is a metalloenzyme which exerts an essential anti-oxidant action, catalysing the dismutation of $O_2^{\cdot-}$ to H_2O_2 and O_2 with very high reaction rates (McCord and Fridovich, 1969; Tainer et al., 1982; Getzoff et al., 1992). The enzymatic activity of SOD1 is fundamental for the maintenance of the physiological cellular conditions and requires the correct folding of the protein, which in turn is strictly connected with the metal binding and the disulfide bond formation. In fact, incorrect SOD1 maturation has been associated to the onset of severe disease states, such as amyotrophic lateral sclerosis (ALS) (Rosen et al., 1993; Lindberg et al., 2002; Pasinelli et al.,

2004; Valentine et al., 2005; Banci et al., 2007). *In vitro*, cadmium has been shown to bind to the zinc and copper sites of SOD1 (Kofod et al., 1991), which are required for the structural stability and catalytic activity of SOD1, respectively. Nevertheless, the mechanism by which cadmium affects the enzymatic activity of SOD1 it is not yet clear, i.e. it is not known if cadmium is able to displace one of the metals which are essential for the correct folding and for the catalytic activity of the protein. Consequently, the aim of this study is to evaluate the effects of cadmium exposure on the maturation of SOD1 in human cells by in-cell NMR, in order to determine whether in the cellular environment cadmium is able to bind to the zinc and/or copper sites, or it affects the intracellular SOD1 maturation otherwise.

This study revealed an interesting relationship between the SOD1 redox state, the availability of Zn^{2+} and the Cd^{2+} -induced overexpression of MTs. While Cd^{2+} itself does not directly bind to SOD1, it is able to induce the premature formation of SOD1 intramolecular disulfide bond, interfering with its correct maturation pathway. Furthermore, Cd^{2+} alters the cellular zinc homeostasis by causing a strong induction of MTs. Such induction is negatively modulated by overexpression of SOD1 itself, likely because the increased SOD1 levels interfere with the activation of MTF-1 by binding free Zn^{2+} with high affinity. While in our experiments the levels of SOD1 are artificially increased, our findings suggest that in cells with endogenously high levels of SOD1, such as neurons, under certain conditions, SOD1 itself could sensitize the cells to Cd^{2+} toxicity, by sequestering the Zn^{2+} displaced by Cd^{2+} , inhibiting the cellular response against Cd^{2+} and further altering the cellular redox balance. Finally, as an interesting remark from the methodological point of view, we report that the strong induction of MTs resulted in the observation of NMR signals from MT-2A. To the best of our knowledge, this is the first time that signals from a protein synthesized by genomic DNA, i.e. not delivered into the cells nor ectopically expressed, could be detected by solution NMR in human cells.

2.5.2 Attached manuscript (submitted)

Cadmium effects on superoxide dismutase 1 in human cells revealed by NMR

Polykretis, P.^a, Luchinat, E.^{a,b}, Cencetti, F.^b, Banci, L.^{a,c,1}

^aMagnetic Resonance Center - CERM, University of Florence, Via Luigi Sacconi 6, 50019 Sesto Fiorentino, Florence, Italy.

^bDepartment of Experimental and Clinical Biomedical Sciences "Mario Serio", University of Florence, Viale Morgagni 50, 50134 Florence, Italy.

^cDepartment of Chemistry, University of Florence, Via della Lastruccia 3, 50019 Sesto Fiorentino, Florence, Italy.

¹To whom correspondence should be addressed. Telephone: +39 055 457 4273. Email: banci@cerm.unifi.it

Keywords

cadmium, superoxide dismutase 1, in-cell NMR, oxidative stress, metallothionein.

Abstract

Cadmium is a toxic pollutant that in recent decades has become more widespread in the environment due to anthropogenic activities, significantly increasing the risk of exposure. Concurrently, a continually growing body of research has begun to enumerate the harmful effects that this heavy metal has on human health. Consequently, additional research is required to better understand the mechanism and effects of cadmium at the molecular level. The main mechanism of cadmium toxicity is based on the indirect induction of severe oxidative stress, through several processes that unbalance the antioxidant cellular defence system. In fact, among the many detrimental effects of cadmium, it has been reported its involvement in the alteration of the enzymatic activity of SOD1, one of the main antioxidant proteins of many tissues, including the central nervous system. SOD1 misfolding and aggregation is correlated with cytotoxicity in neurodegenerative diseases such as amyotrophic lateral sclerosis. We assessed the effect of cadmium on SOD1

folding and maturation pathway directly in human cells through in-cell NMR. Cadmium does not directly bind intracellular SOD1, instead causes the formation of its intramolecular disulfide bond in the zinc-bound form. Metallothionein overexpression is strongly induced by cadmium, reaching NMR-detectable levels. The intracellular availability of zinc modulates both SOD1 oxidation and metallothionein overexpression, strengthening the notion that zinc-loaded metallothioneins help maintaining the redox balance under cadmium-induced acute stress.

Significance

Despite a vast body of literature on cadmium toxicity, its underlying molecular mechanisms are not yet fully elucidated. A consequence of cadmium exposure is intracellular redox unbalance and oxidative stress, partly caused by the displacement of native metals from metalloenzymes. Such mechanism was thought to alter the enzymatic activity of SOD1 *in vivo*. We show instead that cadmium does not bind to intracellular SOD1, whereas it interferes with the correct maturation by causing its premature oxidation via an indirect mechanism modulated by metallothionein overexpression and zinc availability. This is the first example of how a high resolution cellular technique such as in-cell NMR can elucidate a long-standing question in the biochemistry of cadmium.

Introduction

Cadmium is a potent environmental and food contaminant that is ranked as the seventh most hazardous substance for human health when considering both toxicity and exposure frequency (1). Furthermore, it has been classified as a category 1 carcinogen by the International Agency for Research on Cancer (2). Cadmium can spread in the environment due to natural processes like volcanic eruptions and erosion, but during recent decades anthropogenic activities such as agriculture and industry have significantly boosted its dispersal in soil and water (3). Cadmium compounds are very soluble in water, facilitating its

uptake by plants and consequently human exposure as a food and tobacco contaminant (4, 5). Cadmium is not a physiological element for any living organism, and furthermore is a cumulative toxin with an extremely long estimated half-life (up to 13.6 - 23.5 years) due to its very low excretion rate (6). In mammals, the main accumulation sites of cadmium are kidneys, liver, lungs, bone, testes and brain, where it causes severe oxidative stress and other detrimental effects (7, 8). Unlike iron and copper, cadmium is not a Fenton-like metal, consequently it is not involved directly in the production of Reactive Oxygen Species (ROS). Rather, it increases their intracellular production and their harmful effects by altering the balance of the cellular anti-oxidative defence system. In fact, cadmium is thought to be responsible for the replacement of metals from their catalytic sites (9-12); the depletion of anti-oxidant metabolites, like glutathione, ascorbic acid and vitamin E; the inhibition of the electron transport chain, resulting in mitochondrial damage; and the alteration of the enzymatic activity of anti-oxidant proteins (13-15). One of the main cellular defence tools against cadmium are metallothioneins (MTs), a family of highly conserved, cysteine-rich small proteins with several key functions: toxic metal and radical scavenging, maintenance of the intracellular zinc homeostasis, maintenance of the intracellular redox balance and protection against DNA damage (16-18). Mammalian MTs have about 60 amino acids, one third of which are cysteines, forming two metal-thiolate clusters. The protein fold is induced by metal ions (such as Zn^{2+} , Cd^{2+} and Cu^+), and cluster formation (19). Human MTs have 11 functional isoforms divided in 4 subfamilies (MT1-4), which share a high degree of homology and are differentially expressed depending on the tissue (20). Among the anti-oxidant proteins affected by cadmium intoxication, literature reports the involvement of cadmium in the alteration of the enzymatic activity of Superoxide dismutase 1 (SOD1) (13). SOD1 is a metalloprotein that exerts a fundamental anti-oxidant role catalysing the dismutation of $O_2^{\bullet-}$ to H_2O_2 and O_2 with extremely high reaction rates (21-23). SOD1 enzymatic activity is essential for the maintenance of the physiological cellular conditions and requires correct protein folding, metal binding and disulfide bond formation. The impairment of SOD1

maturation has been also related to the onset of severe disease states, including amyotrophic lateral sclerosis (ALS) (24-28).

In vitro, cadmium has been shown to bind to the zinc and copper sites of SOD1 (29), which are necessary for the structural stability and catalytic activity of SOD1, respectively. *In vivo*, however, opposing effects have been reported on SOD1 activity in response to cadmium exposure, and evidence of alteration at the protein level is lacking (30-32). Therefore, it is not clear whether/how cadmium affects SOD1 folding and metallation within the cell, i.e. in the presence of the native SOD1 metal ions and under the control of the cellular metal and redox homeostasis.

Given these contrasting premises, we sought to evaluate the effects of cadmium treatment on the maturation of SOD1 in human cells by in-cell NMR, to determine whether cadmium binds to the zinc and/or copper sites or it affects intracellular SOD1 maturation by other mechanisms. To this aim, in-cell NMR is the ideal technique, as it is able to analyze proteins at atomic resolution directly in living cells. The same technique has been applied previously to observe changes in the intracellular SOD1 folding, metallation and redox state as a consequence of the physiological maturation and/or in response to external stimuli (33-36).

Materials and Methods

In-cell NMR:

In-cell NMR experiments have been performed as previously described (37) on living human embryonic kidney cells (HEK293T), under three main experimental conditions: i) exposure to Zn²⁺ (added in the culture at the time of transfection with SOD1); ii) exposure to Cd²⁺ (added in the culture 24h after the transfection with SOD1); iii) exposure to Zn²⁺ and Cd²⁺ (both added in the culture at the aforementioned times). HEK293T cells were grown on uncoated 75 cm² plastic flasks at 37 °C in 5% CO₂ atmosphere, and were maintained in Dulbecco's modified Eagle's medium (DMEM; high glucose, D6546, Sigma) supplemented with L-glutamine, antibiotics (penicillin and streptomycin) and

10% FBS (Gibco). Cells were transiently transfected with the pHLsec plasmid (38) encoding human SOD1, using polyethylenimine (PEI) in the ratio 1:1, in ^{15}N labelled media (BioExpress6000, Cambridge Isotope Laboratories, Inc.), supplemented 2% FBS in the presence/absence of Zn^{2+} as ZnSO_4 10 μM . 24 hours after the transfection, 10 μM of CdCl_2 was added to the cell cultures; such concentration was chosen considering previous experiments performed on Hep3B and N2A cells (31, 39). After 24 hours of exposure to cadmium, the cells were collected and placed in a 3 mm Shigemi NMR tube for NMR analysis. ^1H WATERGATE (3-9-19) and ^1H - ^{15}N SOFAST-HMQC NMR spectra were acquired on living HEK293T cells and on lysates at a 950 MHz Bruker Avance III or at a 900 MHz Bruker Avance HD spectrometer both equipped with a TCI CryoProbe, at 308 K. The cell lysates were obtained by freeze-thaw lysis in phosphate buffered saline (PBS) buffer, pH 7.4, followed by centrifugation at 14000 rpm. For the [^{15}N]-cysteine selective labelling of metallothioneins, untransfected HEK293T cells were grown in homemade medium containing [^{15}N]-cysteine (Cambridge Isotope Laboratories, Inc.); NMR spectra were acquired on the corresponding cell lysate at 298 K. All NMR spectra were acquired and processed using Bruker Topspin software.

The intracellular oxidation state of E,Zn-SOD1 was determined from the intensities of the signals arising from G10 and N53 N δ 1 in each oxidation state in the ^1H - ^{15}N NMR spectra. The amount of oxidized/reduced E,Zn-SOD1 in each condition are reported as percentages over total E,Zn-SOD1 \pm s.d. calculated over two identical cell samples.

In vitro NMR:

Recombinant SOD1 was demetallated as previously described (40) by repeated dialyses against 10 mM EDTA in 50 mM acetic acid at pH 3.5. The buffer was then replaced with PBS, pH 7.4. Reduction of SOD1 disulfide bond was performed by incubating apo-SOD1^{SS} with 50 mM of DTT for 40 min at 37 °C. DTT was then removed in oxygen-free PBS buffer.

In vitro NMR titration experiments were performed at 950 MHz in anaerobic conditions. E,Zn-SOD1^{SH} was obtained by titrating 150 μM apo-SOD1^{SH} in PBS

buffer, pH 7.4, with 1 equivalent of ZnCl_2 . Titration with Cd^{2+} was performed by addition of increasing equivalents of CdCl_2 to a sample of 150 μM apo-SOD1^{SH}. ^1H WATERGATE (3-9-19) and ^1H - ^{15}N SOFAST-HMQC NMR spectra were acquired at 298 K after each addition.

Real-Time PCR:

Gene expression analysis by Real-Time PCR has been performed using $2^{(-\Delta\Delta\text{CT})}$ comparative method of quantification (41). Briefly, total RNA (1 μg), extracted with TriReagentTM (Sigma-Aldrich S.r.l. Milan, Italy at <http://www.sigma-aldrich.com>) was reverse transcribed using iScriptTM cDNA Synthesis Kit for RT-qPCR (Bio-Rad Laboratories S.r.l., Segrate (MI), Italy, at <http://www.bio-rad.com/>) according to the manufacturer's instructions. Human specific TaqMan Gene Expression Assays employed for gene expression studies were purchased from Thermo Fisher Scientific INC and listed in Table S1. The quantification of target gene mRNA levels was performed employing TaqMan Universal Master Mix (Thermo Fisher Scientific INC). Each measurement was carried out in triplicate, using the automated ABI Prism 7500 Sequence Detector System (Thermo Fisher Scientific INC) as described previously (42). The quantification has been performed by simultaneous amplification of the target gene together with the housekeeping (GAPDH) in order to normalize expression data. Results were analysed by ABI Prism Sequence Detection Systems software, version 1.7 (Applied Biosystems, Foster City, CA). The $2^{(-\Delta\Delta\text{CT})}$ method was used as a comparative method of quantification.

Results

SOD1 overexpressed in human cells either under basal conditions or exposed to Cd^{2+} and/or Zn^{2+} was analyzed by in-cell NMR to determine its metallation and redox state. Under basal conditions, two states of SOD1 were observed, i.e. the disulfide-reduced, monomeric metal-free protein (apo-SOD1^{SH}) and the dimeric form with one Zn^{2+} bound per monomer (E,Zn-SOD1, Fig. 1), mostly in

the reduced state ($66 \pm 5\%$ E,Zn-SOD1^{SH} over total E,Zn-SOD1). This is consistent with previous reports and is due to SOD1 being in excess with respect to the available intracellular zinc (33). When Cd²⁺ was added to the cells, a sizable fraction ($70 \pm 4\%$) of the zinc-bound form was found to be oxidized (E,Zn-SOD1^{SS}), as revealed by the changes in relative signal intensity in the 2D NMR spectra, while the apo-SOD1^{SH} form was unaffected (Fig. 1). Cadmium binding to the zinc or to the copper binding site was not observed in our experimental conditions, as determined by comparison with the *in vitro* NMR spectra. Indeed, the signals of intracellular SOD1 (Fig. 2a) match those of *in vitro* E,Zn-SOD1 (Fig. 2b), while those of SOD1 metallated *in vitro* with either up to four equivalents of Cd²⁺ per SOD1 monomer have different chemical shifts, both in the amide (Fig. 2c,d) and in the histidine region (Fig. 2e).

When excess Zn²⁺ was added to the cell culture, intracellular SOD1 was fully metallated with one Zn²⁺ per monomer, and mostly found in the reduced state ($85 \pm 4\%$ E,Zn-SOD1^{SH}), as previously reported (33, 35). When both Zn²⁺ and Cd²⁺ were supplemented, a small fraction ($34 \pm 10\%$) of SOD1 was oxidized (E,Zn-SOD1^{SS}), while the rest of the protein remained reduced (E,Zn-SOD1^{SH}), as that observed in the Zn²⁺-treated cell sample (Fig. 3). The considerably smaller fraction of oxidized SOD1, compared to the sample supplemented only with Cd²⁺, suggested that a protective mechanism against oxidative stress had been activated by supplementing Zn²⁺. We hypothesized that such effect could have been exerted by metallothioneins (MTs), considering their protective role against cadmium, their involvement in zinc homeostasis and their intracellular anti-oxidant action. Indeed, MTs are well known to be overexpressed in cell lines and tissues as a consequence of cadmium exposure (43, 44). Interestingly, analysing the NMR data, several additional amide crosspeaks not originating from any known state of SOD1 were observed in the 2D spectra of cells treated with both Cd²⁺ and Zn²⁺ (Fig. S1). To further investigate the origin of these signals, we performed additional in-cell NMR experiments on cells not transfected with the plasmid encoding SOD1, that were grown in either uniform-¹⁵N or [¹⁵N-cysteine] labelled medium and subsequently exposed to Cd²⁺. The unknown crosspeaks were also present in the resulting NMR spectra

(Fig. 4a), indicating that they did not arise from SOD1 but from some other protein(s) upregulated upon Cd^{2+} treatment. Strikingly, many signals (~ 20) were also present in the [^{15}N -cysteine] labelled sample (Fig. 4a and Fig. S2). Such a high ratio of cysteine residues is typical of MTs. Therefore, MT overexpression could explain the additional crosspeaks in Cd^{2+} -treated cells, and the lower amount of oxidized SOD1.

To confirm that MTs are overexpressed as a consequence of cadmium exposure and to identify which MT isoforms are upregulated the most, we performed Real-Time PCR experiments on mRNA extracts from cells either untreated or treated with Cd^{2+} and/or Zn^{2+} . Real-Time PCR analysis revealed that, indeed, expression of MTs was greatly increased upon Cd^{2+} treatment in our experimental conditions (Fig. 4b and Table S2). Specifically, in cells treated with Cd^{2+} MT-1X expression was increased ~ 280 -fold compared to the untreated cell sample, while MT-2A expression was increased ~ 210 -fold; MT-1F was also overexpressed to a lesser extent (~ 20 -fold). Considering that in the control sample MT-1X and MT-2A are expressed respectively ~ 8 and ~ 60 times more than MT-1A (taken as reference, Fig. 4c and Table S2), the levels of MT-1X and MT-2A in Cd^{2+} -treated cells reached up to ~ 2200 and ~ 12500 times the basal MT-1A levels, respectively, by far higher than any other isoform, thus suggesting that the observed NMR signals arise from these isoforms. In cells treated with both Cd^{2+} and Zn^{2+} , an increase in the levels of MT-1X and (even more pronounced) MT-2A was observed (respectively, ~ 290 - and ~ 320 -fold), while in cells treated only with Zn^{2+} a much lower MT overexpression was observed (Fig. 4d,e and Table S3).

Real-Time PCR MTs expression analysis was also performed on cells overexpressing SOD1 as it occurs in the in-cell NMR samples upon supplementation of Cd^{2+} and/or Zn^{2+} . Interestingly, in cells expressing SOD1 a different behaviour was observed in defect of Zn^{2+} versus excess of Zn^{2+} , upon Cd^{2+} treatment. In defect of Zn^{2+} , Cd^{2+} treatment induced the expression of MT-1X and MT-2A at lower levels (~ 210 - and ~ 110 -fold, respectively, compared to basal levels) than in untransfected cells, while excess Zn^{2+} in SOD1-expressing cells restored the Cd^{2+} -induced expression of MT-1X and MT-2A to even higher

levels (~860- and ~250-fold, respectively) than in untransfected cells (Fig. 4e and Table S3). These data are consistent with the fact that MTs were not detected by NMR in cells expressing SOD1 in defect of Zn²⁺ (Fig. S3).

Upregulation of MTs was much lower in cells (both untransfected and transfected with SOD1) treated with Zn²⁺ in excess but not exposed to Cd²⁺ (Fig. 4d). Taken together, these data indicate that cadmium is the main trigger of MT overexpression and that SOD1 and zinc supplementation can modulate Cd²⁺-induced MT overexpression in opposite ways.

Discussion

In-cell NMR allows a direct assessment of the intracellular state of SOD1 upon Cd²⁺ treatment, and therefore can provide a close-to-physiological picture of the effect of cadmium exposure on SOD1 in human cells. Previous *in vitro* NMR studies demonstrated that Cd²⁺ is able to bind to the zinc and copper sites of SOD1 (29), while studies on animal models showed that Cd²⁺ affects the superoxide dismutase activity in several tissues (30–32). We therefore sought to determine whether direct binding of Cd²⁺ to SOD1 can occur in living cells. By in-cell NMR, we did not observe any direct Cd²⁺ binding to SOD1, as SOD1 was present only with one Zn²⁺ bound per monomer or in the apo state. Indeed, both the amide chemical shifts and those arising from the metal-coordinating histidines observed in the Cd²⁺-treated cells were identical to those of E,Zn-SOD1 *in vitro*, and differed from those observed when apo-SOD1 was titrated *in vitro* with increasing equivalents of Cd²⁺ (Fig. 2). Moreover, different species were formed simultaneously during the titration and residual apo-SOD1 was still present after up to two equivalents of Cd²⁺. This behaviour suggests that, *in vitro*, Cd²⁺ binds to SOD1 relatively weakly and with low selectivity towards either the zinc or the copper site, and provides further evidence against Cd²⁺ binding to SOD1 in cells.

Instead, a clear effect of Cd²⁺ treatment was the oxidation of intracellular SOD1, i.e. the formation of the intrasubunit disulfide bond between C57 and C146. This outcome is likely a consequence of an intracellular redox unbalance caused

by Cd^{2+} . The disulfide bond formation is required for the correct maturation of SOD1, as it stabilizes the protein structure and is essential for its activity (45, 46). Moreover, the ability of an exogenous redox-reactive compound to stabilize SOD1 by promoting disulfide oxidation has also been reported (36). While cysteine oxidation contributes to stabilize the protein, it could interfere with the native maturation pathway, as SOD1 needs to interact with its partner copper chaperone for SOD1 (CCS) in order to bind copper (47, 48). SOD1 interacts with CCS more efficiently in the reduced state (49, 50). Upon interaction, CCS delivers copper to SOD1 and catalyzes its oxidation, thus producing mature SOD1 (51, 52). The premature oxidation of SOD1 could therefore prevent the interaction with CCS and impair copper delivery, as shown previously in yeast (53) and with human SOD1 *in vitro* (52). Such effect would be consistent with the decrease of superoxide dismutase activity reported *in vivo* (13, 30). Cd^{2+} -mediated SOD1 oxidation did not occur in the presence of excess Zn^{2+} , thus suggesting that Zn^{2+} could modulate the extent of the effect of Cd^{2+} . Notably, this mechanism cannot involve mature Cu,Zn-SOD1, as the disulfide bond is already formed and Cd^{2+} would not be able to replace either zinc or copper, which is bound to SOD1 with even higher affinity.

Furthermore, we observed that Cd^{2+} treatment strongly induced the overexpression of the metallothionein isoforms MT-1X and MT-2A. Interestingly, while MT overexpression is a well known consequence of Cd^{2+} exposure (43, 44), MT-1X and MT-2A reached such high levels in our experimental conditions that they could be observed by in-cell NMR. While in principle the high spectral resolution should allow separating the signals of MT-1X and MT-2A, only one set of resonances could be identified due to the low signal-to-noise ratio and likely because most signals have the same chemical shift due to the high structural similarity of the two isoforms, which have an overall sequence identity > 90% and share a central stretch of 38 identical residues. Strong MT induction required the presence of Cd^{2+} , and was also observed in HEK293T not transfected with the SOD1 gene, where Zn^{2+} supplementation further potentiated the MT induction. Interestingly, SOD1 overexpression negatively modulated the level of Cd^{2+} -mediated MT induction,

and indeed in such experimental conditions, where SOD1 was partially oxidized upon Cd^{2+} treatment, MT-1X/MT-2A did not reach sufficiently high levels to be detected in the NMR spectrum. Conversely, supplementation of both Cd^{2+} and Zn^{2+} to cells overexpressing SOD1, i.e. in the experimental conditions where SOD1 was mostly reduced, Cd^{2+} -mediated MT induction was restored, and high MT-1X/MT-2A levels were observed in the NMR spectrum. Such interplay between Zn^{2+} , MT expression and SOD1 oxidation can be rationalized by considering the role of MTs in the cellular homeostasis of zinc. Zinc is an essential metal for the correct functionality and health of the cell. However, due to its high affinity for biological molecules, its intracellular availability has to be regulated to avoid uncontrolled binding to non-native acceptors. MTs, along with the other high affinity zinc-binding proteins, contribute to buffering the intracellular Zn^{2+} concentration (18). Furthermore, both MTs and Zn^{2+} are involved in the cellular redox homeostasis (54, 18). When intracellular Zn^{2+} increases, it binds to the metal regulatory transcription factor-1 (MTF-1), activating it and triggering the transcription of more MTs (55). Consequently, when Cd^{2+} is added to the cells it displaces Zn^{2+} from MTs and other proteins, releasing it in the cytoplasm and causing it to activate MTF-1, inducing MTs overexpression. In turn, overexpressed MTs protect the cells by directly binding Cd^{2+} and possibly by exerting other antioxidant functions (18). When Cd^{2+} is added to cells overexpressing SOD1, the released Zn^{2+} is immediately sequestered by SOD1, which has a much higher affinity than MTF-1 and MTs, preventing the activation of MTF-1 and decreasing MTs overexpression as a consequence. Instead, when both Zn^{2+} and Cd^{2+} are supplemented, overexpressed SOD1 is fully metallated by the excess of Zn^{2+} , so that the amount released by the MTs can still bind to MTF-1, restoring the high induction of MTs to NMR-detectable levels. Finally, the different oxidation state of SOD1 observed when supplementing both Zn^{2+} and Cd^{2+} can be explained with the fact that in cells with higher levels of MTs the cellular redox balance is partially restored, preventing the premature oxidation of SOD1.

Conclusions

In this work, the effect of cadmium treatment on the metallation and redox state of SOD1 was investigated directly in human cells by in-cell NMR. Our study revealed an interesting relationship between the SOD1 redox state, the availability of Zn^{2+} and the Cd^{2+} -induced overexpression of MTs. While Cd^{2+} itself does not bind SOD1 in place of Zn^{2+} , it is able to induce the premature formation of SOD1 intramolecular disulfide bond, interfering with its correct maturation pathway. Furthermore, Cd^{2+} alters the cellular zinc homeostasis causing a strong induction of MTs. Such induction is negatively modulated by the overexpression of SOD1 itself, likely because the increased SOD1 levels interfere with the activation of the MT transcription factor MTF-1. While in our experiments the levels of SOD1 are artificially increased, our findings suggest that in cells with endogenously high levels of SOD1, such as neurons, under certain conditions, SOD1 itself could sensitize the cells to Cd^{2+} toxicity, by sequestering the Zn^{2+} displaced by Cd^{2+} , inhibiting the cellular response against Cd^{2+} and further altering the cellular redox balance.

Finally, as an interesting remark from the methodological point of view, we report that the strong induction of MTs resulted in the observation of NMR signals from MT-1X/MT-2A. To the best of our knowledge, this is the first time that signals from a protein synthesized by genomic DNA, i.e. not delivered into the cells nor ectopically expressed, could be detected by solution NMR in human cells.

Acknowledgements

Recombinant SOD1 was kindly provided by Dr. L. Barbieri (CERM/CIRMMMP, Italy). The authors acknowledge the support and the use of resources of Instruct-ERIC, a Landmark ESFRI project, and specifically the CERM/CIRMMMP Italy Centre.

Author Contributions

P.P., E.L. and L.B. conceived the work; P.P. and E.L. designed the experiments; P.P. maintained the cells and produced the samples for NMR and RT-PCR; E.L. performed the NMR experiments and analyzed the data; F.C. performed the RT-PCR experiment and analyzed the data; P.P, E.L., F.C. and L.B. wrote the manuscript.

References

1. Substance Priority List | ATSDR (2018) Available at: <https://www.atsdr.cdc.gov/spl/index.html> [Accessed August 3, 2018].
2. List of classifications, Volumes 1–122 – IARC Available at: <https://monographs.iarc.fr/list-of-classifications-volumes/> [Accessed August 3, 2018].
3. Järup L, Akesson A (2009) Current status of cadmium as an environmental health problem. *Toxicol Appl Pharmacol* 238(3):201–208.
4. Satarug S, Moore MR (2004) Adverse Health Effects of Chronic Exposure to Low-Level Cadmium in Foodstuffs and Cigarette Smoke. *Environ Health Perspect* 112(10):1099–1103.
5. Sarwar N, et al. (2010) Role of mineral nutrition in minimizing cadmium accumulation by plants. *J Sci Food Agric* 90(6):925–937.
6. Suwazono Y, et al. (2009) Biological half-life of cadmium in the urine of inhabitants after cessation of cadmium exposure. *Biomark Biochem Indic Expo Response Susceptibility Chem* 14(2):77–81.
7. Bertin G, Averbeck D (2006) Cadmium: cellular effects, modifications of biomolecules, modulation of DNA repair and genotoxic consequences (a review). *Biochimie* 88(11):1549–1559.
8. Nair AR, DeGheselle O, Smeets K, Van Kerkhove E, Cuypers A (2013) Cadmium-Induced Pathologies: Where Is the Oxidative Balance Lost (or Not)? *Int J Mol Sci* 14(3):6116–6143.

9. Bonomi F, Ganadu ML, Lubinu G, Pagani S (1994) Reversible and non-denaturing replacement of iron by cadmium in *Clostridium pasteurianum* ferredoxin. *Eur J Biochem* 222(2):639–644.
10. Moulis J-M (2010) Cellular mechanisms of cadmium toxicity related to the homeostasis of essential metals. *BioMetals* 23(5):877–896.
11. Malgieri G, et al. (2011) Zinc to cadmium replacement in the A. thaliana SUPERMAN Cys2 His2 zinc finger induces structural rearrangements of typical DNA base determinant positions. *Biopolymers* 95(11):801–810.
12. Malgieri G, et al. (2014) Zinc to cadmium replacement in the prokaryotic zinc-finger domain. *Metallomics* 6(1):96–104.
13. Thévenod F (2009) Cadmium and cellular signaling cascades: To be or not to be? *Toxicol Appl Pharmacol* 238(3):221–239.
14. Gobe G, Crane D (2010) Mitochondria, reactive oxygen species and cadmium toxicity in the kidney. *Toxicol Lett* 198(1):49–55.
15. Cuypers A, et al. (2010) Cadmium stress: an oxidative challenge. *Biomaterials Int J Role Met Ions Biol Biochem Med* 23(5):927–940.
16. Cai L, Klein JB, Kang YJ (2000) Metallothionein inhibits peroxynitrite-induced DNA and lipoprotein damage. *J Biol Chem* 275(50):38957–38960.
17. Chiaverini N, De Ley M (2010) Protective effect of metallothionein on oxidative stress-induced DNA damage. *Free Radic Res* 44(6):605–613.
18. Kimura T, Kambe T (2016) The Functions of Metallothionein and ZIP and ZnT Transporters: An Overview and Perspective. *Int J Mol Sci* 17(3):336.
19. Sutherland DEK, Stillman MJ (2011) The “magic numbers” of metallothionein. *Met Integr Biometal Sci* 3(5):444–463.
20. Coyle P, Philcox JC, Carey LC, Rofe AM (2002) Metallothionein: the multipurpose protein. *Cell Mol Life Sci CMLS* 59(4):627–647.
21. McCord JM, Fridovich I (1969) Superoxide dismutase. An enzymic function for erythrocyte hemocuprein (hemocuprein). *J Biol Chem* 244(22):6049–6055.
22. Tainer JA, Getzoff ED, Beem KM, Richardson JS, Richardson DC (1982) Determination and analysis of the 2 A-structure of copper, zinc superoxide dismutase. *J Mol Biol* 160(2):181–217.
23. Getzoff ED, et al. (1992) Faster superoxide dismutase mutants designed by enhancing electrostatic guidance. *Nature* 358(6384):347–351.

24. Rosen DR, et al. (1993) Mutations in Cu/Zn superoxide dismutase gene are associated with familial amyotrophic lateral sclerosis. *Nature* 362(6415):59–62.
25. Lindberg MJ, Tibell L, Oliveberg M (2002) Common denominator of Cu/Zn superoxide dismutase mutants associated with amyotrophic lateral sclerosis: decreased stability of the apo state. *Proc Natl Acad Sci U S A* 99(26):16607–16612.
26. Pasinelli P, et al. (2004) Amyotrophic Lateral Sclerosis-Associated SOD1 Mutant Proteins Bind and Aggregate with Bcl-2 in Spinal Cord Mitochondria. *Neuron* 43(1):19–30.
27. Valentine JS, Doucette PA, Zittin Potter S (2005) Copper-zinc superoxide dismutase and amyotrophic lateral sclerosis. *Annu Rev Biochem* 74:563–593.
28. Banci L, et al. (2007) Metal-free superoxide dismutase forms soluble oligomers under physiological conditions: a possible general mechanism for familial ALS. *Proc Natl Acad Sci U S A* 104(27):11263–11267.
29. Kofod P, Bauer R, Danielsen E, Larsen E, Bjerrum MJ (1991) ¹¹³Cd-NMR investigation of a cadmium-substituted copper, zinc-containing superoxide dismutase from yeast. *Eur J Biochem* 198(3):607–611.
30. Jurczuk M, Brzóska M, Moniuszko-Jakoniuk J, Gałżyn-Sidorczuk M, Kulikowska-Karpińska E (2004) Antioxidant enzymes activity and lipid peroxidation in liver and kidney of rats exposed to cadmium and ethanol. *Food Chem Toxicol* 42(3):429–438.
31. Huang Y-H, et al. (2006) Effects of cadmium on structure and enzymatic activity of Cu,Zn-SOD and oxidative status in neural cells. *J Cell Biochem* 98(3):577–589.
32. Wang J, et al. (2015) Molecular mechanism on cadmium-induced activity changes of catalase and superoxide dismutase. *Int J Biol Macromol* 77:59–67.
33. Banci L, et al. (2013) Atomic-resolution monitoring of protein maturation in live human cells by NMR. *Nat Chem Biol* 9(5):297–299.
34. Luchinat E, et al. (2014) In-cell NMR reveals potential precursor of toxic species from SOD1 fALS mutants. *Nat Commun* 5:5502.
35. Mercatelli E, Barbieri L, Luchinat E, Banci L (2016) Direct structural evidence of protein redox regulation obtained by in-cell NMR. *Biochim Biophys Acta* 1863(2):198–204.
36. Capper MJ, et al. (2018) The cysteine-reactive small molecule ebselen facilitates effective SOD1 maturation. *Nat Commun* 9(1):1693.

37. Barbieri L, Luchinat E, Banci L (2016) Characterization of proteins by in-cell NMR spectroscopy in cultured mammalian cells. *Nat Protoc* 11(6):1101–1111.
38. Aricescu AR, Lu W, Jones EY (2006) A time- and cost-efficient system for high-level protein production in mammalian cells. *Acta Crystallogr D Biol Crystallogr* 62(Pt 10):1243–1250.
39. Lemarié A, et al. (2004) Cadmium induces caspase-independent apoptosis in liver Hep3B cells: role for calcium in signaling oxidative stress-related impairment of mitochondria and relocation of endonuclease G and apoptosis-inducing factor. *Free Radic Biol Med* 36(12):1517–1531.
40. Banci L, Barbieri L, Bertini I, Cantini F, Luchinat E (2011) In-cell NMR in *E. coli* to monitor maturation steps of hSOD1. *PloS One* 6(8):e23561.
41. Schmittgen TD, Livak KJ (2008) Analyzing real-time PCR data by the comparative C(T) method. *Nat Protoc* 3(6):1101–1108.
42. Cencetti F, Bernacchioni C, Nincheri P, Donati C, Bruni P (2010) Transforming growth factor-beta1 induces transdifferentiation of myoblasts into myofibroblasts via up-regulation of sphingosine kinase-1/S1P3 axis. *Mol Biol Cell* 21(6):1111–1124.
43. Andrews GK (2000) Regulation of metallothionein gene expression by oxidative stress and metal ions. *Biochem Pharmacol* 59(1):95–104.
44. Klaassen CD, Liu J, Diwan BA (2009) Metallothionein Protection of Cadmium Toxicity. *Toxicol Appl Pharmacol* 238(3):215–220.
45. Arnesano F, et al. (2004) The unusually stable quaternary structure of human Cu,Zn-superoxide dismutase 1 is controlled by both metal occupancy and disulfide status. *J Biol Chem* 279(46):47998–48003.
46. Furukawa Y, O'Halloran TV (2006) Posttranslational modifications in Cu,Zn-superoxide dismutase and mutations associated with amyotrophic lateral sclerosis. *Antioxid Redox Signal* 8(5–6):847–867.
47. Casareno RL, Waggoner D, Gitlin JD (1998) The copper chaperone CCS directly interacts with copper/zinc superoxide dismutase. *J Biol Chem* 273(37):23625–23628.
48. Culotta VC, Yang M, O'Halloran TV (2006) Activation of superoxide dismutases: putting the metal to the pedal. *Biochim Biophys Acta* 1763(7):747–758.
49. Wright GSA, Antonyuk SV, Hasnain SS (2016) A faulty interaction between SOD1 and hCCS in neurodegenerative disease. *Sci Rep* 6(1). doi:10.1038/srep27691.

50. Luchinat E, Barbieri L, Banci L (2017) A molecular chaperone activity of CCS restores the maturation of SOD1 fALS mutants. *Sci Rep* 7(1):17433.
51. Lamb AL, Torres AS, O'Halloran TV, Rosenzweig AC (2000) Heterodimer formation between superoxide dismutase and its copper chaperone. *Biochemistry* 39(48):14720–14727.
52. Banci L, et al. (2012) Human superoxide dismutase 1 (hSOD1) maturation through interaction with human copper chaperone for SOD1 (hCCS). *Proc Natl Acad Sci* 109(34):13555–13560.
53. Furukawa Y, Torres AS, O'Halloran TV (2004) Oxygen-induced maturation of SOD1: a key role for disulfide formation by the copper chaperone CCS. *EMBO J* 23(14):2872–2881.
54. Oteiza PI (2012) Zinc and the modulation of redox homeostasis. *Free Radic Biol Med* 53(9):1748–1759.
55. Günther V, Lindert U, Schaffner W (2012) The taste of heavy metals: gene regulation by MTF-1. *Biochim Biophys Acta* 1823(9):1416–1425.

Figures

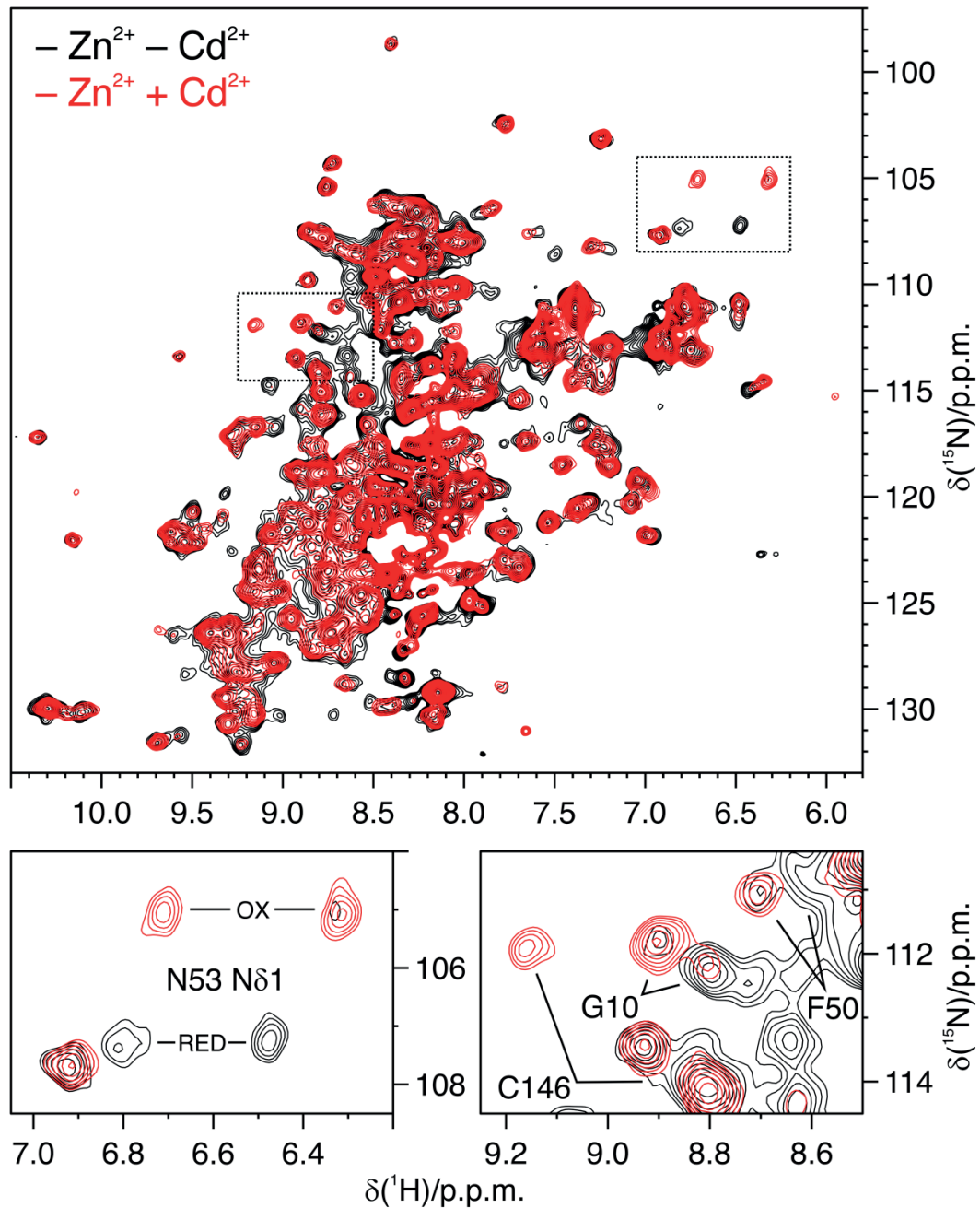


Fig. 1. Cd^{2+} induces intracellular SOD1 oxidation. Overlay of ^1H - ^{15}N NMR spectra acquired on human cells expressing [U- ^{15}N] labelled SOD1 in defect of Zn^{2+} either untreated (black) or treated (red) with Cd^{2+} in the external medium. The bottom panels show enlarged areas of the whole spectra (dotted rectangles). Representative signals affected by the formation of the C57-C146 disulfide bond are labelled.

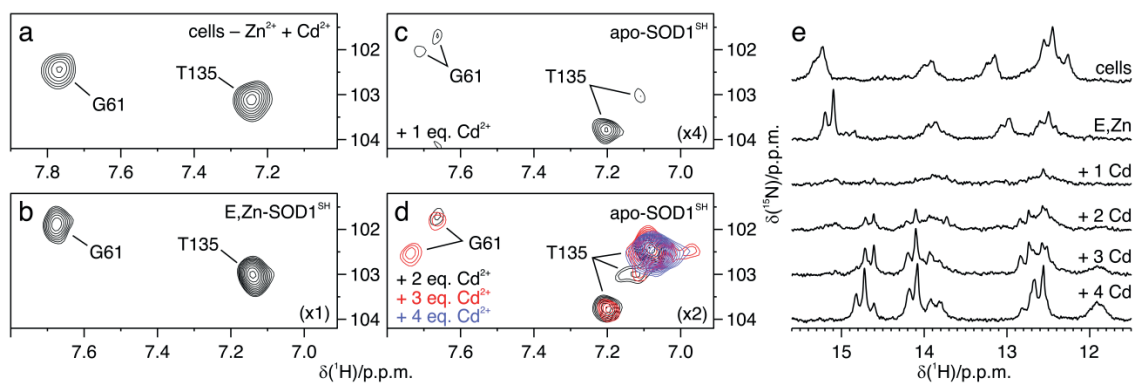


Fig. 2. Intracellular SOD1 binds Zn^{2+} , not Cd^{2+} . Enlarged view of 1H - ^{15}N NMR spectra of (a) Cd^{2+} -treated human cells expressing [U- ^{15}N] labelled SOD1 in defect of Zn^{2+} ; (b) E,Zn-SOD1^{SH} *in vitro*; (c) apo-SOD1^{SH} titrated *in vitro* with 1 equivalent per monomer of Cd^{2+} ; (d) the same sample of (c) titrated with 2 (black), 3 (red) and 4 (blue) equivalents per monomer of Cd^{2+} . The signals sensitive to different metallation states (arising from G61 and T135) are labelled. (e) Imino region of the 1H NMR spectra acquired on the same samples as in (a-d).

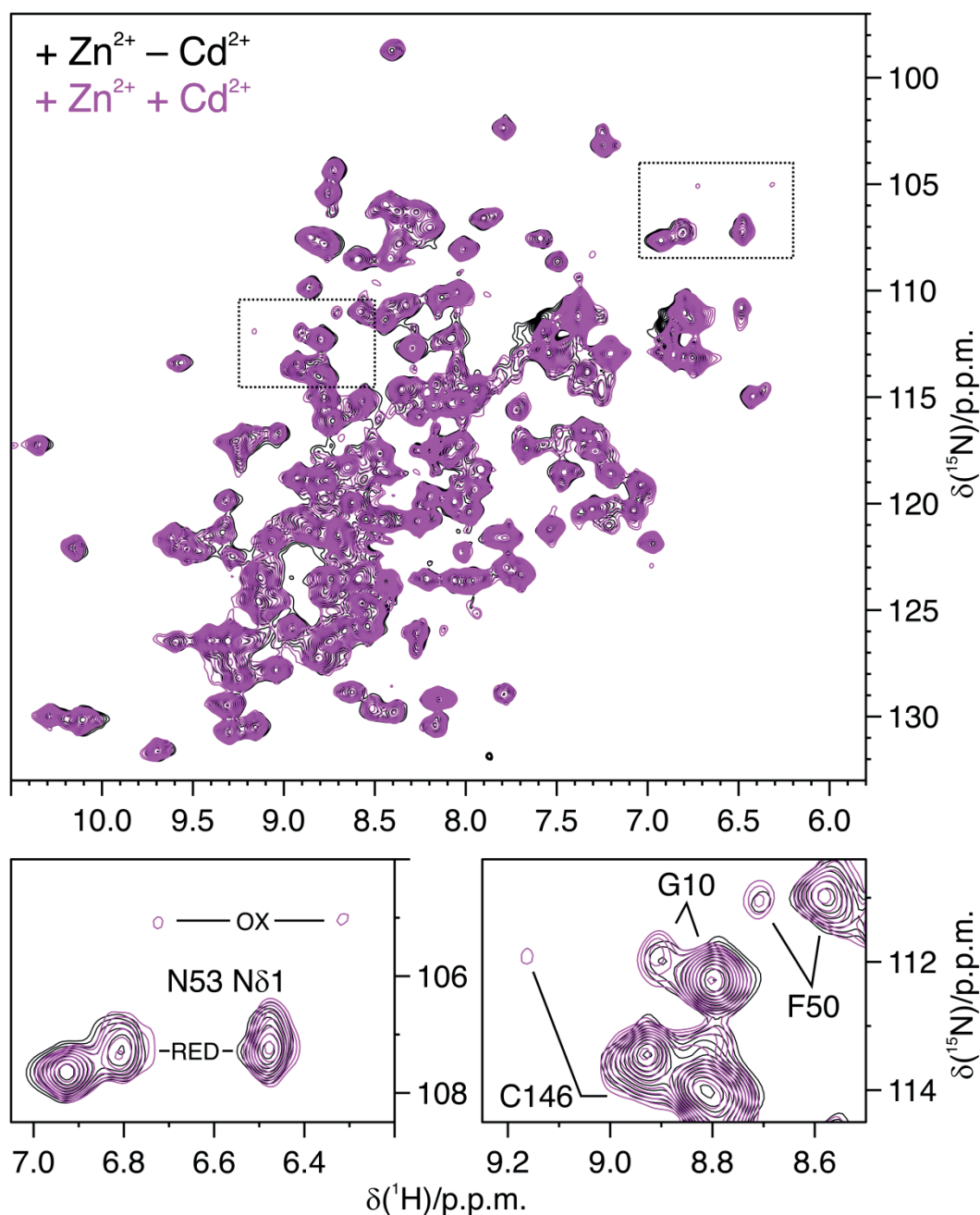


Fig. 3. Excess of Zn²⁺ prevents Cd²⁺-induced SOD1 oxidation. Overlay of ¹H-¹⁵N NMR spectra acquired on human cells expressing [U-¹⁵N] labelled SOD1 in excess of Zn²⁺ either untreated (black) or treated (magenta) with Cd²⁺ in the external medium. The bottom panels show enlarged areas of the whole spectra (dotted rectangles). Representative signals affected by the formation of the C57-C146 disulfide bond are labelled.

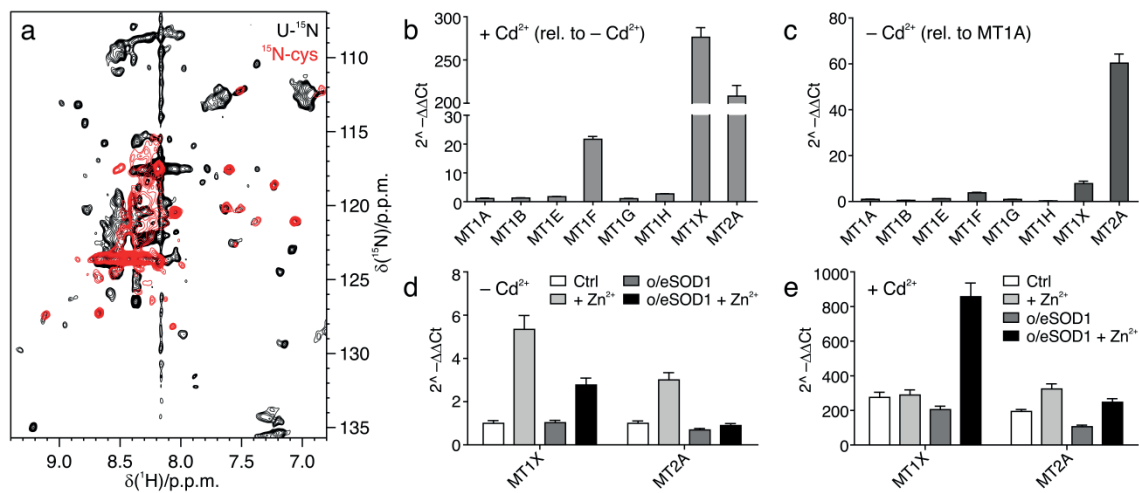


Fig. 4. Cd²⁺ treatment induces MT overexpression to NMR-detectable levels. (a) Overlay of ¹H-¹⁵N NMR spectra acquired on untransfected cells treated with Cd²⁺ either [U-¹⁵N] labelled (black) or [¹⁵N-cysteine] labelled (red); (b-e) Real-Time PCR analysis: (b) expression of different MT isoforms in Cd²⁺-treated untransfected cells, relative to basal (i.e. untransfected cells not treated with Cd²⁺); (c) basal expression of different MT isoforms relative to that of MT1A; (d) expression of MT1X and MT2A in cells not treated with Cd²⁺, overexpressing SOD1 in defect/excess of Zn²⁺, relative to basal; (e) expression of MT1X and MT2A in cells treated with Cd²⁺, overexpressing SOD1 in defect/excess of Zn²⁺, relative to basal. Ctrl: untransfected cells; +Zn²⁺: untransfected cells treated with excess Zn²⁺; o/eSOD1: cells overexpressing SOD1; o/eSOD1 +Zn²⁺: cells overexpressing SOD1 treated with excess Zn²⁺.

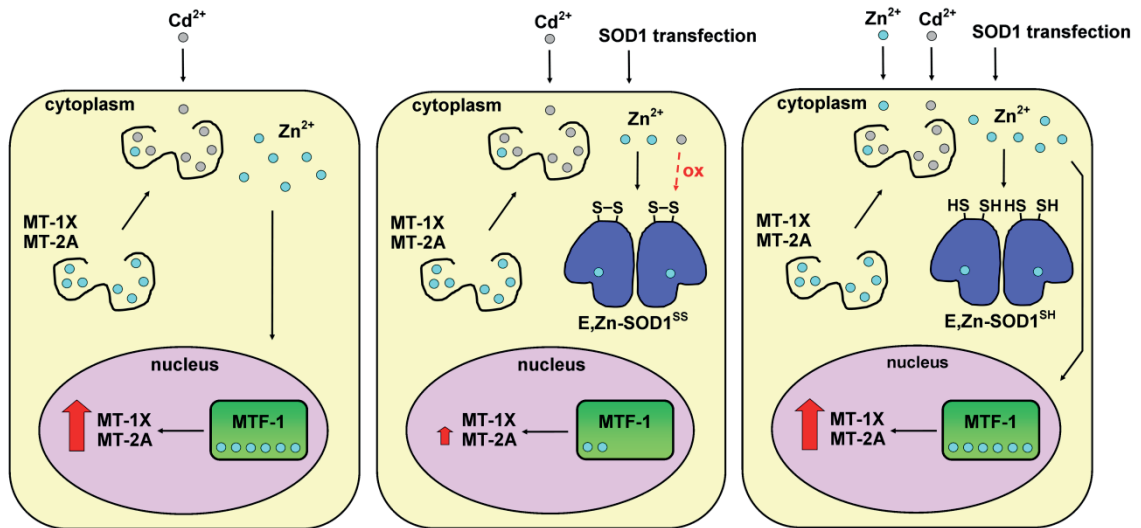


Fig. 5. Cd²⁺-induced SOD1 oxidation is modulated by Zn²⁺ and MT levels. Schematic drawing of the proposed mechanism of SOD1 oxidation as a function of Cd²⁺, Zn²⁺ and MTs. Left panel: when SOD1 is not overexpressed, Zn²⁺ (cyan) is displaced by Cd²⁺ (gray) and activates MTF-1 (green), which strongly induces MTs expression; the high levels of MTs contribute to restore the cellular redox balance by sequestering Cd²⁺. Center panel: when SOD1 is overexpressed, it sequesters the Zn²⁺ displaced by Cd²⁺ causing a decreased MTs induction; Cd²⁺ is not efficiently sequestered by MTs and causes redox imbalance, leading to SOD1 oxidation. Right panel: when excess Zn²⁺ is supplemented, overexpressed SOD1 is metallated and the strong induction of MTs is restored, thus preventing SOD1 oxidation.

Supporting Information

Polykretis et al.

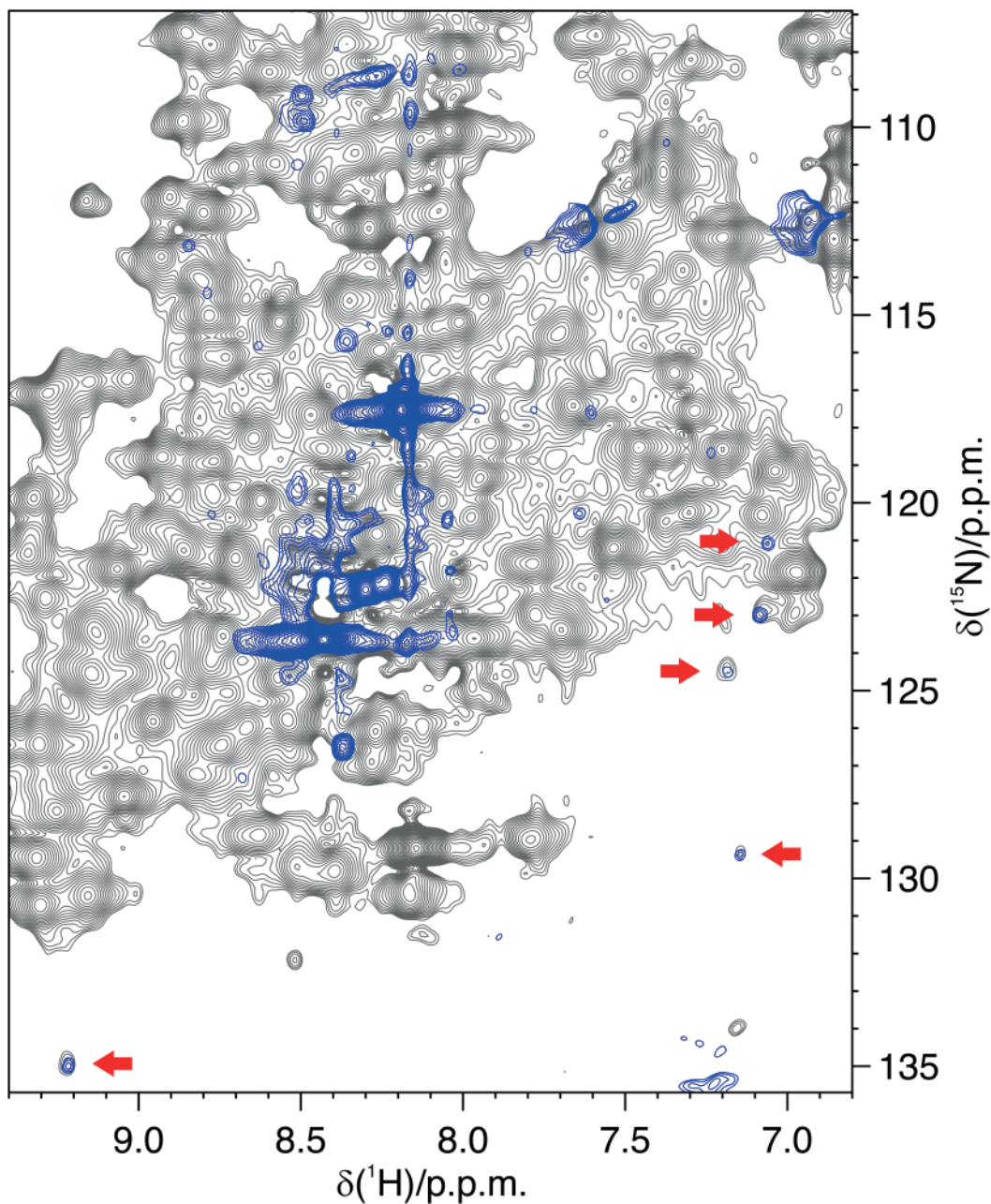


Fig. S1. Cd^{2+} -induced MTs are detected by NMR in cells overexpressing SOD1 in excess of Zn^{2+} . Overlay of ^1H - ^{15}N NMR spectra acquired on human cells expressing $[\text{U}-^{15}\text{N}]$ labelled SOD1 in excess of Zn^{2+} and treated with Cd^{2+} (grey, same as the magenta spectrum in Fig. 3) and untransfected $[\text{U}-^{15}\text{N}]$ labelled cells (blue, same as the black spectrum in Fig. 4a). Signals arising from MTs that are not overlapped with SOD1 signals are indicated (red arrows).

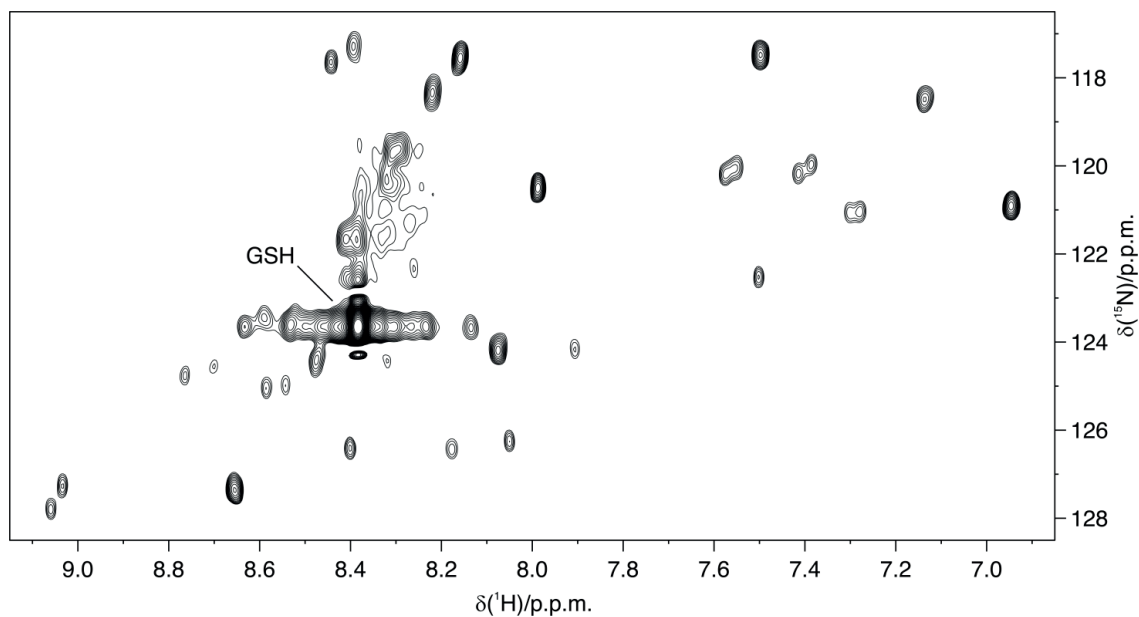


Fig. S2. Many cysteine signals are detected following treatment with Cd^{2+} . ^1H - ^{15}N NMR spectrum acquired for xx hours at 298 K on the lysate obtained from untransfected, [^{15}N -cysteine] labelled cells treated with Cd^{2+} (the corresponding in-cell NMR spectrum is shown in Fig. 4a, red). The strongest signals arises from [^{15}N -cysteine]-glutathione (GSH).

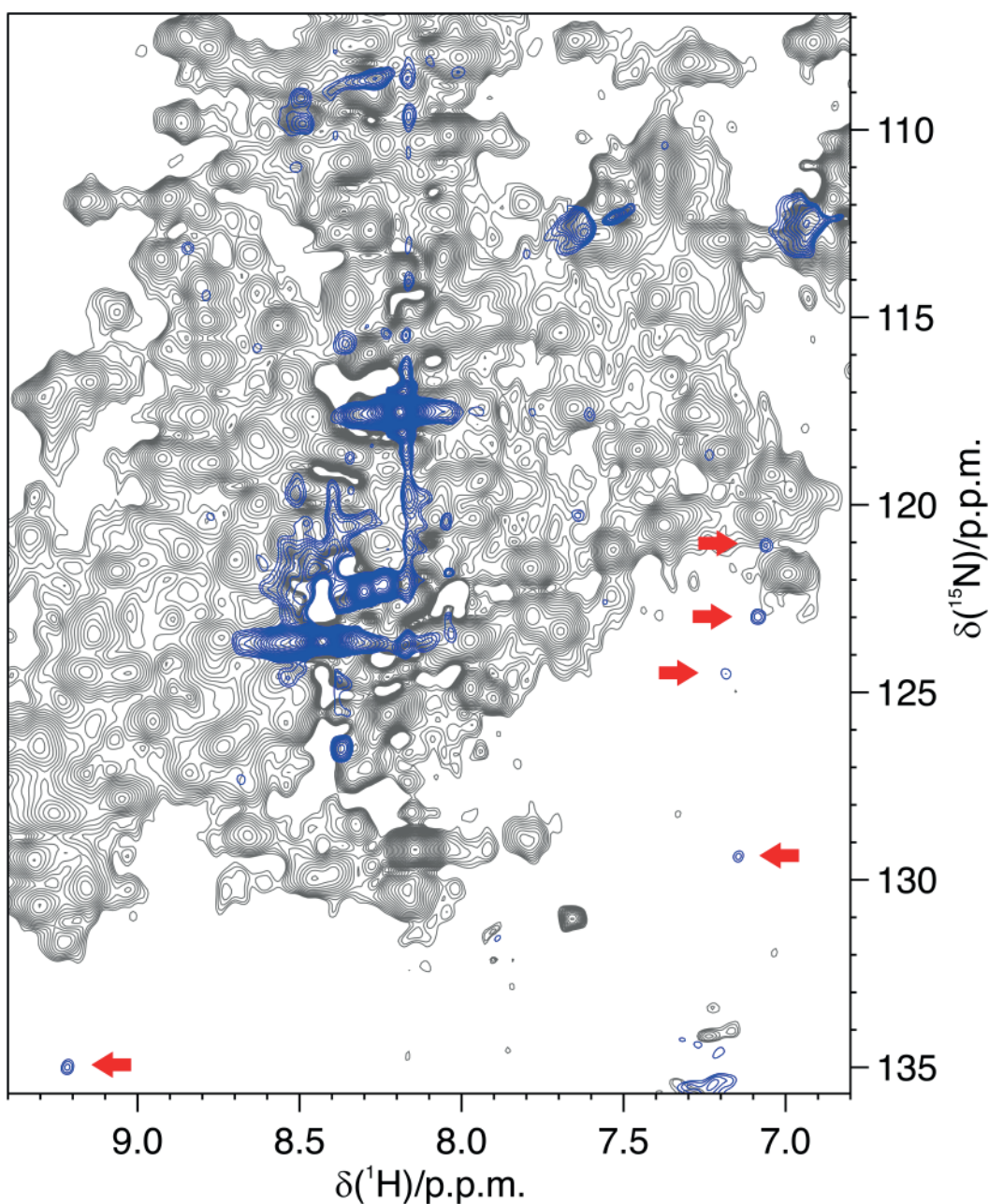


Fig. S3. MTs are not detected by NMR in Cd^{2+} -treated cells overexpressing SOD1 in defect of Zn^{2+} . Overlay of ^1H - ^{15}N NMR spectra acquired on human cells expressing [U - ^{15}N] labelled SOD1 in defect of zinc and treated with Cd^{2+} (grey, same as the red spectrum in Fig. 1) and untransfected [U - ^{15}N] labelled cells (blue, same as the black spectrum in Fig. 4a). MT signals that would not overlap with SOD1 signals are indicated (red arrows).

Table S1: TaqMan Gene Expression Assays employed for expression analysis of MTs.

Gene	UniProtKB	Assay ID
MT1A	P04731	Hs00831826_s1
MT1B	P07438	Hs01875377_s1
MT1E	P04732	Hs01938284_g1
MT1F	P04733	Hs00744661_sH
MT1G	P13640	Hs04401199_s1
MT1H	P80294	Hs00823168_g1
MT1M	Q8N339	Hs00828387_g1
MT1X	P80297	Hs00745167_sH
MT2A	P02795	Hs02379660_gH

Table S2: MTs expression in Cd²⁺-treated cells relative to basal levels and basal levels of each MT relative to MT1A. Values in 2^(-ΔΔCt) ± s.d. (n = 3)

Gene	+ Cd ²⁺ rel. to - Cd ²⁺	- Cd ²⁺ rel. to MT1A
MT1A	1.1 ± 0.2	1
MT1B	1.26 ± 0.09	0.53 ± 0.04
MT1E	1.7 ± 0.1	1.25 ± 0.08
MT1F	21 ± 1	3.8 ± 0.2
MT1G	1.0 ± 0.1	0.96 ± 0.06
MT1H	2.70 ± 0.09	0.31 ± 0.04
MT1M	<u>n.d.</u>	<u>n.d.</u>
MT1X	276 ± 11	8 ± 1
MT2A	208 ± 12	60 ± 4

Table S3: Expression of MT1X and MT2A in different conditions relative to basal. Values in 2^(-ΔΔCt) ± s.d. (n = 3).

Gene	- Cd ²⁺				+ Cd ²⁺			
	- o/eSOD1		+ o/eSOD1		- o/eSOD1		+ o/eSOD1	
	- Zn ²⁺	+ Zn ²⁺	- Zn ²⁺	+ Zn ²⁺	- Zn ²⁺	+ Zn ²⁺	- Zn ²⁺	+ Zn ²⁺
MT1X	1	5.3 ± 0.6	1.0 ± 0.1	2.8 ± 0.3	275 ± 30	289 ± 29	205 ± 19	857 ± 79
MT2A	1	3.0 ± 0.3	0.69 ± 0.07	0.90 ± 0.09	194 ± 11	324 ± 30	106 ± 9	247 ± 21

3. CONCLUSIONS

COCLUSIONS

During my doctoral studies I have been involved in several research projects, which had the common objective of understanding cellular processes at the molecular level in physiologically relevant settings. Among these, in-cell NMR constitutes the common line that connects most of my doctoral research activity, along with the study of the interaction of proteins with metal ions.

Regarding the development of a method that allows the inducible expression of target genes in stably transfected mammalian cell lines, the PB transposon methodology revealed to be a promising approach. In fact, we were able to obtain mammalian cell lines which integrated, likely in multiple copies, the expression cassette containing the inducible target genes. Furthermore, such mammalian cell lines positively reacted to the induction, starting the expression of the gene encoding the protein of interest. While the expression levels were still not sufficient to obtain suitable samples for in-cell NMR experiments, there are several parameters which can still be optimized in order to further improve the transposition and/or the induction efficiency, and consequently increase the intracellular protein concentration.

By in-cell NMR, we were able to determine the redox state of XIAP-BIR1 in the cytoplasm of mammalian cells. Furthermore, by performing additional *in vitro* experiments we showed that, in contrast with previous studies, copper does not substitute zinc in the zinc-finger motif, and does not have a specific binding site on XIAP-BIR1. Concerning XIAP-BIR3, we could not obtain significant structural information by in-cell NMR due to the fact that in the cytoplasm the domain interacts with a cellular component or with a partner which increases its tumbling rate. However, the data obtained from the *in vitro* experiments demonstrated that XIAP-BIR3 does not interact with copper and/or with CCS, contrarily to previous studies. Such results prompted us to elucidate the structural conformation of the full length XIAP, in order to better understand whether the spatial arrangement of its domains could affect its different functions, including the putative interaction with CCS. In fact, even if XIAP has been intensively studied during the last twenty years, the structure of

the full length protein is still unknown. We were able to purify the full length XIAP and we employed structural and biophysical techniques through an integrated approach, which allowed us to characterize the overall structural and dynamic properties of the protein for the first time. Our data indicate that full length XIAP assumes a compact homodimeric structure in solution, which could be amenable to be further refined by cryo-EM analysis in the near future. Finally, in-cell NMR allowed us to demonstrate how cadmium exposure affects SOD1 in human cells, an ubiquitous anti-oxidant protein. In this work we demonstrated that, unlike what previously assumed, cadmium does not replace zinc bound to intracellular SOD1. Instead, it causes the premature oxidation of the cysteines involved in SOD1 intramolecular disulfide bond. Such oxidation at an early stage of maturation would then interfere with CCS-mediated copper delivery, thus explaining the reported decrease in superoxide dismutase activity in cadmium-exposed tissues. In addition, the mechanism that we proposed in this study establishes a new relation between cadmium toxicity, zinc homeostasis and reduced SOD1 activity, which does not involve direct cadmium binding to SOD1 and that might help to better understand the toxicity mechanism of this heavy metal at molecular level. It is also noteworthy that in this study we could detect for the first time the signals of a protein encoded by genomic DNA, without recurring to transfection or exogenous protein delivery. In conclusion, in-cell NMR proved again to be a powerful approach uniquely suited to observe and to characterise different structural and chemical states of a protein directly in living cells. Thus, it is of critical importance to develop advanced approaches that will allow the application of in-cell NMR to investigate at the structural level relevant biological processes, under increasingly physiological conditions.

4. REFERENCES

REFERENCES

- Aricescu, A.R., Lu, W., and Jones, E.Y. (2006). A time- and cost-efficient system for high-level protein production in mammalian cells. *Acta Crystallogr. D Biol. Crystallogr.* *62*, 1243–1250.
- ATSDR (2017). ATSDR - Toxicological Profile: Cadmium.
- Baggio, C., Gambini, L., Udompholkul, P., Salem, A.F., Aronson, A., Dona, A., Troadec, E., Pichiorri, F., and Pellecchia, M. (2018). Design of Potent pan-IAP and Lys-Covalent XIAP Selective Inhibitors Using a Thermodynamics Driven Approach. *J. Med. Chem.*
- Banci, L., Bertini, I., Durazo, A., Girotto, S., Gralla, E.B., Martinelli, M., Valentine, J.S., Vieru, M., and Whitelegge, J.P. (2007). Metal-free superoxide dismutase forms soluble oligomers under physiological conditions: a possible general mechanism for familial ALS. *Proc. Natl. Acad. Sci. U.S.A.* *104*, 11263–11267.
- Banci, L., Bertini, I., Cantini, F., Kozyreva, T., Massagni, C., Palumaa, P., Rubino, J.T., and Zovo, K. (2012). Human superoxide dismutase 1 (hSOD1) maturation through interaction with human copper chaperone for SOD1 (hCCS). *Proceedings of the National Academy of Sciences* *109*, 13555–13560.
- Banci, L., Barbieri, L., Bertini, I., Luchinat, E., Secci, E., Zhao, Y., and Aricescu, A.R. (2013). Atomic-resolution monitoring of protein maturation in live human cells by NMR. *Nat. Chem. Biol.* *9*, 297–299.
- Barbieri, L., Luchinat, E., and Banci, L. (2015). Protein interaction patterns in different cellular environments are revealed by in-cell NMR. *Sci Rep* *5*, 14456.
- Barbieri, L., Luchinat, E., and Banci, L. (2018). Intracellular metal binding and redox behavior of human DJ-1. *J. Biol. Inorg. Chem.* *23*, 61–69.
- Bertin, G., and Averbeck, D. (2006). Cadmium: cellular effects, modifications of biomolecules, modulation of DNA repair and genotoxic consequences (a review). *Biochimie* *88*, 1549–1559.
- Bertrand, K., Reverdatto, S., Burz, D.S., Zitomer, R., and Shekhtman, A. (2012). Structure of Proteins in Eukaryotic Compartments. *J. Am. Chem. Soc.* *134*, 12798–12806.
- Bonomi, F., Ganadu, M.L., Lubinu, G., and Pagani, S. (1994). Reversible and non-denaturing replacement of iron by cadmium in *Clostridium pasteurianum* ferredoxin. *European Journal of Biochemistry* *222*, 639–644.
- Brady, G.F., Galbán, S., Liu, X., Basrur, V., Gitlin, J.D., Elenitoba-Johnson, K.S.J., Wilson, T.E., and Duckett, C.S. (2010). Regulation of the copper chaperone CCS by XIAP-mediated ubiquitination. *Mol. Cell. Biol.* *30*, 1923–1936.
- Burstein, E., Ganesh, L., Dick, R.D., van De Sluis, B., Wilkinson, J.C., Klomp, L.W.J., Wijmenga, C., Brewer, G.J., Nabel, G.J., and Duckett, C.S. (2004). A novel role for XIAP in copper homeostasis through regulation of MURR1. *EMBO J.* *23*, 244–254.
- Cai, L., Klein, J.B., and Kang, Y.J. (2000). Metallothionein inhibits peroxynitrite-induced DNA and lipoprotein damage. *J. Biol. Chem.* *275*, 38957–38960.

- Capper, M.J., Wright, G.S.A., Barbieri, L., Luchinat, E., Mercatelli, E., McAlary, L., Yerbury, J.J., O'Neill, P.M., Antonyuk, S.V., Banci, L., et al. (2018). The cysteine-reactive small molecule ebselen facilitates effective SOD1 maturation. *Nat Commun* 9, 1693.
- Chai, J., Shiozaki, E., Srinivasula, S.M., Wu, Q., Datta, P., Alnemri, E.S., Shi, Y., and Datta, P. (2001). Structural basis of caspase-7 inhibition by XIAP. *Cell* 104, 769–780.
- Chiaverini, N., and De Ley, M. (2010). Protective effect of metallothionein on oxidative stress-induced DNA damage. *Free Radic. Res.* 44, 605–613.
- Coyle, P., Philcox, J.C., Carey, L.C., and Rofe, A.M. (2002). Metallothionein: the multipurpose protein. *Cell. Mol. Life Sci.* 59, 627–647.
- Cuypers, A., Plusquin, M., Remans, T., Jozefczak, M., Keunen, E., Gielen, H., Opdenakker, K., Nair, A.R., Munters, E., Artois, T.J., et al. (2010). Cadmium stress: an oxidative challenge. *Biometals* 23, 927–940.
- Deveraux, Q.L., Takahashi, R., Salvesen, G.S., and Reed, J.C. (1997). X-linked IAP is a direct inhibitor of cell-death proteases. *Nature* 388, 300–304.
- Dzatko, S., Krafcikova, M., Hänsel-Hertsch, R., Fessler, T., Fiala, R., Loja, T., Krafcik, D., Mergny, J.-L., Foldynova-Trantirkova, S., and Trantirek, L. (2018). Evaluation of the Stability of DNA i-Motifs in the Nuclei of Living Mammalian Cells. *Angew. Chem. Int. Ed. Engl.* 57, 2165–2169.
- Fukuchi, K., Hearn, M.G., Deeb, S.S., Smith, A.C., Dang, N., Miyazaki, J., Bothwell, M., and Martin, G.M. (1994). Activity assays of nine heterogeneous promoters in neural and other cultured cells. *In Vitro Cell. Dev. Biol. Anim.* 30A, 300–305.
- Fulda, S., and Vucic, D. (2012). Targeting IAP proteins for therapeutic intervention in cancer. *Nat Rev Drug Discov* 11, 109–124.
- Galbán, S., and Duckett, C.S. (2010). XIAP as a ubiquitin ligase in cellular signaling. *Cell Death Differ.* 17, 54–60.
- Galvan, D.L., Nakazawa, Y., Kaja, A., Kettlun, C., Cooper, L.J.N., Rooney, C.M., and Wilson, M.H. (2009). Genome-wide mapping of PiggyBac transposon integrations in primary human T cells. *J. Immunother.* 32, 837–844.
- Getzoff, E.D., Cabelli, D.E., Fisher, C.L., Parge, H.E., Viezzoli, M.S., Banci, L., and Hallewell, R.A. (1992). Faster superoxide dismutase mutants designed by enhancing electrostatic guidance. *Nature* 358, 347–351.
- Gobe, G., and Crane, D. (2010). Mitochondria, reactive oxygen species and cadmium toxicity in the kidney. *Toxicology Letters* 198, 49–55.
- Hamatsu, J., O'Donovan, D., Tanaka, T., Shirai, T., Hourai, Y., Mikawa, T., Ikeya, T., Mishima, M., Boucher, W., Smith, B.O., et al. (2013). High-resolution heteronuclear multidimensional NMR of proteins in living insect cells using a baculovirus protein expression system. *J. Am. Chem. Soc.* 135, 1688–1691.

Hui, S.-K., Tse, M.-K., Yang, Y., Wong, B.C.-Y., and Sze, K.-H. (2010). Backbone and side-chain ¹H, ¹³C and ¹⁵N assignments of the ubiquitin-associated domain of human X-linked inhibitor of apoptosis protein. *Biomol NMR Assign* 4, 13–15.

IARC (2009). IARC Monographs on the Evaluation of Carcinogenic Risks to Humans – IARC.

Inomata, K., Ohno, A., Tochio, H., Isogai, S., Tenno, T., Nakase, I., Takeuchi, T., Futaki, S., Ito, Y., Hiroaki, H., et al. (2009). High-resolution multi-dimensional NMR spectroscopy of proteins in human cells. *Nature* 458, 106–109.

Jurczuk, M., Brzóska, M., Moniuszko-Jakoniuk, J., Gałazyn-Sidorczuk, M., and Kulikowska-Karpińska, E. (2004). Antioxidant enzymes activity and lipid peroxidation in liver and kidney of rats exposed to cadmium and ethanol. *Food and Chemical Toxicology* 42, 429–438.

Kimura, T., and Kambe, T. (2016). The Functions of Metallothionein and ZIP and ZnT Transporters: An Overview and Perspective. *International Journal of Molecular Sciences* 17, 336.

Kofod, P., Bauer, R., Danielsen, E., Larsen, E., and Bjerrum, M.J. (1991). ¹¹³Cd-NMR investigation of a cadmium-substituted copper, zinc-containing superoxide dismutase from yeast. *European Journal of Biochemistry* 198, 607–611.

Li, C., Zhao, J., Cheng, K., Ge, Y., Wu, Q., Ye, Y., Xu, G., Zhang, Z., Zheng, W., Zhang, X., et al. (2017). Magnetic Resonance Spectroscopy as a Tool for Assessing Macromolecular Structure and Function in Living Cells. *Annu Rev Anal Chem (Palo Alto Calif)* 10, 157–182.

Liang, Y., Ewing, P.M., Laursen, W.J., Tripp, V.T., Singh, S., and Splan, K.E. (2014). Copper-binding properties of the BIR2 and BIR3 domains of the X-linked inhibitor of apoptosis protein. *J. Inorg. Biochem.* 140, 104–110.

Lindberg, M.J., Tibell, L., and Oliveberg, M. (2002). Common denominator of Cu/Zn superoxide dismutase mutants associated with amyotrophic lateral sclerosis: decreased stability of the apo state. *Proc. Natl. Acad. Sci. U.S.A.* 99, 16607–16612.

Liston, P., Roy, N., Tamai, K., Lefebvre, C., Baird, S., Cherton-Horvat, G., Farahani, R., McLean, M., Ikeda, J.E., MacKenzie, A., et al. (1996). Suppression of apoptosis in mammalian cells by NAIP and a related family of IAP genes. *Nature* 379, 349–353.

Lopes, R.B., Gangeswaran, R., McNeish, I.A., Wang, Y., and Lemoine, N.R. (2007). Expression of the IAP protein family is dysregulated in pancreatic cancer cells and is important for resistance to chemotherapy. *Int. J. Cancer* 120, 2344–2352.

Lu, M., Lin, S.-C., Huang, Y., Kang, Y.J., Rich, R., Lo, Y.-C., Myszka, D., Han, J., and Wu, H. (2007). XIAP induces NF- κ B activation via the BIR1/TAB1 interaction and BIR1 dimerization. *Mol. Cell* 26, 689–702.

Luchinat, E., and Banci, L. (2018). In-Cell NMR in Human Cells: Direct Protein Expression Allows Structural Studies of Protein Folding and Maturation. *Acc. Chem. Res.* 51, 1550–1557.

- Luchinat, E., Barbieri, L., and Banci, L. (2017). A molecular chaperone activity of CCS restores the maturation of SOD1 fALS mutants. *Sci Rep* 7, 17433.
- Lukacs, C., Belunis, C., Crowther, R., Danho, W., Gao, L., Goggin, B., Janson, C.A., Li, S., Remiszewski, S., Schutt, A., et al. (2013). The structure of XIAP BIR2: understanding the selectivity of the BIR domains. *Acta Crystallogr. D Biol. Crystallogr.* 69, 1717–1725.
- Malgieri, G., Zaccaro, L., Leone, M., Bucci, E., Esposito, S., Baglivo, I., Del Gatto, A., Russo, L., Scandurra, R., Pedone, P.V., et al. (2011). Zinc to cadmium replacement in the *A. thaliana* SUPERMAN Cys2His2 zinc finger induces structural rearrangements of typical DNA base determinant positions. *Biopolymers* n/a-n/a.
- Malgieri, G., Palmieri, M., Esposito, S., Maione, V., Russo, L., Baglivo, I., de Paola, I., Milardi, D., Diana, D., Zaccaro, L., et al. (2014). Zinc to cadmium replacement in the prokaryotic zinc-finger domain. *Metallomics* 6, 96–104.
- Mannhold, R., Fulda, S., and Carosati, E. (2010). IAP antagonists: promising candidates for cancer therapy. *Drug Discov. Today* 15, 210–219.
- McCord, J.M., and Fridovich, I. (1969). Superoxide dismutase. An enzymic function for erythrocyte hemoglobin (hemocyanin). *J. Biol. Chem.* 244, 6049–6055.
- Mercatelli, E., Barbieri, L., Luchinat, E., and Banci, L. (2016). Direct structural evidence of protein redox regulation obtained by in-cell NMR. *Biochim. Biophys. Acta* 1863, 198–204.
- Mizutani, Y., Nakanishi, H., Li, Y.N., Matsubara, H., Yamamoto, K., Sato, N., Shiraishi, T., Nakamura, T., Mikami, K., Okihara, K., et al. (2007). Overexpression of XIAP expression in renal cell carcinoma predicts a worse prognosis. *International Journal of Oncology* 30, 919–925.
- Moulis, J.-M. (2010). Cellular mechanisms of cadmium toxicity related to the homeostasis of essential metals. *BioMetals* 23, 877–896.
- Mufti, A.R., Burstein, E., Csomos, R.A., Graf, P.C.F., Wilkinson, J.C., Dick, R.D., Challa, M., Son, J.-K., Bratton, S.B., Su, G.L., et al. (2006). XIAP Is a Copper Binding Protein Deregulated in Wilson's Disease and Other Copper Toxicosis Disorders. *Molecular Cell* 21, 775–785.
- Mufti, A.R., Burstein, E., and Duckett, C.S. (2007). XIAP: cell death regulation meets copper homeostasis. *Arch. Biochem. Biophys.* 463, 168–174.
- Nair, A.R., DeGheselle, O., Smeets, K., Van Kerkhove, E., and Cuypers, A. (2013). Cadmium-Induced Pathologies: Where Is the Oxidative Balance Lost (or Not)? *International Journal of Molecular Sciences* 14, 6116–6143.
- Nakagawa, Y., Abe, S., Kurata, M., Hasegawa, M., Yamamoto, K., Inoue, M., Takemura, T., Suzuki, K., and Kitagawa, M. (2006). IAP family protein expression correlates with poor outcome of multiple myeloma patients in association with chemotherapy-induced overexpression of multidrug resistance genes. *Am. J. Hematol.* 81, 824–831.

- Nakatani, Y., Kleffmann, T., Linke, K., Condon, S.M., Hinds, M.G., and Day, C.L. (2013). Regulation of ubiquitin transfer by XIAP, a dimeric RING E3 ligase. *Biochem. J.* *450*, 629–638.
- Niwa, H., Yamamura, K., and Miyazaki, J. (1991). Efficient selection for high-expression transfectants with a novel eukaryotic vector. *Gene* *108*, 193–199.
- Ogino, S., Kubo, S., Umemoto, R., Huang, S., Nishida, N., and Shimada, I. (2009). Observation of NMR signals from proteins introduced into living mammalian cells by reversible membrane permeabilization using a pore-forming toxin, streptolysin O. *J. Am. Chem. Soc.* *131*, 10834–10835.
- Pasinelli, P., Belford, M.E., Lennon, N., Bacsikai, B.J., Hyman, B.T., Trotti, D., and Brown, R.H. (2004). Amyotrophic Lateral Sclerosis-Associated SOD1 Mutant Proteins Bind and Aggregate with Bcl-2 in Spinal Cord Mitochondria. *Neuron* *43*, 19–30.
- Riedl, S.J., Renatus, M., Schwarzenbacher, R., Zhou, Q., Sun, C., Fesik, S.W., Liddington, R.C., and Salvesen, G.S. (2001). Structural basis for the inhibition of caspase-3 by XIAP. *Cell* *104*, 791–800.
- Rosen, D.R., Siddique, T., Patterson, D., Figlewicz, D.A., Sapp, P., Hentati, A., Donaldson, D., Goto, J., O'Regan, J.P., Deng, H.-X., et al. (1993). Mutations in Cu/Zn superoxide dismutase gene are associated with familial amyotrophic lateral sclerosis. *Nature* *362*, 59–62.
- Sarwar, N., Saifullah, Malhi, S.S., Zia, M.H., Naeem, A., Bibi, S., and Farid, G. (2010). Role of mineral nutrition in minimizing cadmium accumulation by plants. *J. Sci. Food Agric.* *90*, 925–937.
- Satarug, S., and Moore, M.R. (2004). Adverse Health Effects of Chronic Exposure to Low-Level Cadmium in Foodstuffs and Cigarette Smoke. *Environ Health Perspect* *112*, 1099–1103.
- Schimmer, A.D., Dalili, S., Batey, R.A., and Riedl, S.J. (2006). Targeting XIAP for the treatment of malignancy. *Cell Death Differ.* *13*, 179–188.
- Selenko, P., Serber, Z., Gadea, B., Ruderman, J., and Wagner, G. (2006). Quantitative NMR analysis of the protein G B1 domain in *Xenopus laevis* egg extracts and intact oocytes. *Proc. Natl. Acad. Sci. U.S.A.* *103*, 11904–11909.
- Serber, Z., Keatinge-Clay, A.T., Ledwidge, R., Kelly, A.E., Miller, S.M., and Dötsch, V. (2001). High-Resolution Macromolecular NMR Spectroscopy Inside Living Cells. *J. Am. Chem. Soc.* *123*, 2446–2447.
- Sladitschek, H.L., and Neveu, P.A. (2015). MXS-Chaining: A Highly Efficient Cloning Platform for Imaging and Flow Cytometry Approaches in Mammalian Systems. *PLoS ONE* *10*, e0124958.
- Smith, M.J., Marshall, C.B., Theillet, F.-X., Binolfi, A., Selenko, P., and Ikura, M. (2015). Real-time NMR monitoring of biological activities in complex physiological environments. *Curr. Opin. Struct. Biol.* *32*, 39–47.

- Srinivasula, S.M., Hegde, R., Saleh, A., Datta, P., Shiozaki, E., Chai, J., Lee, R.A., Robbins, P.D., Fernandes-Alnemri, T., Shi, Y., et al. (2001). A conserved XIAP-interaction motif in caspase-9 and Smac/DIABLO regulates caspase activity and apoptosis. *Nature* 410, 112–116.
- Sun, C., Cai, M., Gunasekera, A.H., Meadows, R.P., Wang, H., Chen, J., Zhang, H., Wu, W., Xu, N., Ng, S.-C., et al. (1999). NMR structure and mutagenesis of the inhibitor-of-apoptosis protein XIAP. *Nature* 401, 818–822.
- Sutherland, D.E.K., and Stillman, M.J. (2011). The “magic numbers” of metallothionein. *Metallomics* 3, 444–463.
- Suwazono, Y., Kido, T., Nakagawa, H., Nishijo, M., Honda, R., Kobayashi, E., Dochi, M., and Nogawa, K. (2009). Biological half-life of cadmium in the urine of inhabitants after cessation of cadmium exposure. *Biomarkers* 14, 77–81.
- Tainer, J.A., Getzoff, E.D., Beem, K.M., Richardson, J.S., and Richardson, D.C. (1982). Determination and analysis of the 2 A-structure of copper, zinc superoxide dismutase. *J. Mol. Biol.* 160, 181–217.
- Theillet, F.-X., Smet-Nocca, C., Liokatis, S., Thongwichian, R., Kosten, J., Yoon, M.-K., Kriwacki, R.W., Landrieu, I., Lippens, G., and Selenko, P. (2012). Cell signaling, post-translational protein modifications and NMR spectroscopy. *J. Biomol. NMR* 54, 217–236.
- Theillet, F.-X., Binolfi, A., Bekei, B., Martorana, A., Rose, H.M., Stuver, M., Verzini, S., Lorenz, D., van Rossum, M., Goldfarb, D., et al. (2016). Structural disorder of monomeric α -synuclein persists in mammalian cells. *Nature* 530, 45–50.
- Thévenod, F. (2009). Cadmium and cellular signaling cascades: To be or not to be? *Toxicology and Applied Pharmacology* 238, 221–239.
- UNEP (2008). Draft final review of scientific information on cadmium. United Nations Environment Programme, Chemicals Branch.
- Valentine, J.S., Doucette, P.A., and Zittin Potter, S. (2005). Copper-zinc superoxide dismutase and amyotrophic lateral sclerosis. *Annu. Rev. Biochem.* 74, 563–593.
- Vucic, D. (2018). XIAP at the crossroads of cell death and inflammation. *Oncotarget* 9, 27319–27320.
- Wang, W., Lin, C., Lu, D., Ning, Z., Cox, T., Melvin, D., Wang, X., Bradley, A., and Liu, P. (2008). Chromosomal transposition of PiggyBac in mouse embryonic stem cells. *Proc. Natl. Acad. Sci. U.S.A.* 105, 9290–9295.
- Wilson, M.H., Coates, C.J., and George, A.L. (2007). PiggyBac transposon-mediated gene transfer in human cells. *Mol. Ther.* 15, 139–145.
- Witt, A., and Vucic, D. (2017). Diverse ubiquitin linkages regulate RIP kinases-mediated inflammatory and cell death signaling. *Cell Death and Differentiation* 24, 1160–1171.

Wu, S.C.-Y., Meir, Y.-J.J., Coates, C.J., Handler, A.M., Pelczar, P., Moisyadi, S., and Kaminski, J.M. (2006). piggyBac is a flexible and highly active transposon as compared to sleeping beauty, Tol2, and Mos1 in mammalian cells. *Proc. Natl. Acad. Sci. U.S.A.* *103*, 15008–15013.

Yusa, K., Zhou, L., Li, M.A., Bradley, A., and Craig, N.L. (2011). A hyperactive piggyBac transposase for mammalian applications. *Proc. Natl. Acad. Sci. U.S.A.* *108*, 1531–1536.

5. ACKNOWLEDGMENTS

ACKNOWLEDGMENTS

I would like to warmly thank my tutor, Prof. *Lucia Banci*, for giving me the opportunity to pursue my doctoral studies in her laboratory, but mainly, because her dedication, her unending passion for scientific research and her continuous strive to make CERM grow are a constant driving force that encourages us to always give our best.

I would like to thank Dr. *Enrico Luchinat*, because he truly loves research, because I matured as researcher working at his side, and because conversing with him about science is always an interesting and stimulating experience.

I would like to thank Dr. *Letizia Barbieri*, because during these years she has been constantly at my side in the laboratory, giving me precious suggestions and instructions.

I would like to thank *Leonardo Gonnelli*, because he is an indispensable and skilful laboratory technician, who taught me a lot about protein purification.

Indeed, I would like to thank all “cermians”, because each and every one of them has contributed in making my doctoral studies the most formative and constructive experience of my life.

I would like to thank my great friend, Dr. *Gerasimos Anastasiadis*, for his authentic friendship and for his constant support.

I want to thank *Argo*, because he filled with light and joy every single moment spent with him, even during the darkest periods. Goodbye my friend!

And last, but absolutely not least, I want to thank my family because they never stopped believing in me and because especially as a biologist, I can firmly assert that I owe them everything I am.